UNIVERSITY OF MINNESOTA
ST. ANTHONY FALLS HYDRAULIC LABORATORY

Project Report No. 229

PHASE A-2, LARGE CAVITATION CHANNEL, DAVID TAYLOR NAVAL SHIP RESEARCH AND DEVELOPMENT CENTER

by

J. M. Wetzel, D. W. Bintz, R. E. A. Arndt, T. Morel,
S. Gavali, C. C. S. Song, and J. M. Killen

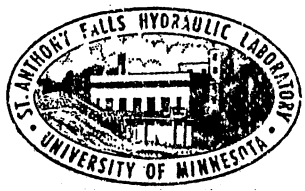

Prepared for

SSV&K/DMJM: Joint Venture
1709 New York Ave., N.W.
Washington, D.C. 20006

August 1983
Minneapolis, Minnesota

Permanent File Copy
St. Anthony Falls Hydraulic Laboratory

Final Report on Phase A-2, Task A-1:

Studies of the Turbulence Management System

by

R. E. A. Arndt, D. Bintz,
and T. Morel

St. Anthony Falls Hydraulic Laboratory
University of Minnesota
Minneapolis, Minnesota 55414

Prepared for

SSV&K/DMJM:Joint Venture
1709 New York Ave., N.W.
Washington, D.C. 20006

July 1983

II. MEAN FLOW AND TURBULENCE CONTROL BY HONEYCOMBS

A. Flow Quality

The LCC specifications call for a very high quality flow in the test section, with mean velocity non-uniformities less than one percent and turbulence intensity less than 0.1 percent. More specifically, to meet these specifications the following items must be controlled:

1) nonuniformity of the streamwise velocity component
2) flow angularity (non-zero cross-stream velocity component)
3) mean swirl (non-zero tangential component)
4) streamwise turbulence intensity
5) cross-stream turbulence intensities
6) total turbulence intensity $q = \sqrt{1/2(u^2+v^2+w^2)}$

The tools available for these purposes in a water flow are the use of honeycombs and a contraction, while turbulence-reducing screens popular in wind tunnels are not recommended because they are susceptible to hydroelastic interactions which lead, under some conditions, to large screen oscillations.

B. Contraction Effects

The contraction adopted for the LCC has a contraction ratio of six. The effect of flow passage through such a contraction may be estimated to produce:

1) a large reduction in streamwise velocity nonuniformity on the order of $1/c^2$, i.e., 1/36,
2) unknown effect on flow angularity,
3) amplification of mean swirl by vortex stretching,

TASK A-1: Studies of the Turbulence Management System

by

R. E. A. Arndt, D. Bintz, and T. Morel

St. Anthony Falls Hydraulic Laboratory, University of Minnesota

I. INTRODUCTION

The Large Cavitation Channel (LCC) has very tight performance specifications for the flow quality in the test section, both for uniformity of the mean velocity profiles and turbulence levels. The mean velocity profiles have been addressed experimentally in the Task A report, and mathematically in the Task B report. This task is concerned with the turbulence levels in the test section. Turbulence levels are partially controlled by honeycomb design. Model studies of honeycombs should be conducted at as high a Reynolds number as possible to reduce scale effects. Thus, the decision was made not to utilize the undistorted 1 to 10 scale model of the preliminary Kempf and Remmers (K&R) contraction, test section, and diffuser that was used in the Task A studies as the Reynolds number based on honeycomb parameters was judged to be too low to obtain meaningful results. The existing wind tunnnel facility was modified for the turbulence measurements in rather an unique manner so that full scale honeycombs could be evaluated. These modifications were made after the tests of the Task A program were completed. Results of the turbulence measurements and recommendations for a turbulence management system for the LCC are discussed in the following sections.

4) theoretical reduction of streamwise turbulence intensity by a factor of less than 0.1,

5) theoretical reduction of cross-stream intensities by a factor 0.35 (i.e., the existing flow is strongly anisotropic, and the turbulence will be dominated by the cross-stream component),

6) experimentally determined reduction of the total turbulence intensity by a factor of about 0.2.

C. Honeycomb Tasks

In evaluating the expected effects produced by a 6:1 contraction, it is observed that the target mean velocity nonuniformity will be achieved by the contraction alone, but that the honeycomb will have to be relied on to provide the necessary reductions in flow angularity, mean swirl and turbulence intensity.

The first two tasks are achieved by making the honeycomb deep compared to the size of its cells. Making it sufficiently deep to produce a fully developed pipe flow in its passages would, by definition, produce a perfectly axial outflow. For the Reynolds number range of interest this would imply an L/D of about 30, where L is the honeycomb depth and D is the cell size.

Reduction of the turbulence level is a more complex subject. One reason for the complexity is that the honeycomb not only reduces the preexisting (incoming) turbulence, but it also generates turbulence of its own. The flow exiting the honeycomb has excess kinetic energy, part of which produces new turbulence downstream of the honeycomb. The magnitude, scale and subsequent decay of this turbulence depend on Reynolds number based on the passage diameter D, on D itself, L/D and on t/D, where t is the wall thickness. In the range of interest, the dependence on Reynolds number and on L/D is weak, and the most

important parameters for the honeycomb generated turbulence are D and t/D. Using a thin-walled construction material with t/D = 0.25 and a 25 mm (1 inch) cell size, the turbulence produced will decay rapidly and reach levels well below 0.1 percent in the test section. A larger cell size with 50 mm openings produces slower-decaying turbulence which is projected to have intensity on the order of 0.1 percent at the test section entrance, leaving no safety margin and not allowing any contribution from the preexisting turbulence. Thus, based on the development of the honeycomb-generated turbulence, recommendation of a 25 mm cell size honeycomb is appropriate.

The attenuation of the preexisting turbulence is not the same for the different velocity components, nor is it uniform across the spectrum. All honeycombs reduce transverse fluctuations much more strongly than streamwise fluctuations, and deep honeycombs can actually suppress transverse fluctuations altogether. Downstream of the honeycomb the turbulence gradually redistributes the streamwise turbulence energy over all three components, and so in the following discussion we shall mainly consider the reduction in the total turbulence intensity.

As for the spectral dependence of attenuation in deep honeycombs, the largest scales with wavelengths much longer than the honeycomb depth are attenuated equally, while the attenuation of wavelengths shorter than the honeycomb depth grow with decreasing wavelength. The possible exception is eddies smaller than the honeycomb cell size that could conceivably pass through the cell, but those eddies would decay rapidly downstream due to their size and so they need not be of concern here. Thus, the main concern is the attenuation of the largest turbulent motions, which are also those that will take the longest to decay downstream of the honeycomb. The degree of their attenuation depends on the pressure drop across the honeycomb, and so for a meaningful

attenuation the honeycomb has to produce a pressure drop coefficient on the order of one or more.

D. Kempf and Remmers Design

The original design of Kempf and Remmers envisioned a honeycomb with square cells with 50 mm sides and 500 mm depth. The honeycomb was to have a wall thickness of 1 mm and was to be built in 1200 x 1200 mm sections set in a stainless steel frame with wall thickness of 10 mm.

An evaluation of this honeycomb indicated that it is probably insufficient to produce the desired flow quality. The honeycomb has too low a length-to-diameter ratio (L/D = 10) to eliminate flow angularity and swirl. The pressure drop across the honeycomb is very small, based on an estimated pressure coefficient of about 0.2 and, thus, would not be sufficiently effective in reduction of the preexisting turbulence. Further, the cell size is too large to permit the honeycomb generated turbulence to decay to acceptable levels before reaching the test section. Finally, supporting the honeycomb in a thick-walled grid as originally proposed would lead to large wakes and additional turbulence production behind the supporting structure, further aggravating the turbulence problem.

E. Alternate Design

In consequence of the weaknesses of the original design, two alternative designs for the LCC honeycomb are proposed. These designs are based on the considerations discussed in the above. Both designs have 25 mm (1 inch) square cells with a wall thickness of 0.6 mm (0.025 inches). One of the designs is a single honeycomb with L/D = 40, i.e., 1000 mm (40 inches) long, producing a pressure drop coefficient of 0.7 over the expected flow speed range of the LCC. The other design is as tandem configuration of two honeycombs with L/D = 20,

i.e., each 500 mm (20 inches) long. The pressure coefficient of each honeycomb is about 0.32; i.e., the total for the two is slightly less than for the single deeper honeycomb.

The first honeycomb is expected to be capable of producing a swirl-free axial flow with streamwise velocity nonuniformity reduced by a factor of 0.5. The total turbulence intensity is expected to be reduced by a factor of 0.35.

The second design should also produce a swirl-free axial flow downstream of the two honeycombs. The axial velocity nonuniformity should be reduced by a factor of 0.73 in each honeycomb, for a total reduction factor of 0.53, which would make it marginally less effective than the single deep honeycomb. The total turbulence intensity should be reduced by a factor of 0.45 by a single honeycomb. If the two honeycombs were spaced sufficiently far apart for the exiting turbulence to approach isotropy, the effect of the two honeycombs would be multiplicative, and the total reduction factor would be 0.21. This would be significantly better than for a single honeycomb of twice the depth; however, since the two honeycombs cannot really be spaced so far apart, a smaller reduction is to be expected. Nevertheless, it seems likely that the two honeycombs spaced about a meter apart should produce at least the same or better reduction than the single honeycomb.

In summary, two alternative designs are proposed: (1) a single honeycomb one meter deep, or (2) two tandem honeycombs 500 mm deep and spaced on the order of one meter apart. They both should produce similar pressure drops and reduction in mean velocity nonuniformity. The single honeycomb is expected to be more effective in eliminating mean flow skewness and swirl, but even the tandem honeycomb should be adequate. As for the turbulence intensity, the tandem honeycombs should produce a better attenuation of the largest scales of turbulence, meaning those which are larger than the honeycomb depth. For

smaller scales, however, the single deep honeycomb will offer an advantage because a larger part of the turbulence spectrum will effectively be small scale with respect to the honeycomb depth, and it will undergo a stronger attenuation.

An advantageous strategy seems to be the choice of two tandem honeycombs, and construction of the settling chamber in such a way that the two honeycombs could be spaced at various distances from each other varying from zero to two meters. In this fashion, it should be possible to fine tune the installation for the optimum end result.

The honeycombs will be subjected to a very significant load due to the pressure drop they produce, reaching 31,000 lbs at a test section velocity of 50 fps. The first of the two alternative designs has been analyzed by SSV&K, who found it capable of supporting the loads. The second design has also been analyzed for structural rigidity and strength, and appears to be adequate.

F. Overall Improvements in Flow Quality

Summarizing the overall improvements in mean flow quality due to the honeycomb plus contraction, it is found that these should be adequate even for a highly distorted flow coming out of the fourth elbow just upstream of the contraction. The intensity of the preexisting turbulence is expected to be reduced by a combined factor of 0.07 for the single honeycomb and slightly more for the tandem design. This means that the design objective of 0.1 percent total turbulence intensity in the test section will be achieved only if the largest scales of turbulence ahead of the honeycomb will have an intensity of less than two percent. (The intensity of the smaller scale turbulence is of lesser concern as it will be attenuated and will decay more than the large scales.)

III. THE PHYSICAL MODEL

A. Streamtube concept

To reduce scale effects, the Reynolds number in the model should be as close to the full scale Reynolds number as possible. It was obvious that the honeycomb Reynolds number would be much too low if the tests were conducted in the 1 to 10 scale model. Therefore, an alternative scheme was developed that would provide Reynolds numbers much closer to the full-scale values. This scheme is based on a streamtube concept. As the flow at the entrance and exit of the contraction is essentially uniform, it is possible to consider a streamtube of a convenient cross-sectional area. The streamtube has the same contraction ratio as the contraction itself, i.e., six, and a length equal to the full-scale contraction length. As a model of the streamtube is bounded by solid walls, the boundary layer growth along the walls must be considered in selection of cross-sectional area. Boundary layer computations indicated that an exit area of about the same value as that available in the 1 to 10 scale model test section may be adequate. This is very convenient, since it permits use of several components of the 1:10 model such as the fan, diffuser, and inlet section.

In conjunction with this streamtube, sections of full-scale honeycombs were used at the inlet. The decay length, i.e., the length of the contraction, was full scale. It was anticipated that if boundary layer growth influenced the centerline turbulence measurements near the streamtube exit, the location at which this would occur could be detected. Data at points upstream would then be extrapolated to the test section.

B. Model Layout

A schematic of the model layout is shown in Fig. 1. The framing convered with porous fabric enclosing the inlet as well as the inlet itself were part of the 1 to 10 scale model. The fabric had a sufficiently tight weave to prevent dust particles from being drawn into the test reach. The streamtube model consisted of a total length of about 44 ft, which includes a 4.67 ft. straight entrance length. In the longitudinal direction, the streamtube had a straight taper from the inlet plane to 8 ft upstream of the exit plane. As the K&R contraction shape had modest curvature and area change from this point on, the streamtube model was constructed with parallel walls over the last 8 ft. The model was built in sections from 3/8 inch plywood and wood support framing, and the outside corners were reinforced with sheet metal angles to prevent air leakage. Holes were drilled through the top surface along the centerline of the streamtube model through which probes for velocity measurement could be inserted. The row of holes extended over the entire length of the model and were spaced at 2 ft intervals. The exit plane of the streamtube model is attached to the diffuser of the 1 to 10 scale model, which in turn is connected to the suction opening of the fan.

The turbulence generating grid was constructed of three-quarter inch pine quarter-round bars placed horizontally just downstream of the bellmouth inlet. The flat sides of the quarter-round were oriented horizontally and vertically with the curved surface facing into the flow and upward. This position and shape was chosen to generate turbulence similar to the wakes trailing a vane in the proposed elbows by forcing the flow over long upper surfaces and short lower surfaces creating relatively smaller pressures at the top of each bar. Spacing was arbitrarily chosen at two inch center-to-center distances, and the resulting turbulence levels were considered satisfactory for this study.

Two honeycombs with a depth of 20 in. and 40 in. were fabricated. The cell dimensions were 2x2 in. and 1xl in., respectively. The larger cell size corresponds to the K&R honeycomb design. Wall thickness for both honeycombs was 0.025 inches. It was not possible to find a source of supply for these honeycomb units. The small unit size, about 29 in. sq., did not justify a special order, and in any case the delivery time would not fit into the tight time schedule. Therefore, the honeycombs were fabricated in the Laboratory shop, but not without difficulty. Various construction materials were considered, and the material finally chosen was cardboard. The honeycombs were fabricated in sections and the corners were fixed together. As the aerodynamic loading was quite small, the completed unit proved to be adequately rigid.

C. Instrumentation and Test Procedure

Hot wire anemometry was applied to the investigation of turbulence within the streamtube model. The TSI constant temperature anemometer Model 1050 with a TSI hot wire probe Model 1212-T1.5 acted as the sensing unit providing DC voltage (to determine mean velocity) to a Fluke 8050A digital multimeter, and AC voltage (to determine root mean square velocity) to a Bruel and Kjoer (B&K) Type 2607 measuring amplifier. The rms level of velocity fluctuations was measured with the B&K, and the amplified signal was then sent to a Nicolet Mini-Ubiquitous FFT Computing Spectrum Analyzer Model 44A where spectra were displayed and photographed.

Wire stability and trim were assured by frequently monitoring the response of the wire to a 1 KHz square wave with a Tektronix 2213 60 mHZ oscilloscope.

Turbulence was measured at twenty-one stations along the streamtube (one station just before the honeycomb and the remainder spaced two feet apart on the

contraction). A measurement was taken at each station. (Multiple readings were taken prior to the honeycomb due to the high turbulence levels.) Prior to each analysis, the probe was calibrated in the centerline of a free-jet emitted from the orifice of a large plenum chamber. Velocity of the jet was determined by the Bernoulli equation for energy conservation. If the confidence in a probe's performance was high and a preceding calibration curve was applicable for the possible velocity range expected in that area of the contraction, a check was made of the calibration curve. This curve, if satisfactory, would be used in the new analysis.

Placing the probe at the centerline of the contraction, measurements of the core flow were taken and spectras recorded. The probe was held in position by hand to reduce the transmission of floor vibrations to the probe.

Air density was determined prior to each experimental session by applying the barometric pressure (using a mercury barometer) and temperature to the table for the density of moist air in the Handbook of Chemistry and Physics [1].

IV. DISCUSSION OF RESULTS

A. Data Format

The results of the experimental program are presented in Figs. 2 through 7. Figures 2 and 3 present turbulence intensity normalized with respect to local velocity as a function of distance through the nozzle (i.e. u/U vs x). Figure 4 presents turbulent intensity normalized to the value at the contraction inlet as a function of distance through the nozzle. For comparison purposes, Fig. 5 presents the variation of turbulence intensity normalized to the velocity in the settling chamber as a function of distance from the honeycomb in terms of honeycomb cell size, M, (i.e. u/U_1 vs x/M). Finally, Figs. 6 and 7 are wave number spectra, wherein wave number has been modified by multiplying by the local contraction ratio, C; i.e.

$$ck = \frac{2\pi cf}{U} \tag{1}$$

where c and U are the contraction ratio and centerline velocity at the station in question. The rationale for this presentation of data is discussed below.

B. Expected Results

The final turbulence level in the test section is the result of a complex process. Assuming a certain turbulence level leaving the fourth elbow, attenuation of this level of turbulence is achieved within the honeycomb, the level of attenuation being related to the pressure drop through the honeycomb and the ratio of length to cell size. The honeycomb itself generates

turbulence. For the sake of simplicity we can assume that the turbulence is isotropic, having a scale comparable to the cell size M and having a turbulence level, u, of unknown magnitude. This turbulence decays via viscous dissipation until it reaches the nozzle, at which point the mean flow accelerates and the turbulent eddies are subjected to stretching along the x-axis by a factor c, whereas vortex filaments in the x and y direction are subjected to contraction by a factor, $\sqrt{c}$. Prandtl [2] first considered this process and calculated that the u component of turbulence decreases by a factor of K_c, whilst the v and w components increase by a factor $\sqrt{c}$. However, the process is more complex since as the turbulence becomes more anisotropic with distance, other factors come into play which tend to force the turbulence back to isotropy. Hence there is an energy transfer between components such that further downstream in the nozzle, u tends to increase, and the rate of increase of v and w is less than expected. Finally the turbulence level in the tunnel test section,

$$T \equiv \frac{q_T}{U_T} \tag{2}$$

$$q \equiv \sqrt{u^2 + v^2 + w^2} \tag{3}$$

is the combined result of the change in q through the contraction and the acceleration of the mean velocity from the entrance to the contraction to the tunnel test section. The turbulence level in the test section depends on the turbulence level leaving the fourth elbow, the properties of the honeycomb including pressure drop and cell size, the length of the stilling section, and the contraction of the nozzle, as well as other geometric properties of the

nozzle that are not clearly understood. However, there is a considerable body of knowledge available which can be utilized to further our understanding of this complex process.

As a start, we will assume that the turbulence level leaving the honeycomb can be modeled by grid generated turbulence. Simple calculations (c.f. Tennekes and Lumley [3]) indicate that

$$\frac{u\ell}{\nu} = \text{const.} \tag{4}$$

$$\frac{u}{U} = \frac{C^{1/2}\left[\frac{u\ell}{\nu}\right]^{1/2}}{\left[\frac{Ux}{\nu}\right]^{1/2}} \quad \text{or} \quad u \sim \frac{1}{x^{1/2}} \tag{5}$$

$$\frac{\ell}{x} = \frac{C^{1/2}\left[\frac{u\ell}{\nu}\right]^{1/2}}{\left[\frac{Ux}{\nu}\right]^{1/2}} \qquad \ell \sim x^{1/2} \tag{6}$$

wherein u is turbulence intensity and ℓ is the scale of that turbulence. The simple analysis says that we should expect the turbulence level to decay with distance whereas the scale of the turbulence should increase. This simple model is only valid in the initial period of decay. A simple fit to more complex theory as well as experiment is given by

$$\frac{u}{U} = \frac{C_1}{\left(\frac{x}{M}\right)^{0.65}} \tag{7}$$

wherein M is the cell size. Noting the analogy between Eqs. 5 and 6 the following model for turbulence scale is proposed:

$$\frac{\ell}{x} = \frac{C_1}{\left(\frac{x}{M}\right)^{0.65}} \tag{8}$$

or

$$\frac{\ell}{M} = C_1 \left(\frac{x}{M}\right)^{0.35} \tag{9}$$

The flow through the contraction is more complex since there is a combination of distortion, dissipation, and energy transfer between components taking place. Neglecting the latter two effects, an estimate of the effect of the contraction can be made using approximations to the results of Ribner and Tucker [4] and Batchelor [5]:

$$\left(\frac{u_2}{u_1}\right)^2 \cong [3/4c^2](\log 4\ c^3 - 1) \quad c \gg 1 \tag{10}$$

$$\left(\frac{v_2}{v_1}\right)^2 = \left(\frac{w_2}{w_1}\right)^2 \cong \frac{3c}{4} \tag{11}$$

Assuming isotropic flow at the inlet we obtain:

$$q_1^2 = u_1^2 + v_1^2 + w_1^2 = 3u_1^2 \tag{12}$$

since $u_1 = v_1 = w_1$.

For the outlet

$$q_2^2 = \left[\left(\frac{u_2}{u_1}\right)^2 + \left(\frac{v_2}{v_1}\right)^2 + \left(\frac{w_2}{w_1}\right)^2\right] u_1^2 \tag{13}$$

or

$$\frac{q_2^2}{q_1^2} = \frac{1}{3}\left[\left(\frac{u_2}{u_1}\right)^2 + \left(\frac{v_2}{v_1}\right)^2 + \left(\frac{w_2}{w_1}\right)^2\right] \tag{14}$$

The turbulence intensity at the outlet is then

$$\frac{q_2}{U_2} = \frac{1}{c\sqrt{3}}\left[\left(\frac{u_2}{u_1}\right)^2 + \left(\frac{v_2}{v_1}\right)^2 + \left(\frac{w_2}{w_1}\right)^2\right]^{1/2}\frac{q_1}{U_1} \tag{14a}$$

which reduces to

$$\frac{q_2}{U_2} = \frac{1}{c\sqrt{3}}\left[\frac{3}{4c^2}(\log 4c^3 - 1) + \frac{3}{2}c\right]^{1/2}\frac{q_1}{U_1} \tag{15}$$

For a contraction of six we obtain:

$$\frac{q_2}{U_2} \cong \frac{1}{(2C)^{1/2}}\frac{q_1}{U_1} \tag{16}$$

$$\frac{q_2}{U_2} = 0.289\,\frac{q_1}{U_1} \qquad \text{1:6 contraction} \tag{17}$$

Classical design equations assume that through the nozzle, the turbulence is unchanged, i.e. $q_1 = q_2$ and hence the relative level simply changes by the contraction ratio (compare Eqs. 16 and 18);

$$\frac{q_2}{U_2} = \frac{1}{c}\frac{q_1}{U_1} \tag{18}$$

or $$\frac{q_2}{U_2} = 0.167 \quad \frac{q_1}{U_1} \qquad \text{1:6 contraction} \qquad (19)$$

Because of the other factors (not considered) we expect the effect of the contraction to lay somewhere between Eqs. 17 and 19.

Returning now to the results, we note from inspection of Fig. 2 that the K&E design honeycomb attenuates a 5 percent turbulence level to 3 percent and that the turbulence level at the contraction is approximately 0.4 percent. Direct comparison cannot be made with Eqs. 17 and 19 since only the u component was measured. If for the sake of simplicity we assume isotropic turbulence at the outlet, then the ratios u_2/u_1 and q_2/q_1 are comparable. The attenuation for the nozzle is then 0.133 which is even better than predicted by Eq. 19, indicating that the test section turbulence is most probably anisotropic for this case. The finer cell size honeycomb (M = 1 in. or 25.4 mm) is more effective in attenuating turbulence (5 percent to 2.4 percent), but the resulting finer scale turbulence is not attenuated as effectively by the nozzle. The attenuation factor for the nozzle is now 0.208 and the turbulence level in the test section is slightly higher (0.5 percent). In any event neither combination of honeycomb and nozzle satisfies the design objectives.

Further insight into the mechanisms at play is found from inspection of Fig. 4. This shows that initially the u component of turbulence decays faster in the nozzle than rapid distortion theory predicts, and that a reduced level of turbulence persists further through the nozzle before other mechanisms take hold for the larger scale turbulence (M = 2 in.). The finer scale turbulence begins to increase in amplitude earlier in the nozzle, and, in fact, the turbulence level is higher at the exit than in the entrance. Keep in mind that only the u component was measured. Nothing can be said about the cross flow components.

This result is not unexpected; the rapid distortion theory would be expected to break down earlier in the nozzle for the finer scale turbulence.

The reason for initial reductions in turbulence level that are greater than predicted by rapid distortion theory is evident from inspection of Fig. 5. Here the turbulence level is plotted as a function of distance from the honeycomb. For up to about 120 cell sizes from the honeycomb, we see dissipation theory adequately predicts the attenuation in turbulence level. The curve drawn through the data is Eq. 7 with $c_1 = 0.219$. It should be noted that the relative position of the entrance and exit of the contraction is different for different values of M. Hence for $M = 2$ in. the data deviate early from the theoretical curve since the larger scale turbulence feels the effects of the nozzle at smaller values of x/M. It can also be conjectured from this plot that the effects of anisotropy and the return to isotropy are more strongly felt by the finer scale turbulence. In other words, the finer the scale turbulence, the more gradual is the contraction, and the effects of rapid distortion at the nozzle are not as strongly felt. Bear in mind that only u was measured. It could be conjectured that the finer scale turbulence is more isotropic at the nozzle exit, and the total turbulence level, q, may be less than the comparable level of the coarser grained turbulence.

To obtain further insight into the process of change in the turbulence through the contraction, velocity spectra were measured. The raw data are mean square intensity per unit frequency bandwidth or

$$\int_0^\infty S(f)\, df = \overline{u^2} \tag{20}$$

where $S(f)$ is the spectrum and f is frequency. Since the mean velocity varies through the contraction, comparisons are best made in terms of wave

number defined by

$$k = \frac{2\pi f}{U} = \frac{2\pi}{\lambda} \tag{21}$$

where λ is the wavelength of the turbulence. Further it should be kept in mind that an eddy of wavelength λ at the nozzle entrance assume a wavelength λ_2 at any axial position in the nozzle given by

$$\lambda_2 = c\,\lambda_1 \tag{22}$$

Therefore, energy concentrated at wavelength λ_2 was originally at a wavelength λ_1 or

$$k_2 = \frac{2\pi}{\lambda_2} = \frac{2\pi}{c\lambda_1} \tag{23}$$

Hence to compare energy at k_1, we should multiply k_2 by c, i.e.,

$$k_1 = ck_2 \tag{24}$$

Hence we seek spectra of the form

$$\int_0^\infty S(ck)d\,(ck) = \overline{u^2} \tag{25}$$

For convenience we normalize the spectra further with respect to $\overline{u^2}$ such that

$$\int_0^\infty S'(ck)d(ck) = 1 \tag{25A}$$

or

$$\frac{1}{u^2} \int_0^\infty \frac{U}{2\pi c} S(f)\, d\left(\frac{2\pi cf}{U}\right) = 1 \tag{26}$$

Hence we plot $US(f)/2\pi c\overline{u^2}$ as a function of $2\pi cf/U$; this is equivalent to S'(ck). It can be further shown [6] that the expected form of S'(ck) is given by

$$S'(ck) = \frac{2}{\pi ck_o}\left[1 + \left(\frac{ck}{ck_o}\right)^2\right]^{-1} \tag{27}$$

where

$$k_o \cong \frac{2\pi}{\ell} \tag{28}$$

Using Eq. 9 the expected value of k_o is

$$k_o = \frac{C}{\left(\frac{x}{M}\right)^{0.35} M} \tag{29}$$

Applying the model parameters for x, M, and c/we derive the value for k_o at the nozzle. Comparison of Eq. 27 with the data is given in Figs. 6 and 7. The turbulence spectra are predicted by this equation for the first part of the nozzle. The spectra deviate in the latter part of the nozzle adding further credance to the thought that the rapid distortion theory is breaking down.

In the latter part of the nozzle, it is expected that the efects of return to isotropy as well as dissipation are important. These effects, as well as the probably intrusion of turbulence generated in the boundary layers into the centerline flow and measured turbulence cannot be sorted out with the limited number of measurements made in this program.

V. CONCLUSIONS

Based upon the limits of the data gathered, the likelihood of attaining the design goal for turbulence intensity with the present configurations studied seems remote. Granted, the finer celled honeycomb is more effective in attenuating turbulence toward the inlet end of the contraction, but the honeycomb generated turbulence and the transfer between components as the flow continues through this relatively long contraction (relative with respect to eddy size versus distance travelled) sustains a, at least, constant fluctuation level. This leads to a dilemma in contraction design: Studies of flow uniformity support long nozzles, while turbulence criteria point toward a more favorable use of stilling sections and rapid contraction combinations.

Obviously, more study is warranted. As a bare minimum, one of the cross flow components should be measured, spectra should be determined across a given cross section, and various cross correlations should be made to determine the possible influence of viscous effects at the wall as well as the contamination of the measurements by sound. An exhaustive study of this problem is highly recommended to achieve the design goal.

REFERENCES

1. Hodgman, Charles D., Handbook of Chemistry and Physics, 38th ed., Chemical Rubber Publishing Co., Cleveland, 1956.

2. Prandtl, L., Attaining a Steady Air Stream in Wind Tunnels, NACA TM 726, 1933.

3. Tennekes, H. and Lumley, J. L., A First Course in Turbulence, MIT press, 1972.

4. Ribner, H. S. and Tucker, M., Spectrum of Turbulence in a Contracting Stream, NACA TN 2606, 1952.

5. Batchelor, G. K., Theory of Homogeneous Turbulence, Cambridge University Press, 1953.

6. Uberoi, M. S., "Effect of Wind-Tunnel Contraction on Free-Stream Turbulence," Jour. Aeronautical Sci., Aug., 1956.

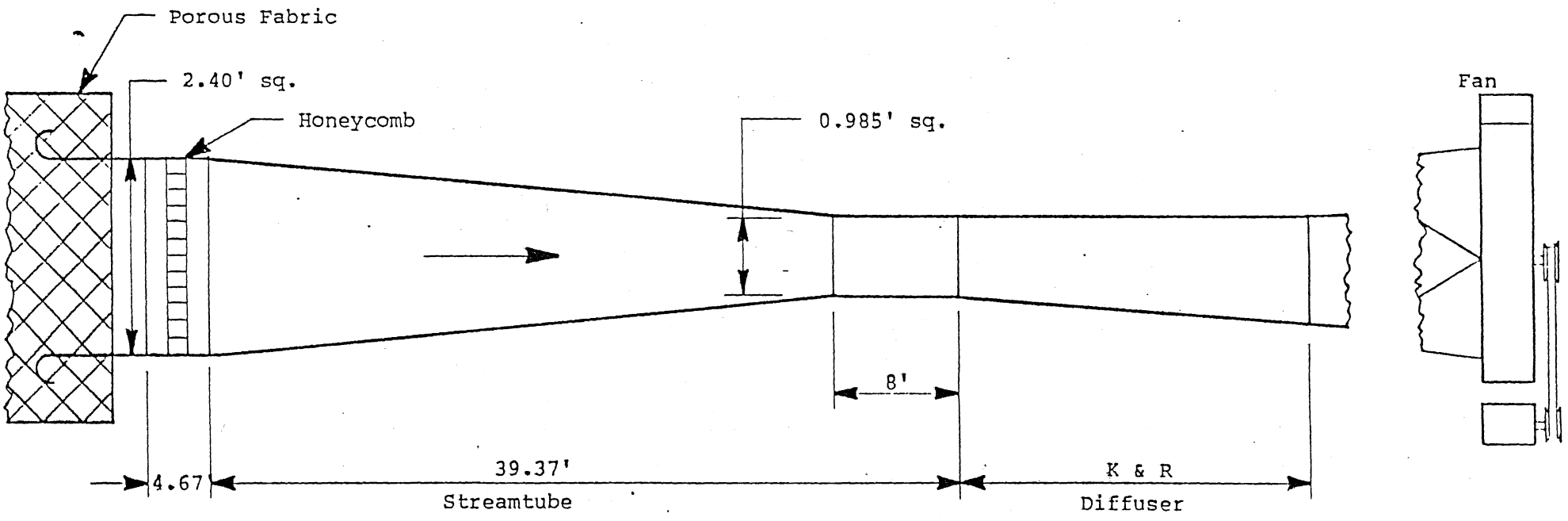

Not to Scale

Fig. 1 - Schematic of Streamtube Model.

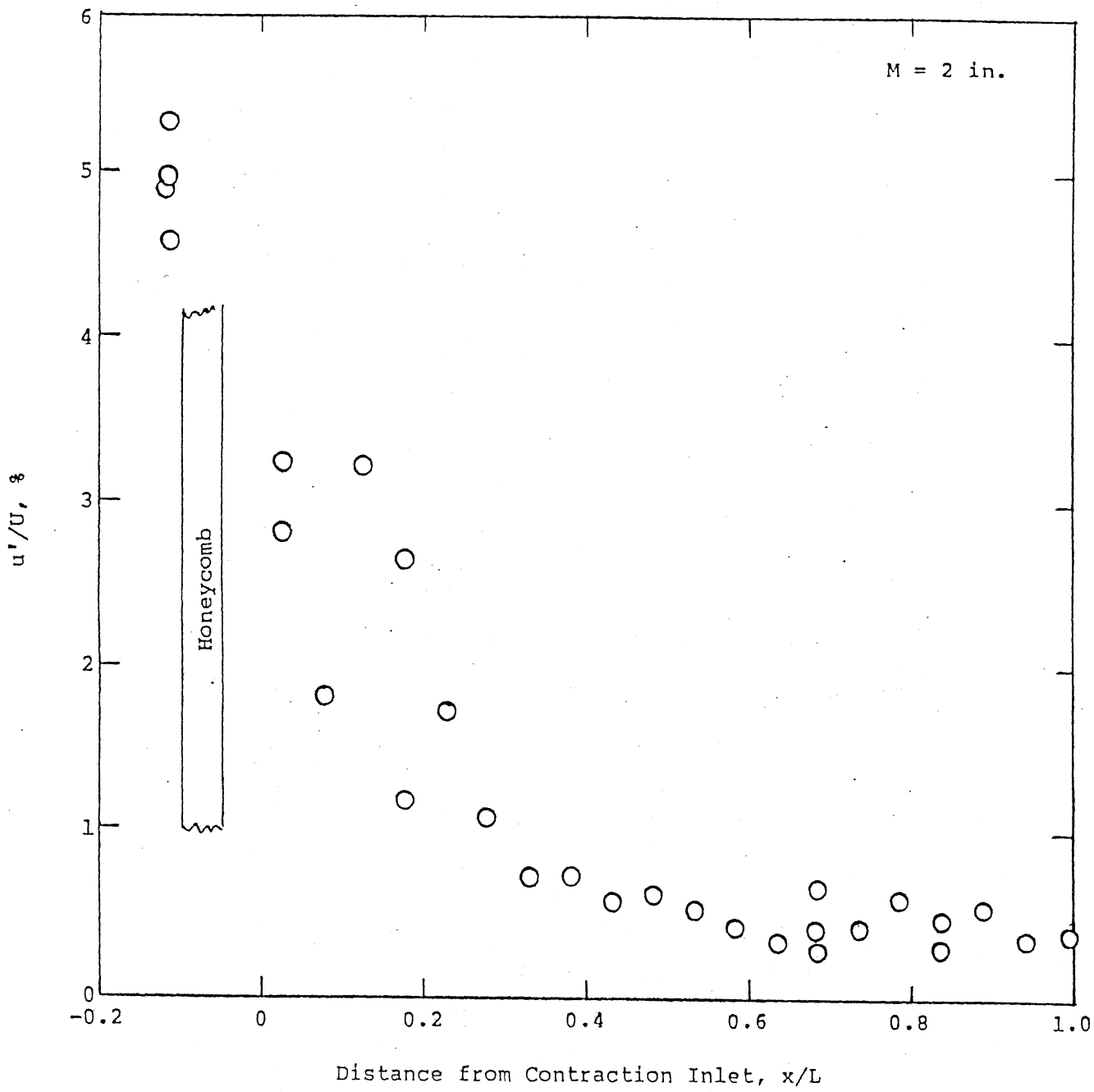

Fig. 2 - Variation of u'/U Based on Local Velocity Along Axis of Streamtube, M = 2 in.

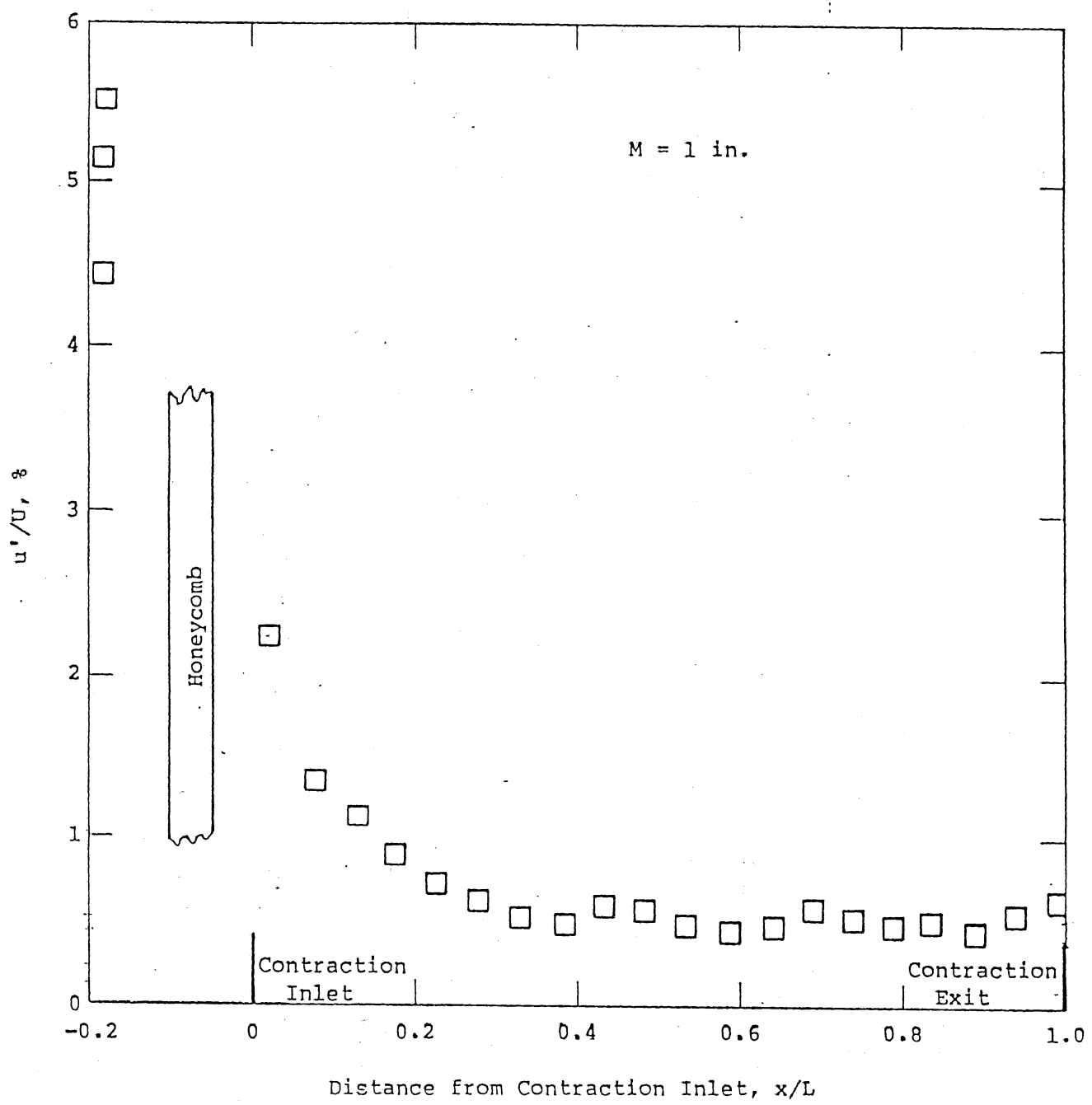

Fig. 3 - Variation of u'/U Based on Local Velocity Along Axis of Streamtube, M = 1 in.

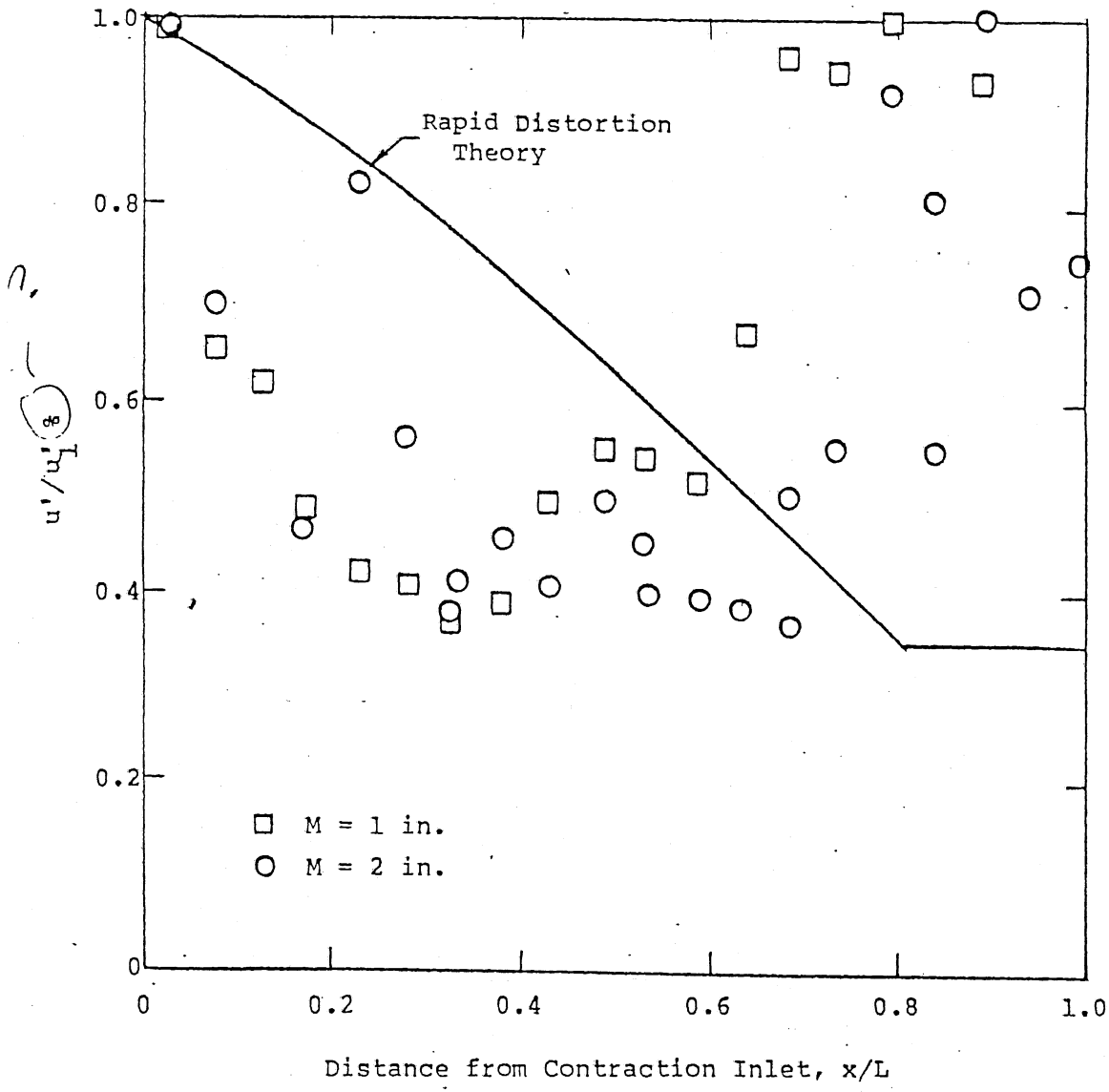

Fig. 4 - Local Turbulence Intensity Relative to Inlet Turbulence Intensity.

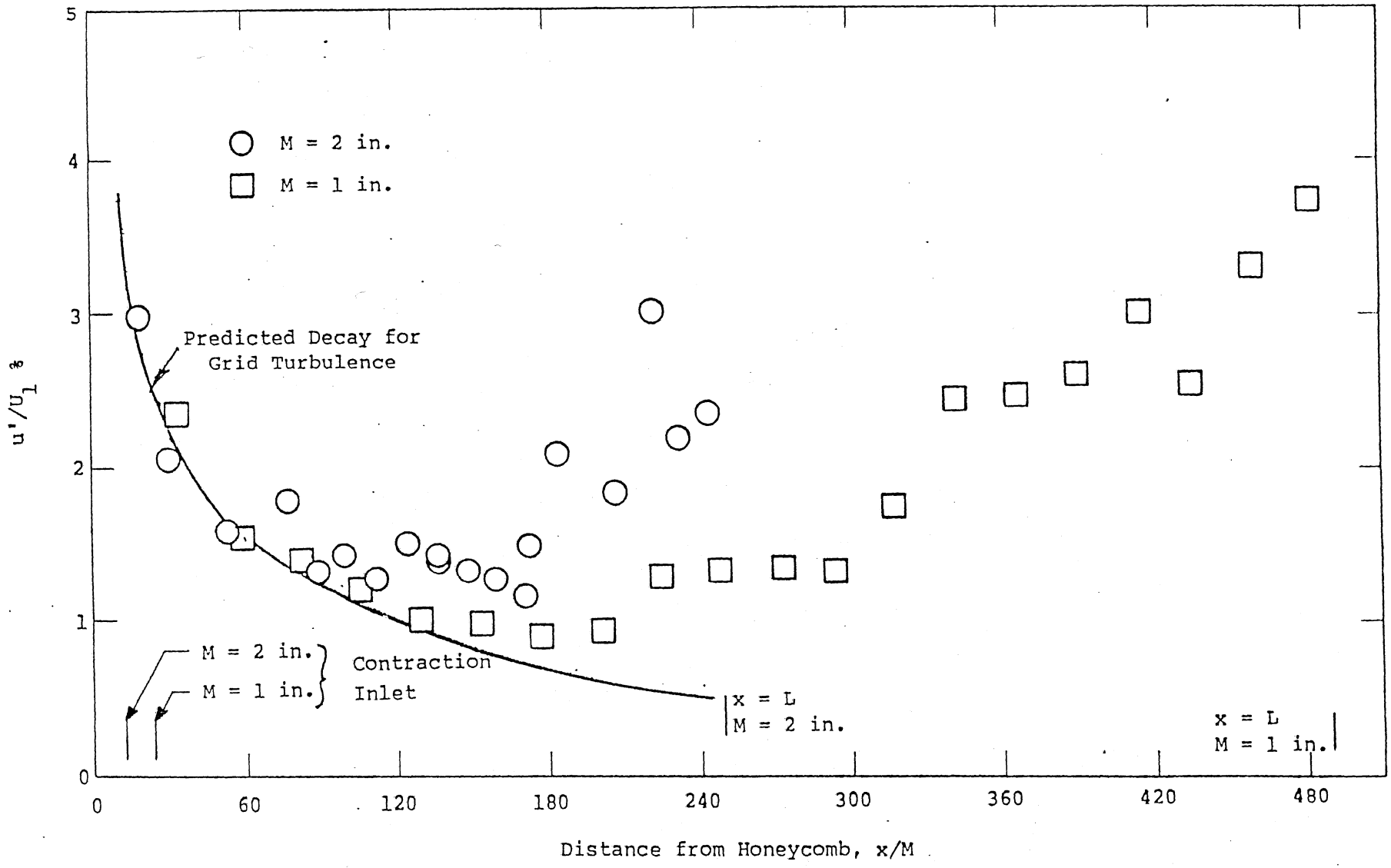

Fig. 5 - Local Turbulence Intensity Normalized to Inlet Average Velocity.

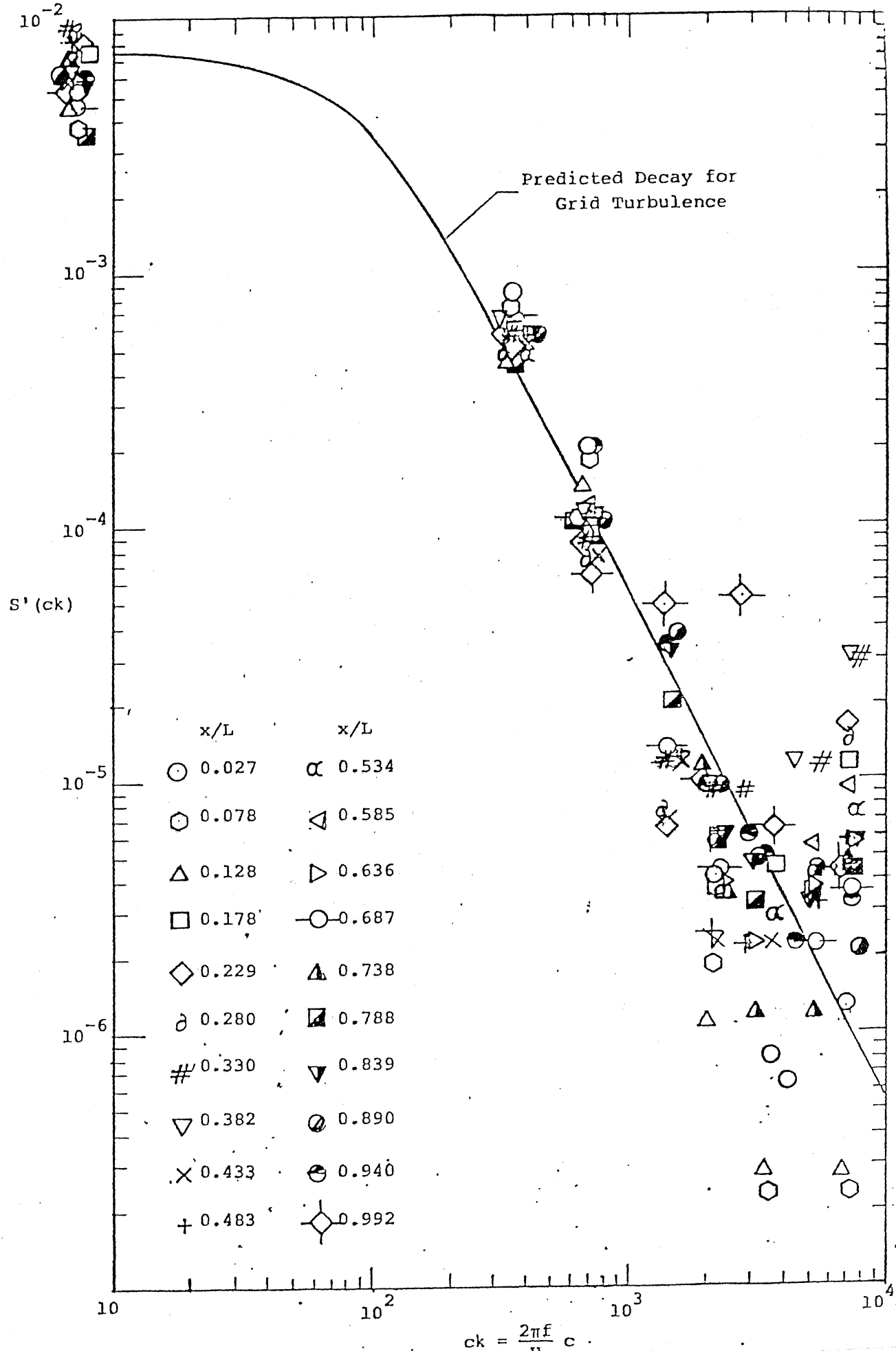

Fig. 6 – Unit Spectrogram

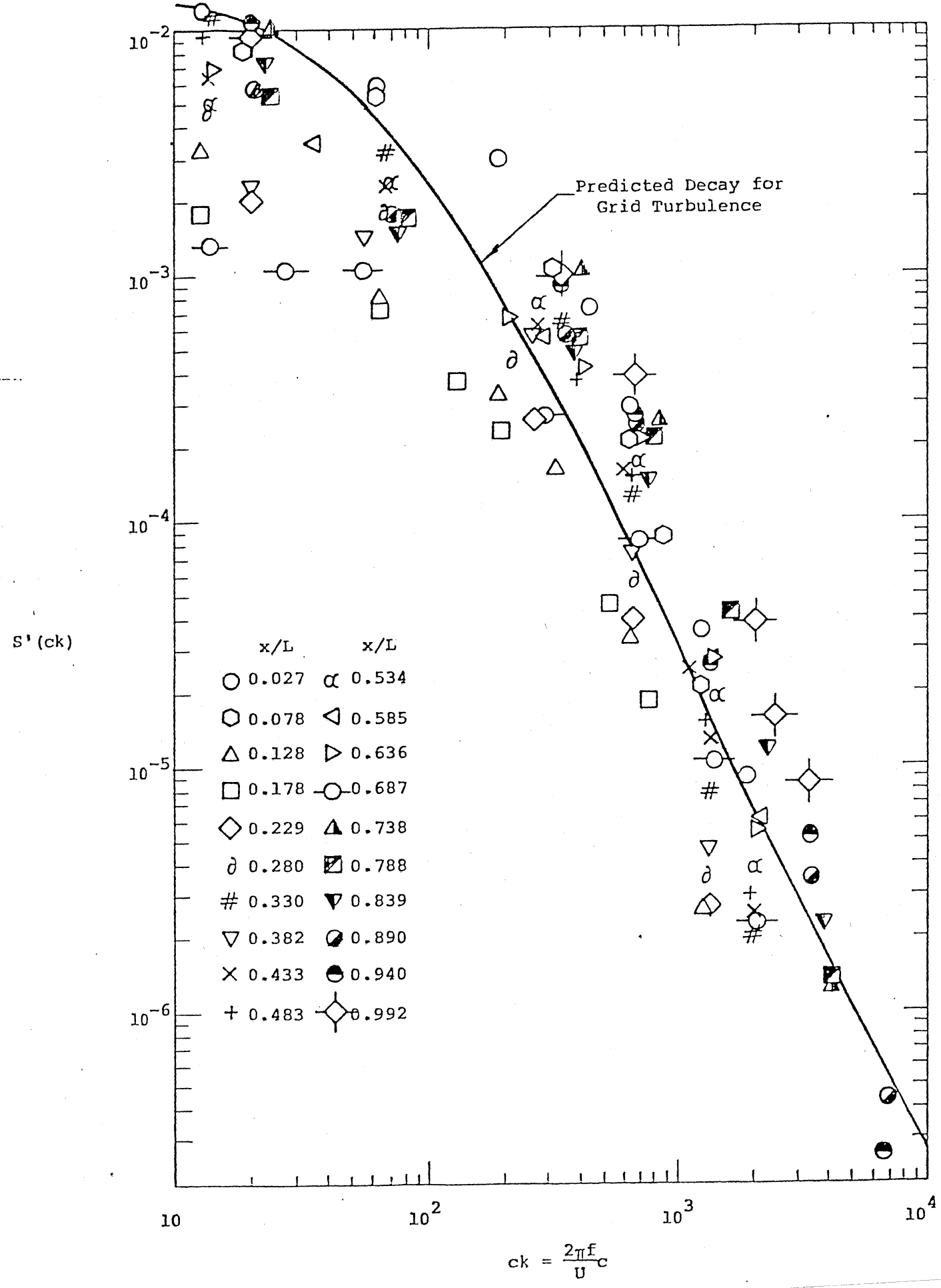
Predicted Decay for
Grid Turbulence
S'(ck)
x/L
x/L
0.027
0.078
0.128
0.178
0.229
0.280
0.330
0.382
0.433
0.483
0.534
0.585
0.636
0.687
0.738
0.788
0.839
0.890
0.940
0.992
10^{-2}
10^{-3}
10^{-4}
10^{-5}
10^{-6}
10
10^{2}
10^{3}
10^{4}
$ck = \frac{2\pi f}{U}c$

Final Report on Phase A-2, Task A:

Physical Modeling of the Kempf & Remmer Contraction, Test Section, and Diffuser

by

J. M. Wetzel, D. W. Bintz, R. E. A. Arndt,
and T. Morel

St. Anthony Falls Hydraulic Laboratory
University of Minnesota
Minneapolis, Minnesota 55414

Prepared for

SSV&K/DMJM:Joint Venture
1709 New York Ave., N.W.
Washington, D.C. 20006

July 1983

Task A: Physical Modeling of the Kempf & Remmer Contraction, Test Section, and Diffuser

by

J. M. Wetzel, D. W. Bintz, R. E. A. Arndt, and T. Morel*
St. Anthony Falls Hydraulic Laboratory, University of Minnesota

I. INTRODUCTION

A review of the preliminary Kempf and Remmers (K&R) design of the Large Cavitation Channel (LCC) resulted in some concern relative to the hydrodynamic performance of several components in the upper leg. These components included the contraction and diffuser. As the desired goals for velocity uniformity in the test section were demanding, it was felt that the contraction proposed by K&R should be evaluated for its adequacy. The contraction is of particular importance as its geometry has a direct impact on the physical size of the remainder of the flow circuit. The diffuser downstream of the test section is also a critical component, and preliminary estimates indicated that the diffuser contributed to about half of the head loss in the channel. Flow stability in the diffuser is required, and the shape of the velocity profile at its exit plane has a direct influence on the turning vane design of the first elbow. No experimental data were made available on the hydrodynamic characteristics of either of these two components. It was therefore deemed necessary to conduct small scale model studies to determine whether or not the test section performance goals could be actually achieved. As this information was urgently

---

*Presently with Integral Technologies, Incorporated.

needed, a mini-model was constructed at the Laboratory to provide the necessary data. Time did not permit the in-depth study that would have been desirable. Therefore, the study was limited to items considered to be most significant and that would impact on the overall design features. Results from the physical model were also to be used to verify the mathematical model of the contraction which was being developed in a parallel program. The comparison of results from the two models is discussed in Task B. A description of the physical model and the experimental data are discussed in the following sections.

II. THE PHYSICAL MODEL

A 1 to 10 scale model of the contraction, test section, and diffuser was constructed based on the geometry of the preliminary K&R design. Dimensions were taken from Kempf and Remmers' Drawing No. K37-SK2, dated July, 1981. To reduce both hydrodynamic loads and power requirements, air was used as the working fluid rather than water. A sketch of the test apparatus is shown in Fig. 1, and an overall photo of the installation is shown in Fig. 2a. Air is drawn through the system by means of a variable speed fan. A large housing with dimension of about 8x8x8 ft constructed of light steel framing surrounds the inlet. This framing was covered with a porous fabric as seen in Fig. 2a, and its purpose was to isolate the inlet from external flow disturbances at the site and to prevent ingestion of foreign particles into the flow. A rounded inlet was fabricated from 10 inch diameter plastic pipe cut along a diameter. These half sections were mitered at the corners and attached to a sheet metal entrance section with a square cross section as shown in Fig. 2b. Some entrance length was provided upstream of the contraction to permit installation of screens for distortion of the inlet velocity profile.

The contraction itself was fabricated with sheet metal sides and bottom, and the top was transparent Lucite to permit observation of small tufts attached to the boundary. A photo of the contraction top is shown in Fig. 2c. The white dots on the left side indicate locations of pressure taps. The contraction shape conforms to templates based on the K&R equations for the sides and bottom. The contraction was followed by a Lucite test section of scaled length. The test section is shown in Fig. 2d with corner fillets installed.

Care was taken in fabrication and assembly to ensure a good match between the contraction and test section elements.

The diffuser transition was made of Lucite in two section. The first section has a constant width and a curved bottom. The second section has a straight bottom and the two side walls are curved to meet the remainder of the straight walled diffuser itself. Dimensions were held to close tolerances to avoid any mismatch between the components. After final fitting, the flanges were pinned so that sections could be removed and reinstalled without changing the alignment. A short section of constant area follows the diffuser and terminates in a square to circular transition leading to the section opening of the fan. A foam rubber insert has been installed between the square and transition section to reduce transmission of fan vibration to the remainder of the system. The components downstream of the diffuser are not part of the K-R design, and their only purpose is to provide a stable flow into the fan.

A total of 108 pressure taps have been installed in the contraction. The 1/16 in. diameter holes were drilled normal to the boundary. These taps have been placed in three rows of 36 taps each along the longitudinal centerline of the bottom surface, and near the corners at the bottom and top surfaces. The taps were more closely spaced near the entrance and exit of the contraction as these regions were considered to be critical areas. Twenty four taps were intalled in a single row along the longitudinal centerline of the bottom surface of the test section. In the diffuser, a total of 101 taps have been placed along the top and bottom longitudinal centerline and along the top corner. Some taps were also placed along the centerline of the curved sidewall of the second transition section. The large number of taps was chosen to detect possible flow separation.

Fx	3.64e+003	-3.64e+003	Mx	0	0
Fy	-1.28e+004	1.28e+004	My	0	0

A series of pressure taps were connected to three Scanivalves with ten ports each. Pressure differences were measured with a calibrated Validyne pressure transducer and a micromanometer. Calibration of the pressure transducer was checked frequently during a test run against a known column of water. To eliminate the effects of slight changes in flow conditions during a test, each data point was nondimensionalized with a dynamic reference pressure recorded at the same time.

Provisions were made for measuring mean velocity profiles in horizontal and vertical planes at several locations. These locations were 1.4 ft upstream of the contraction entrance, in the test section (4, 46, and 95 percent of the test section length) and at the exit of the diffuser. The measurements were made on centerlines with a 0.25 in. diameter Pitot cylinder spanning the entire width of the section. A wall tap was generally used as the reference static pressure, although a static pressure probe on the centerline was used with skewed inlet profiles. The position of the probe with respect to the wall was measured with a calibrated apparatus incorporating an optical encoder with a digital voltmeter readout.

The initial data were collected without the corner fillets installed. This was done to permit a direct comparison with the first version of the mathematical model of the contraction, which was run without fillets. Fillets were later added as shown in Fig. 2. It should be noted that the corner fillets with a 20 inch radius of the preliminary K&R design have not been used. Other design considerations for the test section have led to a change in fillet geometry from a curved to a triangular fillet with a diagonal length of about 21.5 in. This triangular or beveled fillet was therefore used in the model throughout the contraction, test section, and diffuser.

III. DISCUSSION OF RESULTS

A. Test Section Mean Velocity Profiles

One of the first items of interest was the uniformity of the flow velocity in the test section. Vertical and horizontal velocity profiles were measured on the axial centerline at three distances downstream of the test section entrance. During the preliminary tests with the facility, it was noted that the flow velocity at a given point varied slightly over a period of time. This variation was probably associated with minor changes in the rotational speed of the fan or other outside influences. As the time period was on the order of the time required to make a velocity traverse across the test section, it was necessary to continually monitor a reference pressure so that the time variation in flow velocity could be detected. For this purpose, the wall pressure difference between the inlet and exit of the contraction was used as a measure of the overall flow steadiness. This value was recorded at the time of each velocity measurement. Final data were reduced using the corrected velocity at the centerline as the reference value.

The experimental data are plotted in Figs 3 to 5 in dimensionless form. Note that the location of the measuring station is given as x/L_T, where x is the longitudinal distance downstream of the beginning of the test section, and L_T is the length of the test section. Two sets of symbols are shown for each profile. Open symbols represent data taken with the probe traversing the section from either the bottom to the top or the left to right side wall. After reaching the far wall, the pressure transducer was recalibrated, and the probe progressively moved back to its original position. The latter data points are

indicated by the filled symbols. The velocity profiles are remarkably flat; and the variation is within plus or minus one percent of the centerline velocity, excluding the boundary layer regions.

These velocity profiles were taken without the corner fillets installed so that a direct comparison could be made with the first version of the mathematical model as described in Task B. The velocity profiles at the entrance to the contraction were essentially uniform as shown in Fig. 6. These profiles were measured on centerlines at $x/L_c = 1.36$, when x is the distance from the contraction exit (positive in the upstream direction) and L_c is the length of the contraction. The inlet of the contraction is therefore at $x/L_c = 1.0$.

After the corner fillets were installed in the contraction, test section, and diffuser, measurements of the vertical velocity profiles were repeated at two locations in the test section. These profiles are shown in Fig. 7; and as expected, the experimental data are essentially the same as that previously shown without fillets. The velocity profile at the contraction inlet was also that shown in Fig. 6.

Although it may be expected that the eventual installation of turbulence management honeycombs upstream of the contraction will tend to improve the uniformity of the velocity profile at the inlet to the contraction, it was felt necessary to determine the influence of a nonuniform inlet profile on the velocity distribution in the test section. To distort the inlet profile, No. 15 mesh screens were installed near the inlet. A total of six layers of screens was used, and the length of each layer was varied in an attempt to establish a near linear distribution of velocity in a vertical plane from the top to the bottom of the contraction inlet. After several trials, the centerline velocity distribution shown in Fig. 8 was obtained and was considered adequate for the

purpose. The velocity varied by a factor of about two from top to bottom, with the higher velocity at the bottom. Measurements of the vertical velocity profile on the longitudinal centerline just downstream of the contraction exit are also shown in Fig. 8. The profile is skewed with slightly higher velocities at the bottom than the top, but still is within acceptable limits. These profiles were taken without the corner fillets.

The same set of screens was removed from the inlet and inverted to provide a profile with higher velocities at the top than the bottom. The inlet and test section velocity profiles are shown in Fig. 9. In this case, an additional velocity profile was taken near the middle of the test section. Again, some of the distortion of the inlet profile is observed in the test section profiles, although the magnitude has been satisfactorily reduced by the contraction. The profiles shown in Fig. 9 were taken after the corner fillets were installed.

B. Contraction Boundary Pressures

The evaluation of the hydrodynamic performance of the K&R contraction design is based on two criteria. These criteria are the capability of creating a highly uniform exit velocity profile, and freedom of boundary layer separation in the inlet region. The previous discussion on test section velocity profiles leads to the conclusion that the contraction ratio is adequate to provide good flow uniformity.

The subject to be addressed is that of the boundary pressures. It is well known that the boundary pressures deviate from those obtained by a simple application of the Bernoulli equation and the equation of continuity. As a uniform flow approaches the contraction, the streamlines are straight and parallel. In the region of boundary curvature, the curvature of the streamlines is achieved by a reaction force on the solid boundary. This results in a

pressure rise at the wall near the inlet, which diminishes with increasing distance along the contraction. The opposite trend occurs near the contraction outlet. Here the reverse curvature of the boundary results in a pressure dip followed by a rise in pressure to the exit valve. If the magnitude of these adverse pressure gradients is excessive, boundary layer separation and eddies can form which can influence the overall performance of the contraction.

As no experimental data were available for the K&R contraction design, measurements of the boundary pressures were made in the 1 to 10 scale model. Wall pressures were measured along the longitudinal centerline of the bottom surface, near the intersection of the bottom surface and vertical side wall, and near the intersection of the side wall and flat top surface. Pressures in the corner were measured without the corner fillets installed. The primary purpose of the corner pressure measurements was to determine the extent of three-dimensionality of the flow.

Experimental data taken with a near uniform inlet velocity profile are shown in Figs. 10 and 11. Pressure differences were measured between points on the boundary and the entrance to the test section. These pressures were normalized with the pressure difference measured between the contraction inlet and exit. The latter pressure difference is a measure of the average dynamic test section pressure. As the flow varied slightly during a test run, both pressure differences were measured for each tap location to eliminate the effect of drift on the readings. The horizontal scale is based on the distance, x, measured from the contraction exit, divided by the length of the contraction, L_C. The contraction exit is therefore at $x/L_C = 0$, and the contraction inlet at $x/L_C = 1.0$. The origin for x is the same as for the mathematical expression for the boundary curvature.

The plotted curve represents the pressure variation calculated using the Bernoulli equation and equation of continuity. The previously mentioned deviations of boundary pressures from this curve near the inlet and exit of the contraction are clearly seen. Data taken near the top and bottom corners are plotted in Fig. 11. The pressure coefficients at the bottom corner are essentially the same as at the bottom centerline. Some differences are noted for the top corner, particularly near the contraction exit. These differences are probably due to the three-dimensionality of the flow.

In Fig. 12, wall pressure data for the bottom centerline have been replotted using a different definition for the pressure coefficient. Wall pressure differences are now related to the inlet wall pressure. This pressure difference has been divided by a reference dynamic pressure based on the inlet flow velocity. The inlet flow velocity was determined from the measured pressure difference between the contraction inlet and exit. Application of the contraction area ratio then provided an average inlet velocity. In this manner of plotting, the pressure rise is exaggerated and more clearly evident. The magnitude is about 0.4 of the inlet velocity head. The data do not indicate that boundary layer separation has taken place. Small tufts were attached to the boundary at many locations, and observations of the tufts were not conclusive. Some fluttering of the tufts was noted near the maximum pressure region, although no evidence of flow reversal was detected.

Boundary pressures on the bottom centerline were also measured with nonuniform inlet velocity profiles. The wall pressures taken with an inlet profile with velocities higher at the bottom than the top (see Fig. 8) are plotted in Fig. 13. In Fig. 14, the inlet velocity profile has higher velocities at the top than the bottom (see Fig. 9). When plotted in terms of test section parameters, little influence of the inlet velocity profile is

noted, although pressures near the contraction outlet are slightly lower than for the uniform inlet flow.

The same data have been replotted using inlet parameters in Figs. 15 and 16. In Fig. 15, the magnitude of the pressure rise has increased to about 0.65 of the inlet velocity head. Recall that the definition of the pressure coefficient is based on the average velocity head, and the differences may be associated with this definition applied to the case of a skewed inlet velocity profile. With the inlet velocity skewed in the opposite direction, the data of Fig. 16 show that the magnitude of the maximum pressure coefficient is less and is essentially constant over a short region. This type of trend is that expected by boundary layer separation. Boundary tufts in this region tended to be inactive and appeared to lie in a dead zone. The contraction may be sensitive to inlet profiles of this type. Further discussion on this matter is continued in the Task B and Task C reports, in which modifications to the K&R contraction design are suggested.

C. Diffuser

The purpose of the diffuser is to reduce the high velocity in the test section to a value more compatible with other components of the recirculating system. This velocity reduction cannot efficiently be achieved by a simple increase in area. The distance over which the area change occurs, and thus the diffuser angle, are also significant parameters. As the area increases and the velocity decreases, the pressure increases in the direction of the flow. The adverse pressure gradient can result in separation of the flow at the boundary. Large increases in head loss are associated with separation, and the entire diffuser flow may be unstable. Proper diffuser design will reduce the chances of these adverse flow characteristics from occurring.

Diffuser geometry is also important in that the head loss in the component is unsually a significant percentage of the head loss in the entire flow circuit. In addition, the velocity profile at the exit of the diffuser is usually quite nonuniform, and this nonuniformity influences the hydrodynamic performance of downstream components. The design of the turning vanes in the first and second elbow to adequately turn the flow and remain cavitation free is dictated by the diffuser outflow. It has been observed that nonuniformity of the inflow to the pump can be traced directly back to the diffuser.

For maximum diffuser efficiency, it is well known that the included angle of a diffuser should be about 5 to 7 degrees. Smaller angles necessitate excessively long diffuser lengths to achieve a specified area change and the wall friction becomes relatively large. Larger angles result in a shorter diffuser, although flow separation and instability may occur. The diffuser incorporated in the preliminary K-R design has a modest angle and area change; however, it is not symmetrical.

To avoid abrupt changes in slope at the entrance to the diffuser, a curved transition is introduced. In the LCC the transition is divided into two sections so that the bottom and sidewall curves do not occur in the same element. With a symmetrical diffuser, the curve of the upper surface is most important, as the pressure decrease to the curvature may lead to cavitation at high speeds and low test section pressures. The LCC diffuser has a flat upper surface which relieves this problem. The bottom transition curve is quite long and gradual, and the pressure drop may not be significant.

Few experimental data could be found in the literature which applied to the diffuser proposed for the LCC; measurements were made of velocity profiles and boundary pressures to aid in the overall performance evaluation. Velocity profiles were measured at the exit plane of the diffuser along centerlines in

both the horizontal and vertical directions. Before the data are presented, several comments should be made about the data reduction.

During a test run, the velocity varied slightly with time. As with the previously described measurements, the pressure difference between the inlet and exit of the contraction was used as a reference. This pressure difference is also a measure of the average dynamic pressure of the test section flow by including the area ratio of the contraction, and can be converted to an average test section velocity. The calculated velocity was used as a reference for each measurement taken for the velocity profile. The contraction pressure difference varied about 3 percent over the duration of time required for a velocity transverse. To obtain the average velocity at the diffuser exit, the average value of the reference velocity was divided by the area ratio of the diffuser.

The experimental data for the vertical and horizontal velocity profiles taken with corner fillets installed are shown in Figs. 17 and 18. It should be noted that the vertical velocity profile is not symmetrical about the centerline, with slightly higher velocities at the top than at the bottom. This asymmetry is not unusual, but can have some impact on flow uniformity at the pump intake. More complete symmetry is observed in the horizontal profile which may be expected as the diffuser is symmetric in plan form. Both velocity profiles are quite peaked with the maximum velocity about 1.7 times the average velocity as defined above.

A vertical velocity profile taken without the corner fillets is shown in Fig. 19. This profile is essentially the same as that with fillets, although the velocities are slightly lower in the lower half of the diffuser.

Variation of the boundary centerline pressures along the diffuser bottom, curved side wall, and top are shown in Figs. 20 and 21. The pressure difference between any point and the diffuser inlet has been referred to the test

section dynamic pressure as determined from the pressure drop across the contraction. The location of each pressure tap is given by the distance, x, measured from the diffuser inlet, divided by the total length of the diffuser, L_d.

The influence of the curved bottom surface in the first transition can be seen in the bottom pressures of Fig. 20. A drop in pressure occurs over a short distance before the pressure starts to rise. The magnitude of this pressure drop is about 0.05 times the test section dynamic pressure. For a 30 knot test section velocity, the minimum pressure head is about 2 ft of water less than the inlet pressure head. This is probably not excessive.

The side wall pressures do not indicate any pressure drop due to curvature. The pressure distribution along the top centerline of the diffuser shown in Fig. 21 is essentially the same as for the bottom, except that the pressure drop in the region of the first transition is not present. The wall pressures do not indicate that boundary layer separation has occurred in the diffuser.

The head loss in a diffuser is commonly determined on the basis of average velocities at the inlet and exit of the diffuser, and the pressure rise between these two planes [1]. If the loss coefficient, K_D, is defined as a fraction of the inlet dynamic pressure, then

$$K_D = \frac{\text{LOSS}}{\frac{1}{2}\rho \overline{V}_T^2} = -C_p + 1 = \frac{1}{AR^2}$$

where $C = \dfrac{P_e - P_T}{\frac{1}{2}\rho \overline{V}_T^2}$

P_e = exit pressure

P_T = inlet pressure

$\overline{V}_T$ = average inlet velocity

AR = diffuser area ratio

The value of C_p can be taken from Fig. 21 as 0.71, and with an area ratio of 3.12 for the case without corner fillets, K_D is calculated to be 0.187. The Reynolds number based on the inlet height of the diffuser is about one million for these tests, which should be sufficiently high to avoid any significant effects of Reynolds number. The loss coefficient used by Kempf and Remmers was about 0.12, which is considerably lower. Measurements of the total pressure rise were also made after the corner fillets were installed. The average of four measurements yielded a C_p of 0.75. The area ratio was changed slightly with fillet addition, and as the fillet size was the same in both the test section and diffuser, the test section area was reduced more than the diffuser exit area. Using an area ratio of 3.19, the loss coefficient is calculated to be 0.15, somewhat lower than without fillets.

Diffuser loss coefficients are better determined by including the nonuniformity of the velocity profiles. This is done by applying a so-called kinetic energy correction factor to the velocity heads based on mean velocities. The expression for K_D then is given by

$$K_D = - C_p + \alpha_T - \frac{\alpha_e}{AR^2}$$

where $$\alpha = \frac{\int V^3 dA}{A\bar{V}^3} > 1$$

and the subscripts T and e refer to the inlet and exit as before. For a uniform velocity profile, $\alpha = 1$, and the expression for K_D reduces to the first expression given.

The kinetic energy correction factor, α, is determined by integration of the velocity field. It is obvious that an extensive mapping of the velocity field is required for this computation. Time did not permit obtaining such a

detailed survey in this investigation, but a crude evaluation of α_e was made using the two available profiles. Numerical integration yielded a value of about 1.25. As the inlet velocity profile was essentially flat, a value for α_T of 1.01 was assumed. The resulting loss coefficient, using C_p of 0.75 is 0.137.

It should be emphasized that estimating loss coefficients for components in close proximity to each other is subject to some error. Downstream conditions can influence the pressure recovery of a diffuser, and it is difficult to establish loss coefficients for interacting components without modeling the entire flow circuit.

IV. CONCLUSIONS

Based on the experimental study conducted with mini-models of the preliminary design of the K&R contraction and diffuser, several conclusions are appropriate. More complete data on component interaction awaits the availability of the 1 to 5 scale model of the entire flow circuit.

1. Measurements of vertical and horizontal mean velocity profiles at various positions along the longitudinal centerline of the test section indicated good flow uniformity. The variation of velocity across the test section was within the desired plus or minus one percent of the centerline velocity, excluding the boundary layer regions. Some distortion of the velocity profiles was observed with skewed velocity profiles upstream of the contraction, although the resulting nonuniformity still appeared to be acceptable. A contraction ratio of about six is judged to be adequate to meet the performance specifications for mean velocity profiles.
2. Contraction boundary pressures measured along the bottom centerline have indicated a small pressure drop near the exit end of the contraction. This is not considered to be significant. A pressure rise was noted just downstream of the contraction inlet which could lead to boundary layer separation. Separation was observed with a skewed inlet velocity profile which had a lower velocity at the bottom than the top. The pressure rise and tendency for separation can be considerably reduced by modifying slightly the bottom curve of the

contraction inlet region to provide more modest curvature. This is further discussed in the Task C report.

3. The boundary pressures along the longitudinal centerlines of the diffuser did not indicate any flow separation. A pressure drop was noted along the curved bottom of the first transition but did not appear to be excessive.

4. The vertical mean velocity profile at the centerline of the diffuser exit plane exhibited some nonsymmetry. Velocities were slightly higher at the top than the bottom of the diffuser. The horizontal mean velocity profile at the same plane was symmetrical. The ratio ofthe maximum to average velocity was about 1.7. These velocity profiles did not appear unusual for a diffuser of this geometry.

5. The diffuser loss was higher than expected. Addition of corner fillets reduced the loss coefficient, but it was still higher than the estimated loss coefficient for the K&R diffuser. As the pressure rise along the diffuser may be influenced by downstream components which were not modeled in this investigation, firmer values will be obtained in the 1 to 5 scale model.

IV. REFERENCES

1. Miller, Donald S., "Internal Flow - A Guide to Losses in Pipe and Duct Systems," British Hydromechanics Research Association, Cranfield, Bedford, England, 1971.

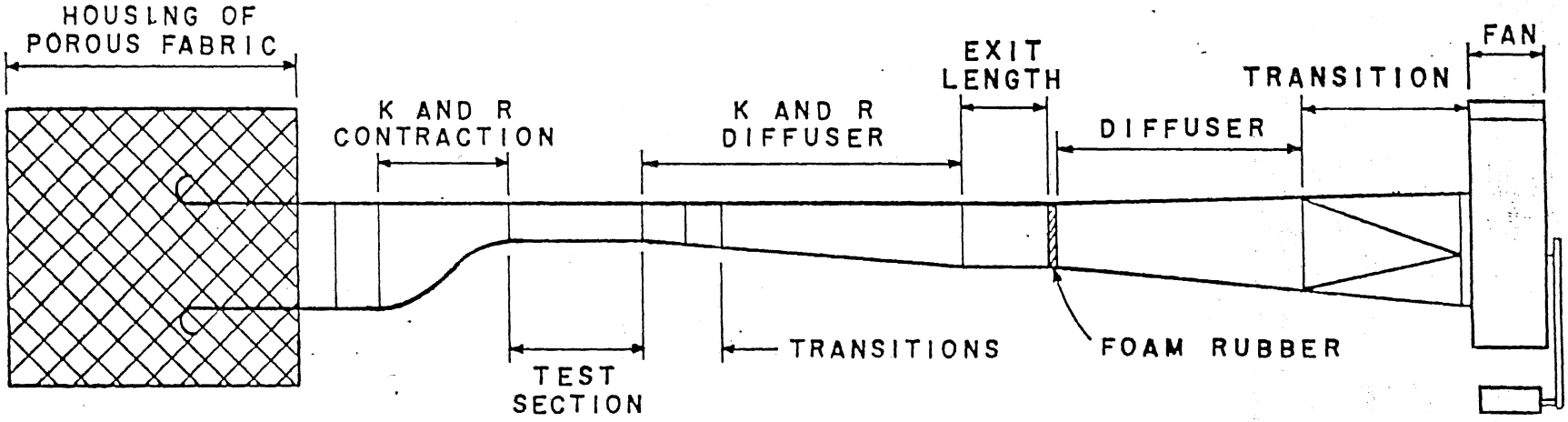

FIG. 1 - SCHEMATIC OF 1:10 PHYSICAL MODEL

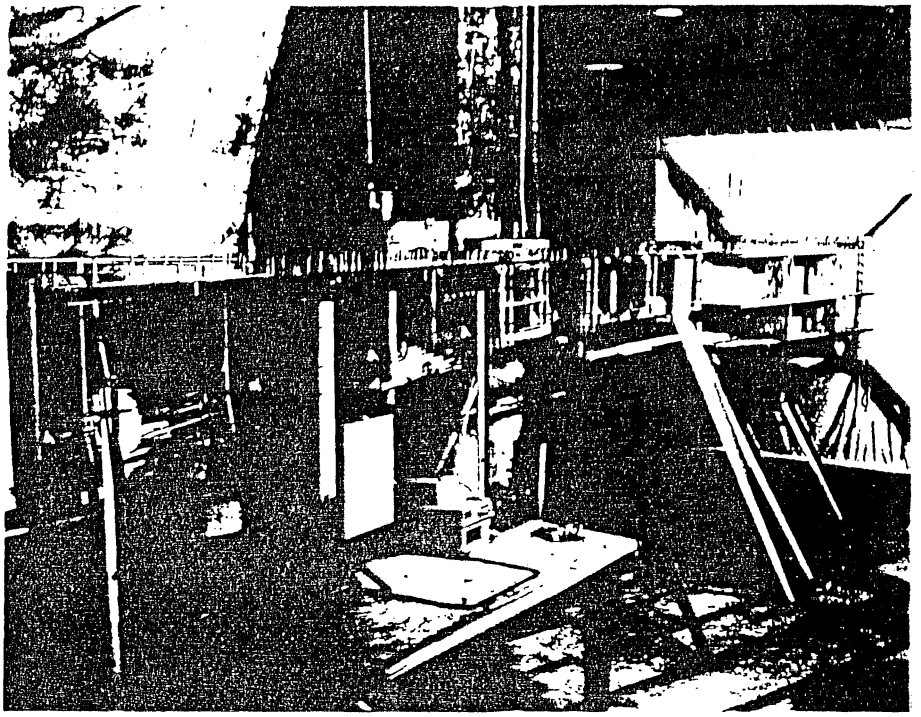

a) Overall view of test apparatus.

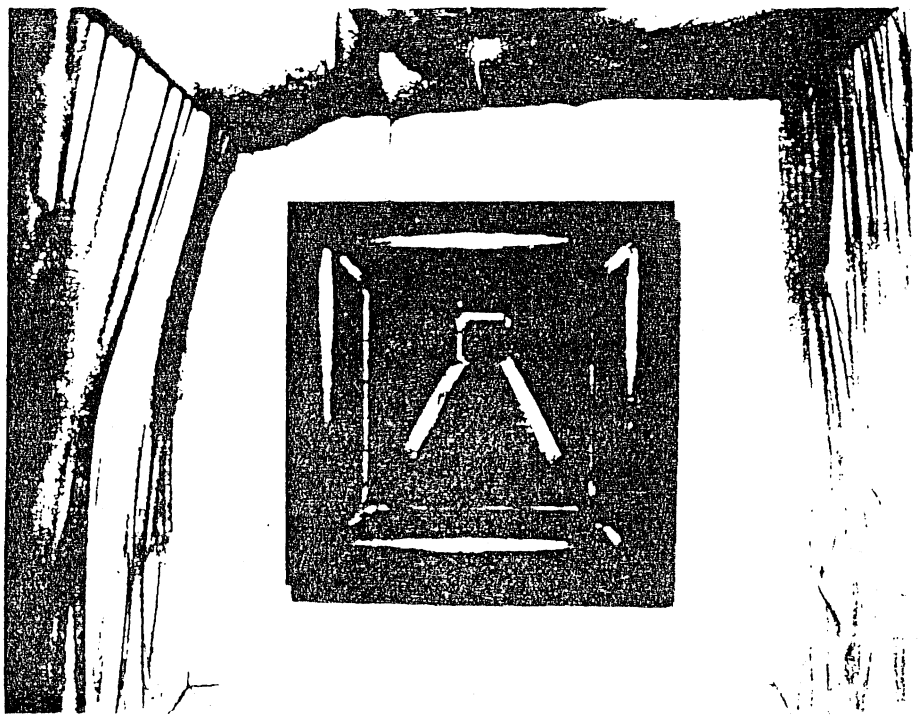

b) Contraction inlet inside bay house.

Fig. 2. Photos of test facility. (cont'd)

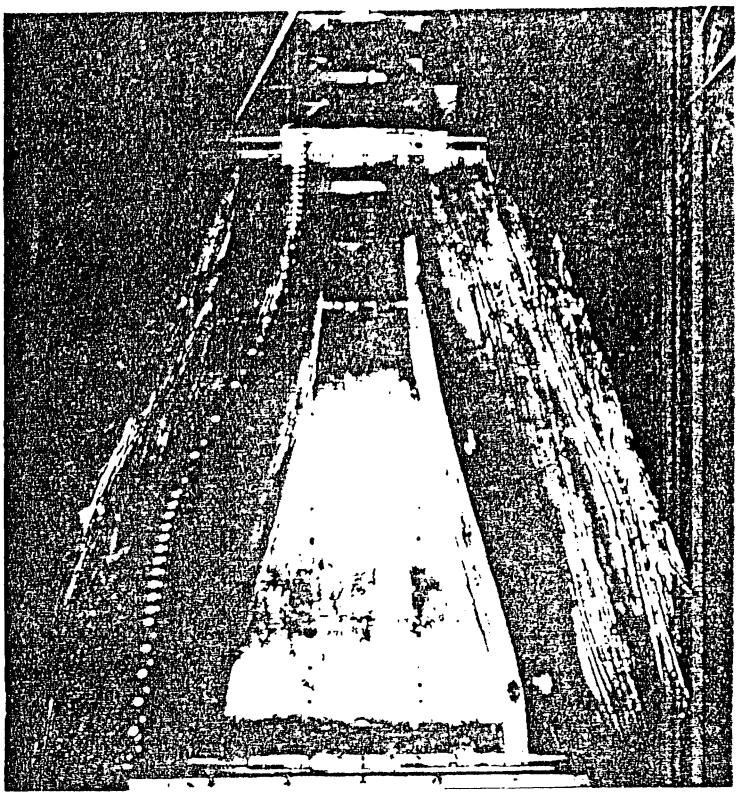

c) Top view of contraction.

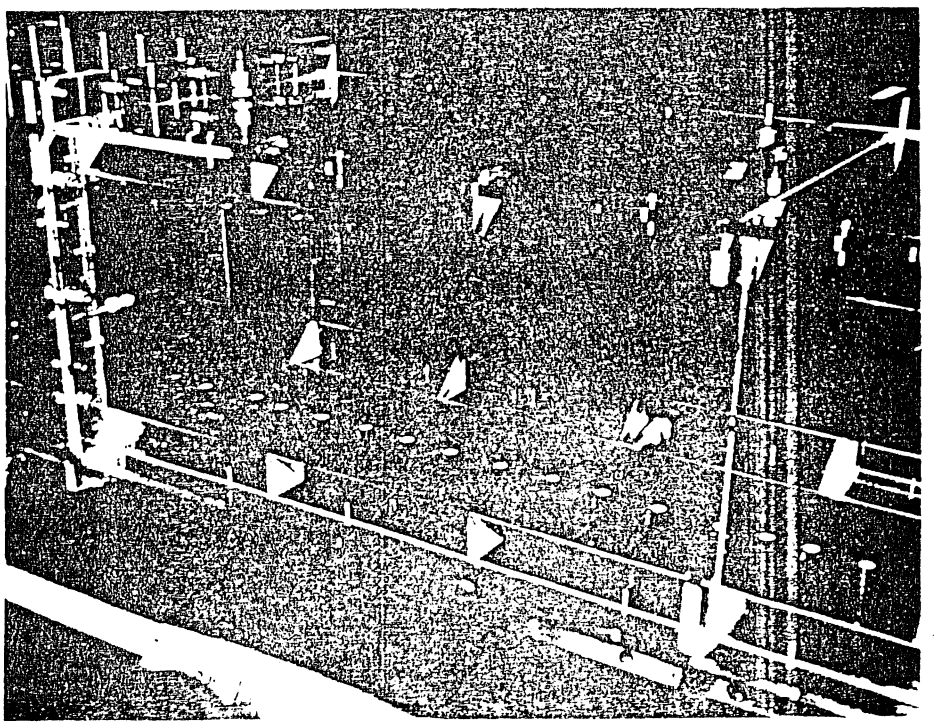

d) Test section with corner fillets.

Fig. 2 (Cont'd). Photos of test facility.

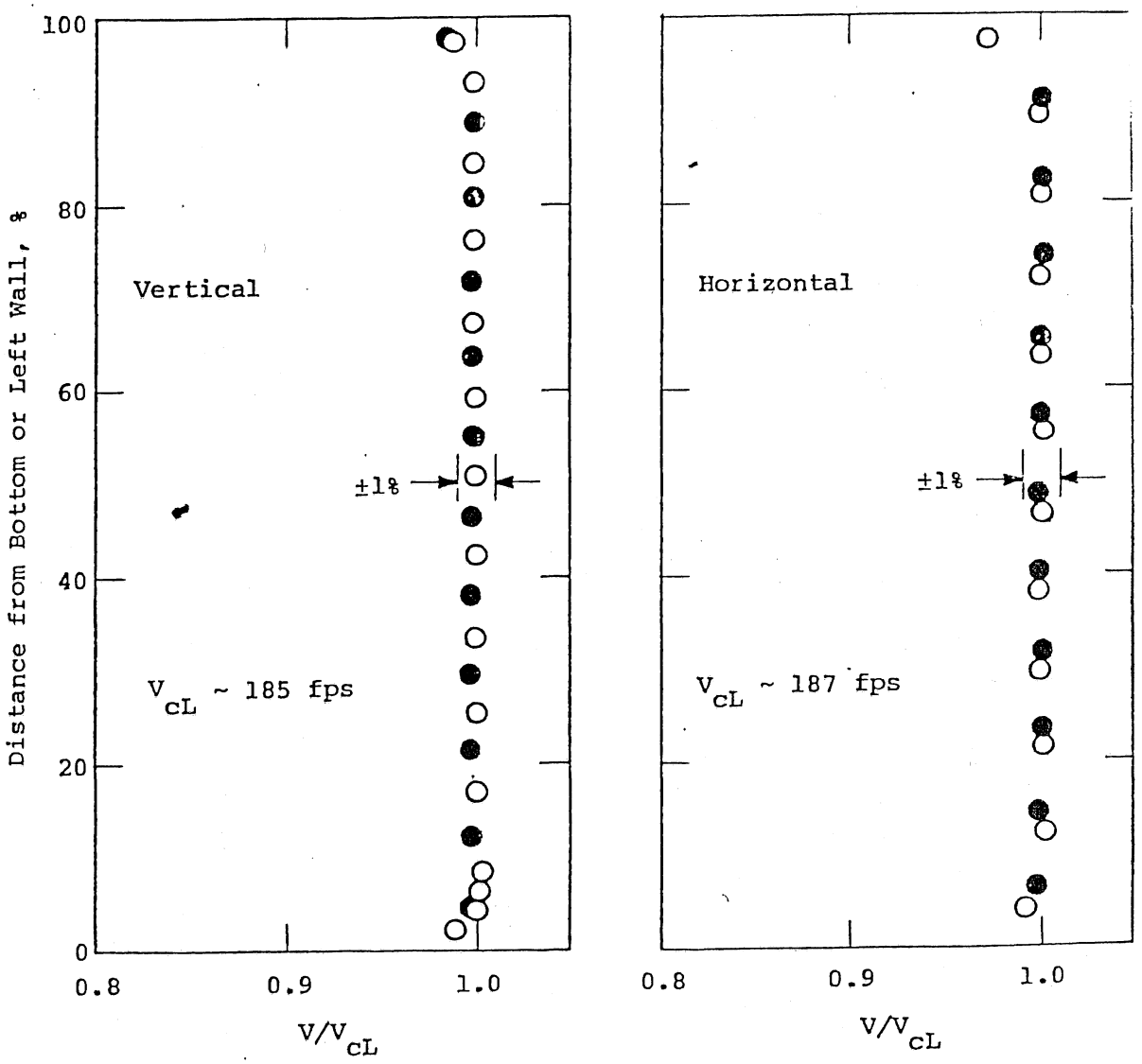

Fig. 3 - Test Section Velocity Profiles at $x/L_T = 0.04$.

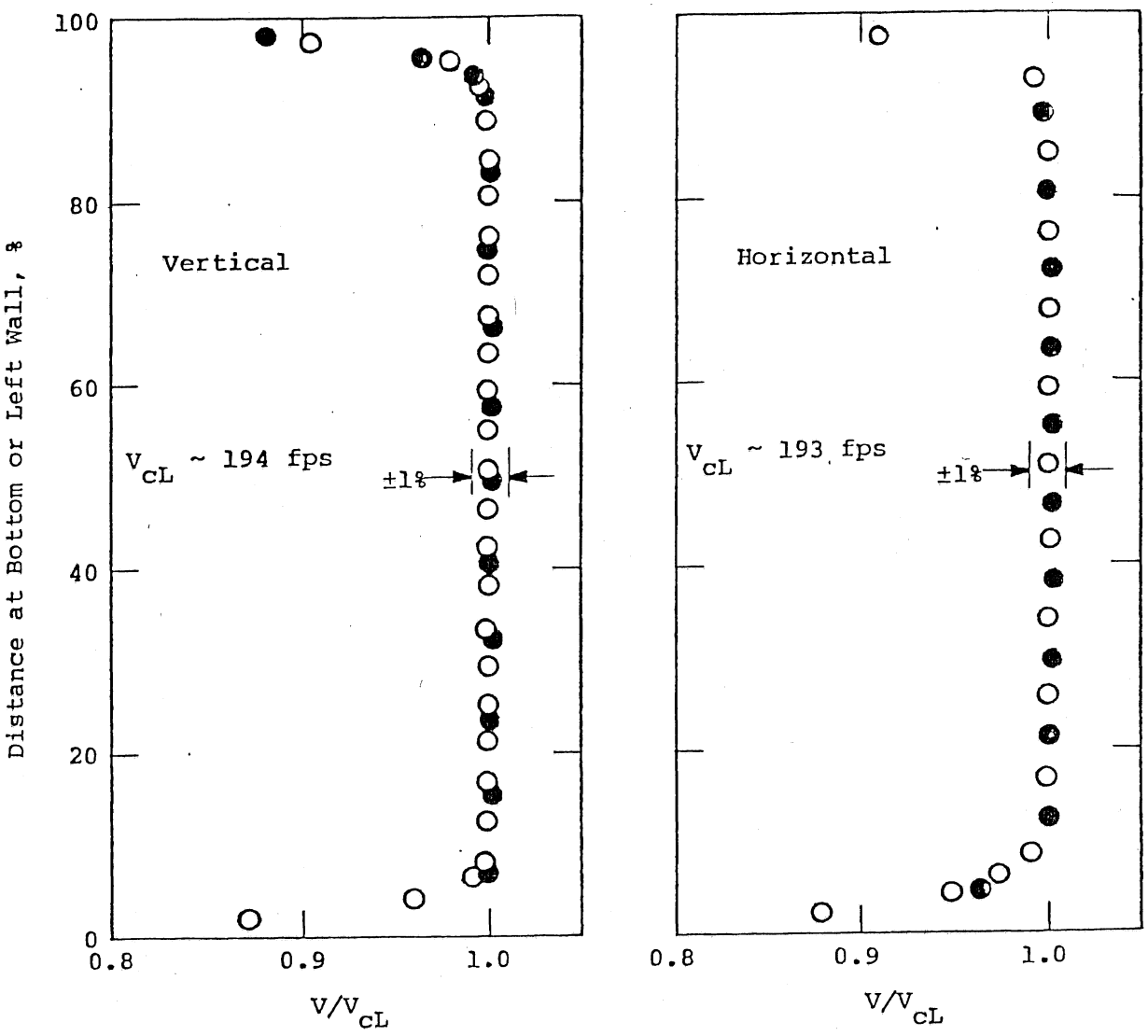

Fig. 4 - Test Section Velocity Profiles at $x/L_T = 0.46$.

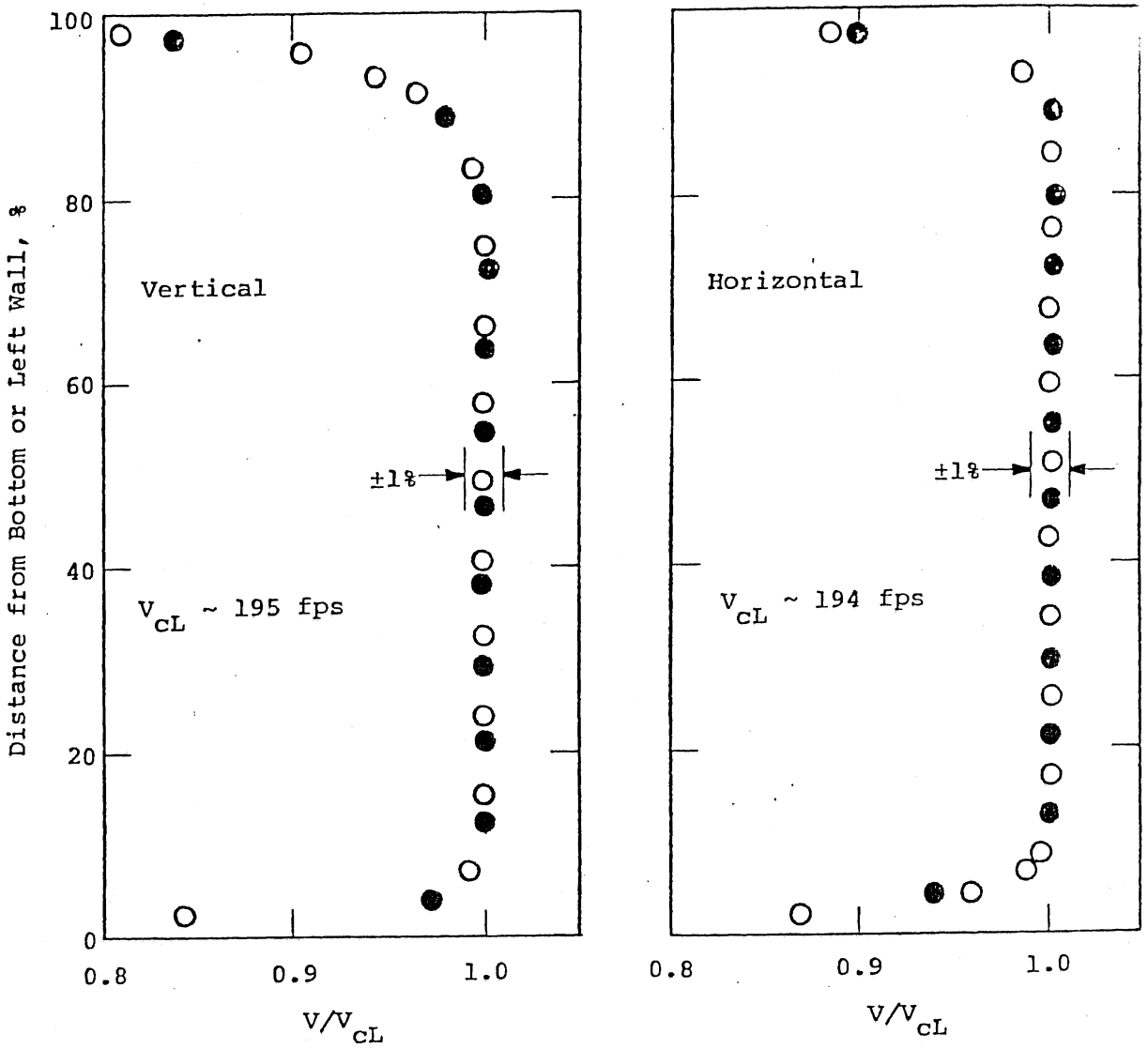

Fig. 5 - Test Section Velocity Profiles at $x/L_T = 0.95$.

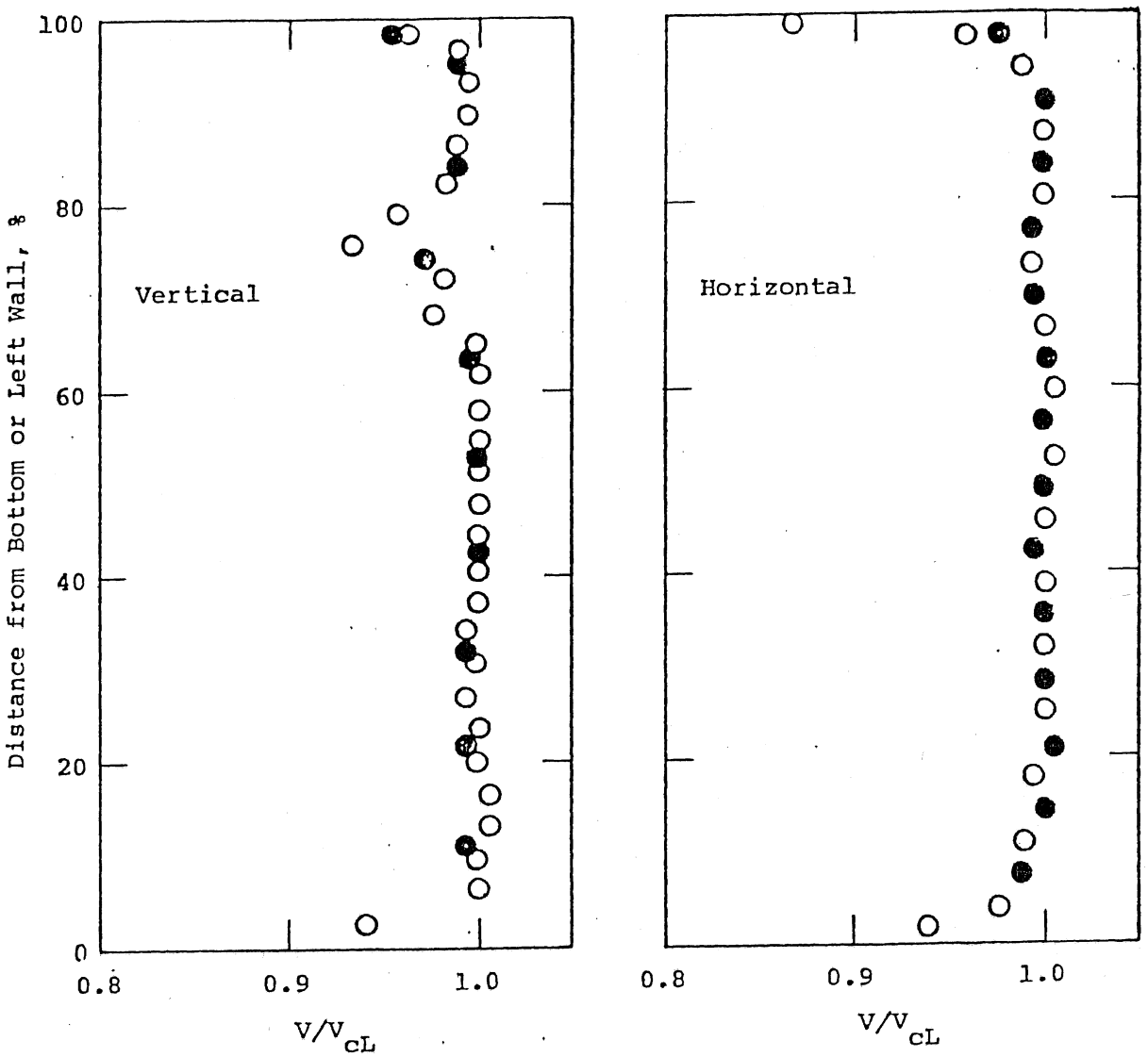

Fig. 6 - Velocity Profiles at Contraction Inlet, $x/L_c = 1.36$.

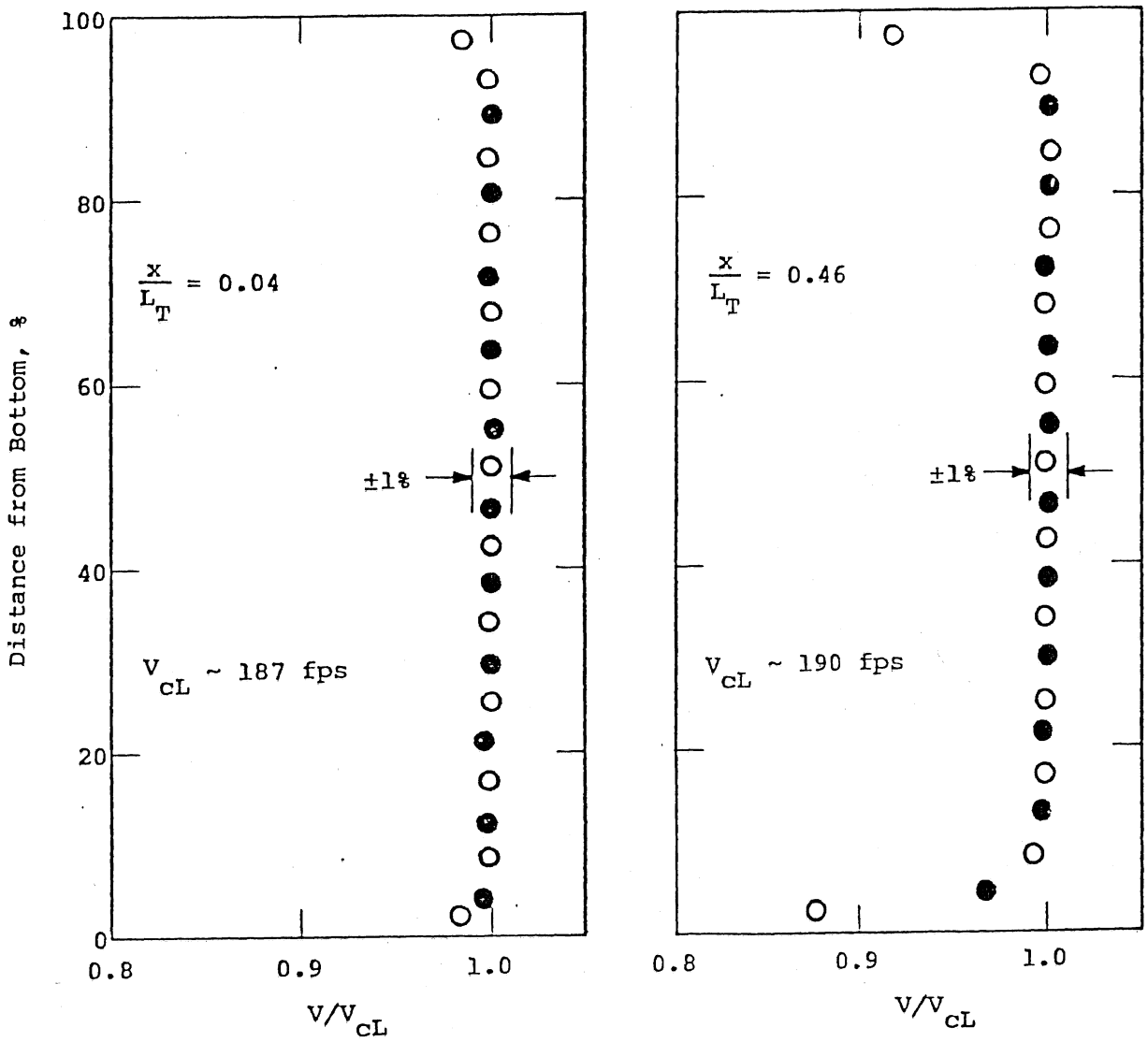

Fig. 7 - Vertical Velocity Profiles on Centerline in Test Section, Uniform Inlet Profile, with Fillets.

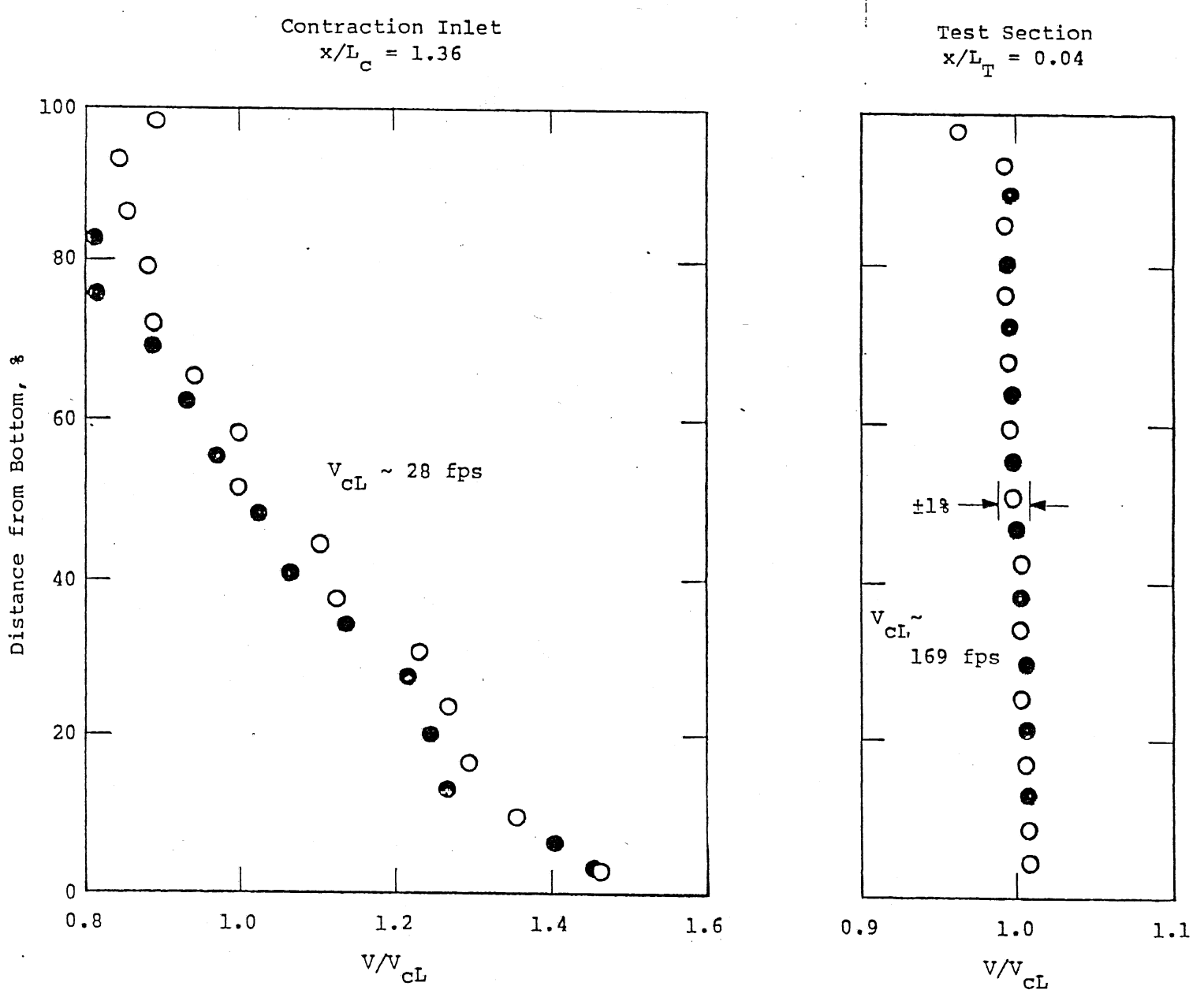

Fig. 8 - Vertical Velocity Profiles on Centerline, Skewed Inlet Profile No. 1.

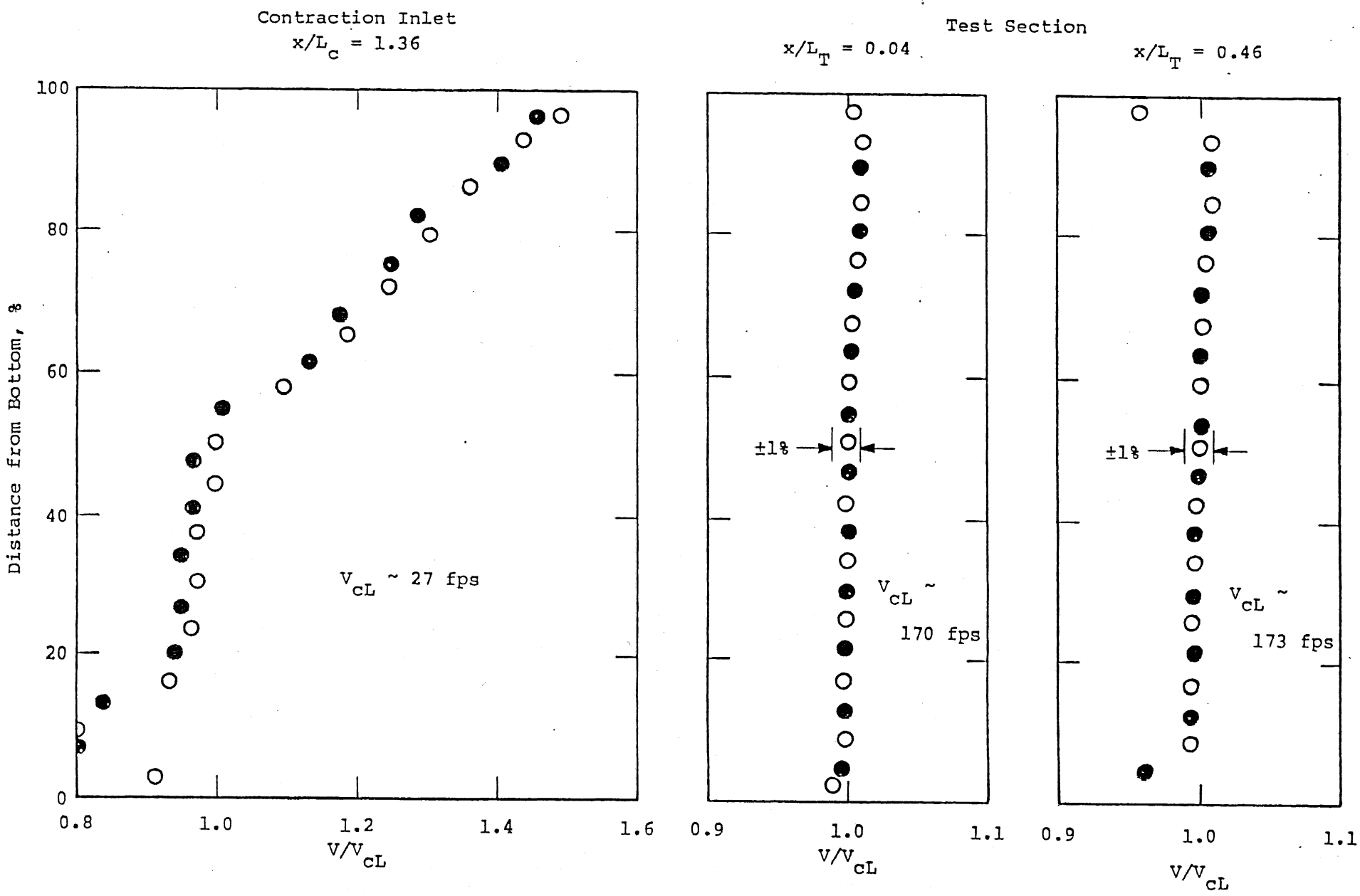

Fig. 9 - Vertical Velocity Profiles on Centerline, Skewed Inlet Profile No. 2.

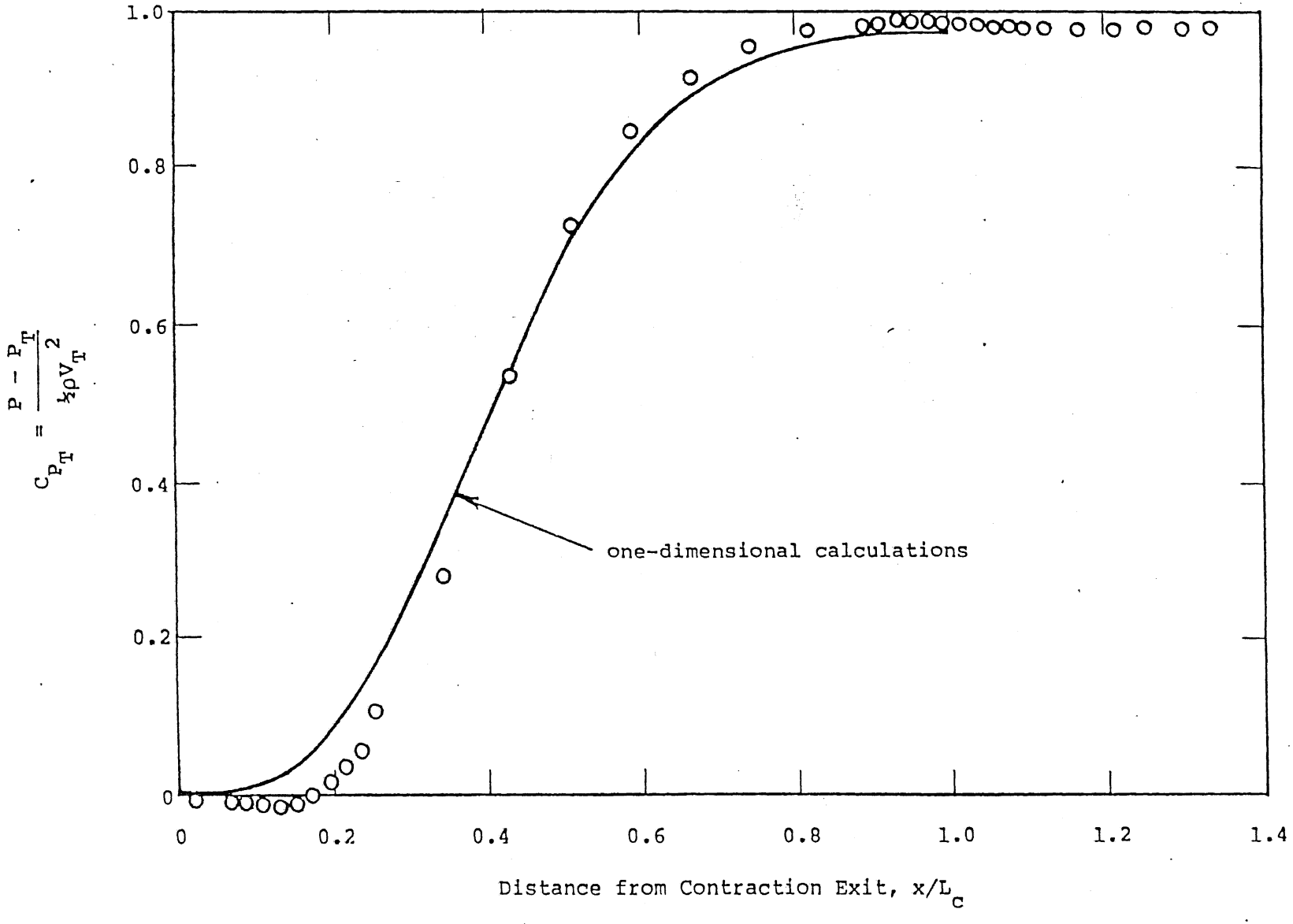

Fig. 10 - Contraction Wall Pressures, Bottom Centerline, Uniform Inlet Velocity Profile

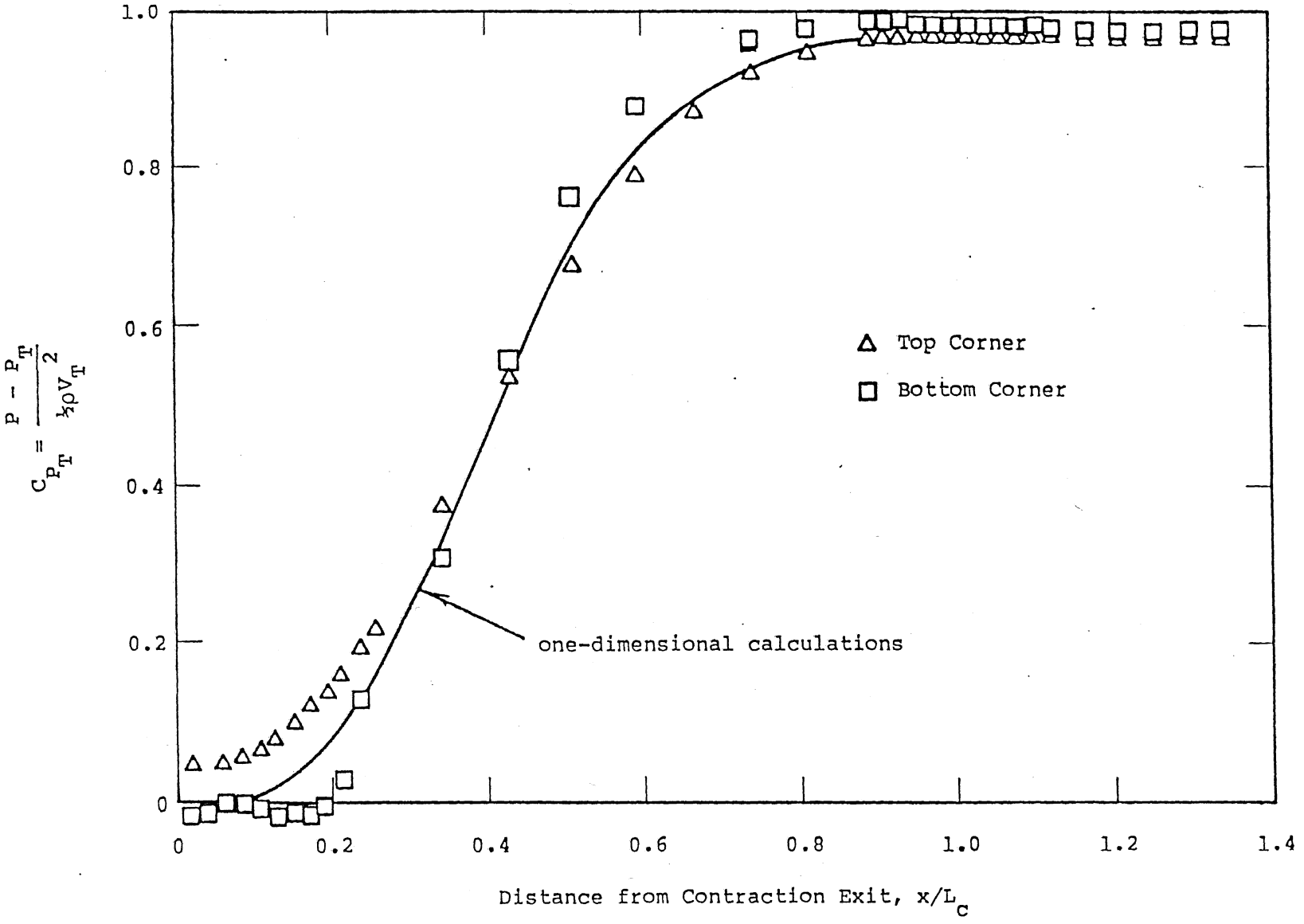

Fig. 11 - Contraction Wall Pressures, Bottom and Top Corners, Uniform Inlet Velocity Profile

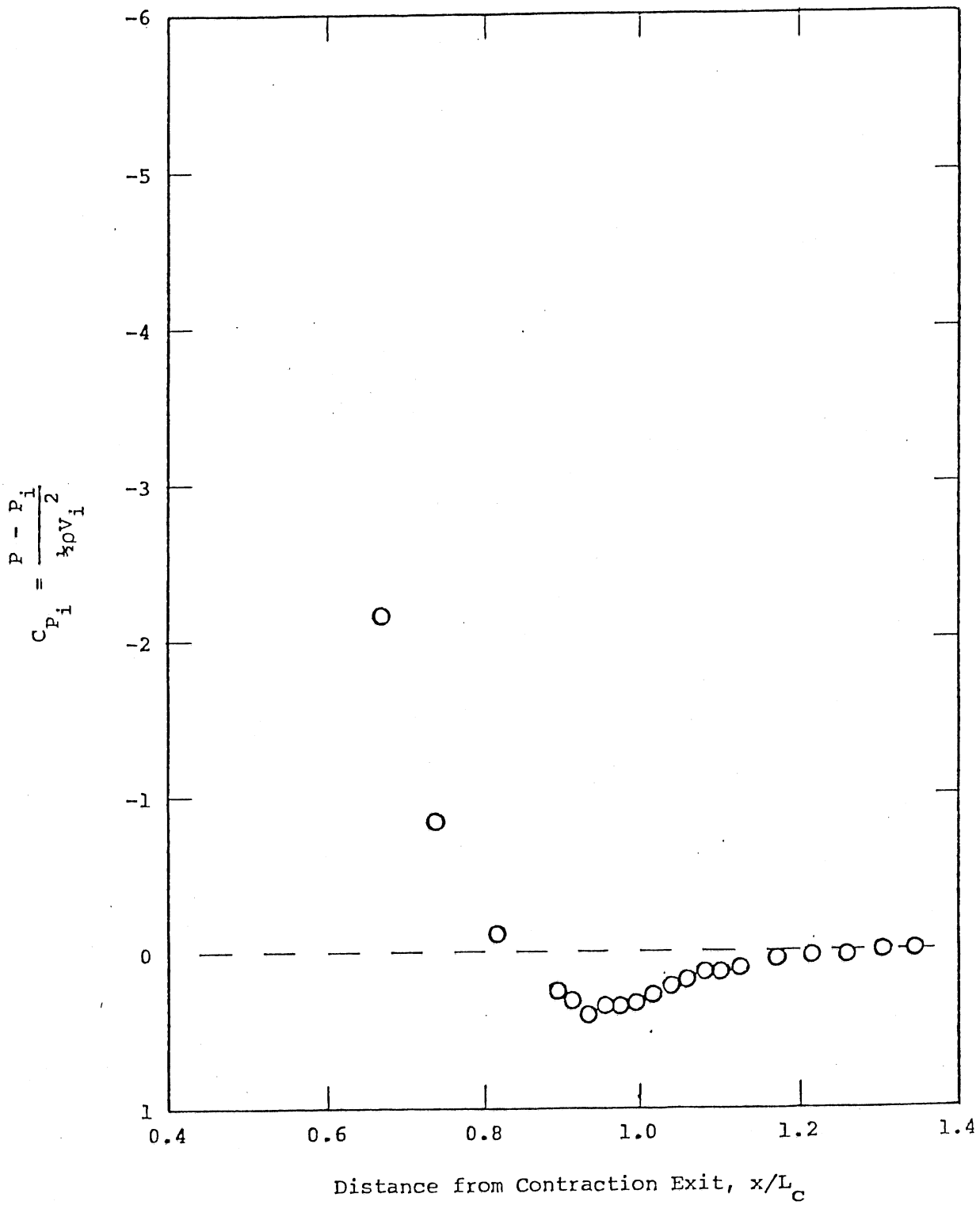

Fig. 12 - Contraction Wall Pressures, Bottom Centerline, Uniform Inlet Velocity Profile.

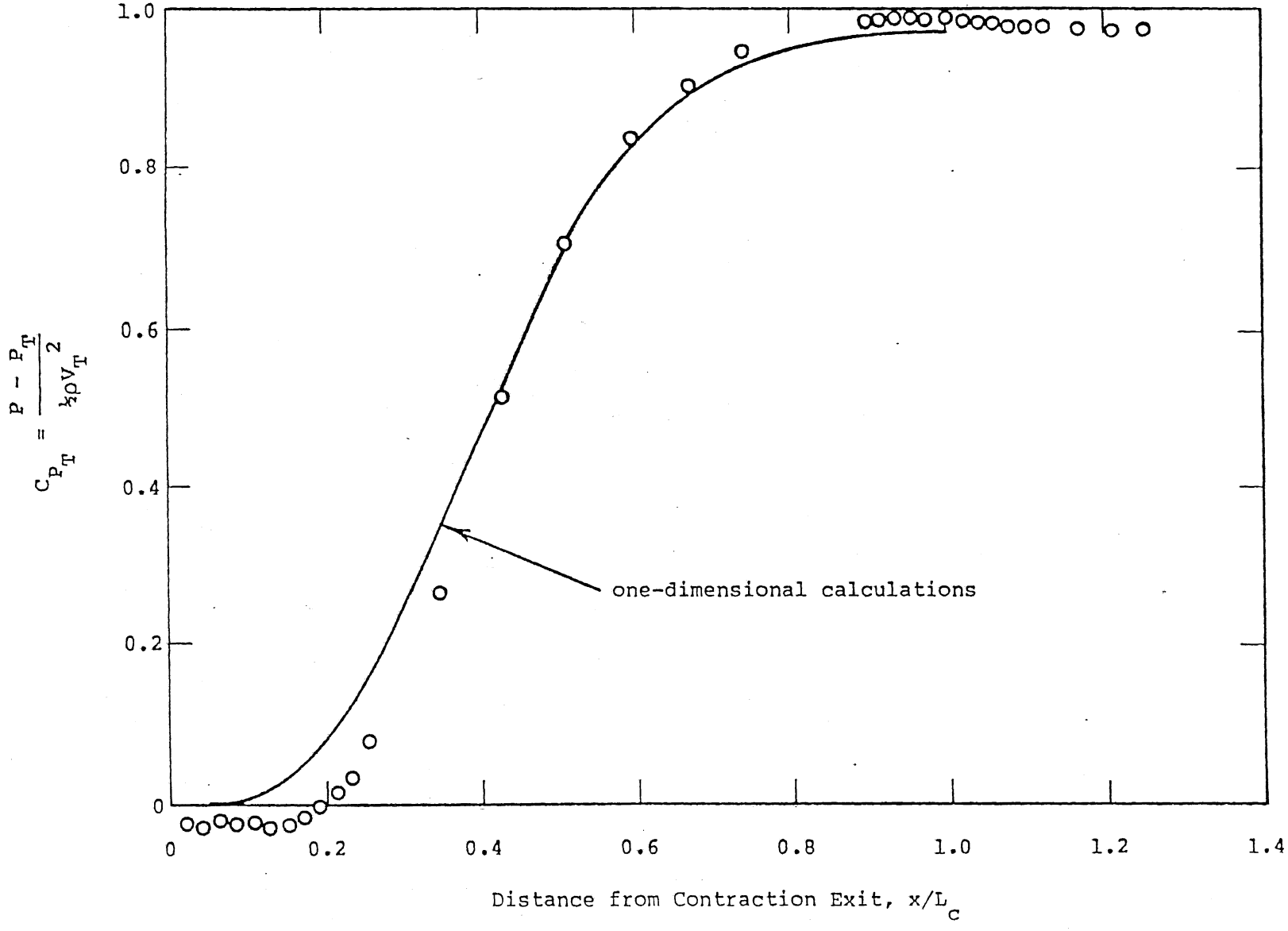

Fig. 13 - Contraction Wall Pressures, Bottom Centerline, Skewed Inlet Velocity Profil

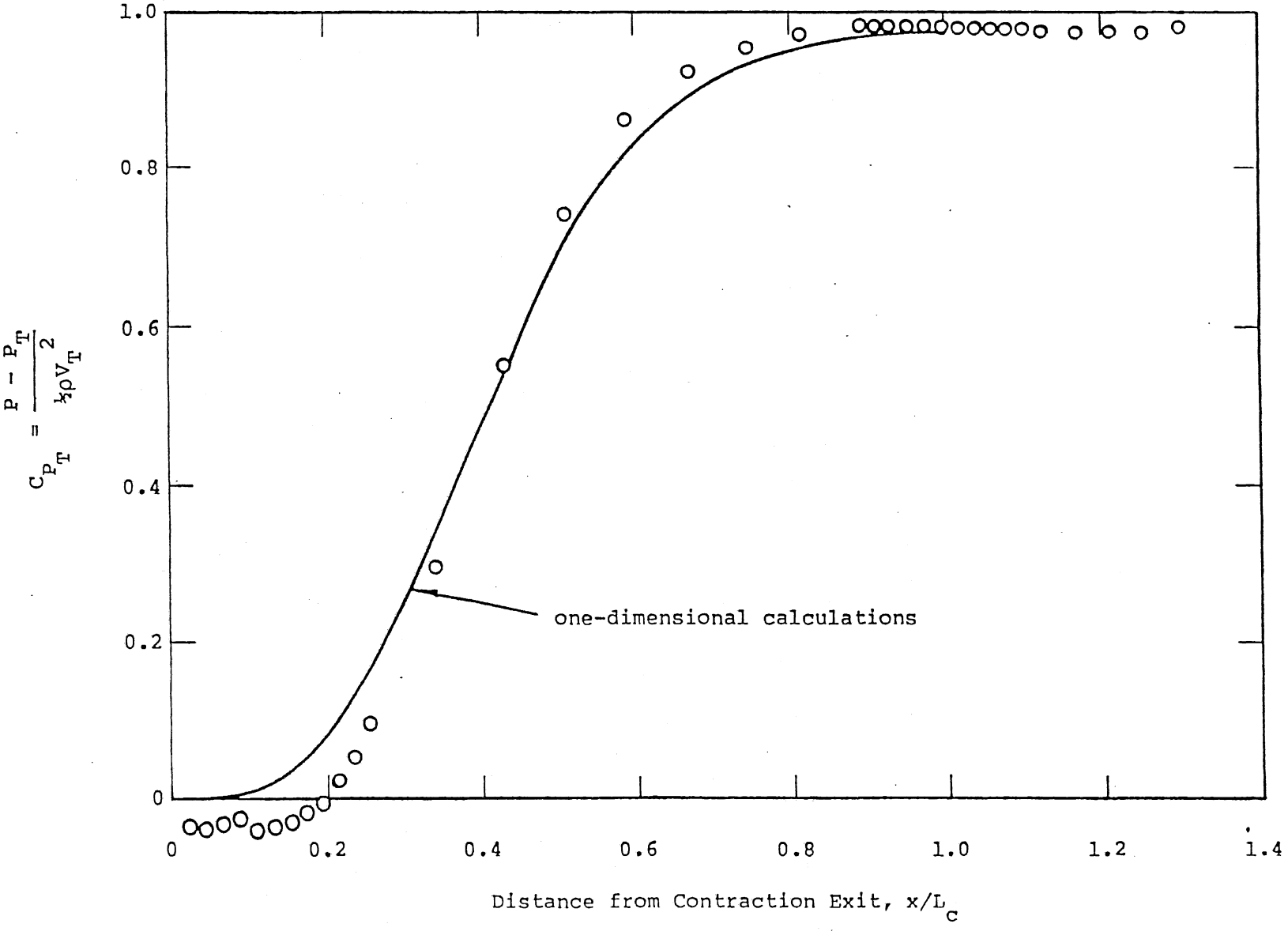

Fig. 14 - Contraction Wall Pressures, Bottom Centerline, Skewed Inlet Velocity Profile No. 2.

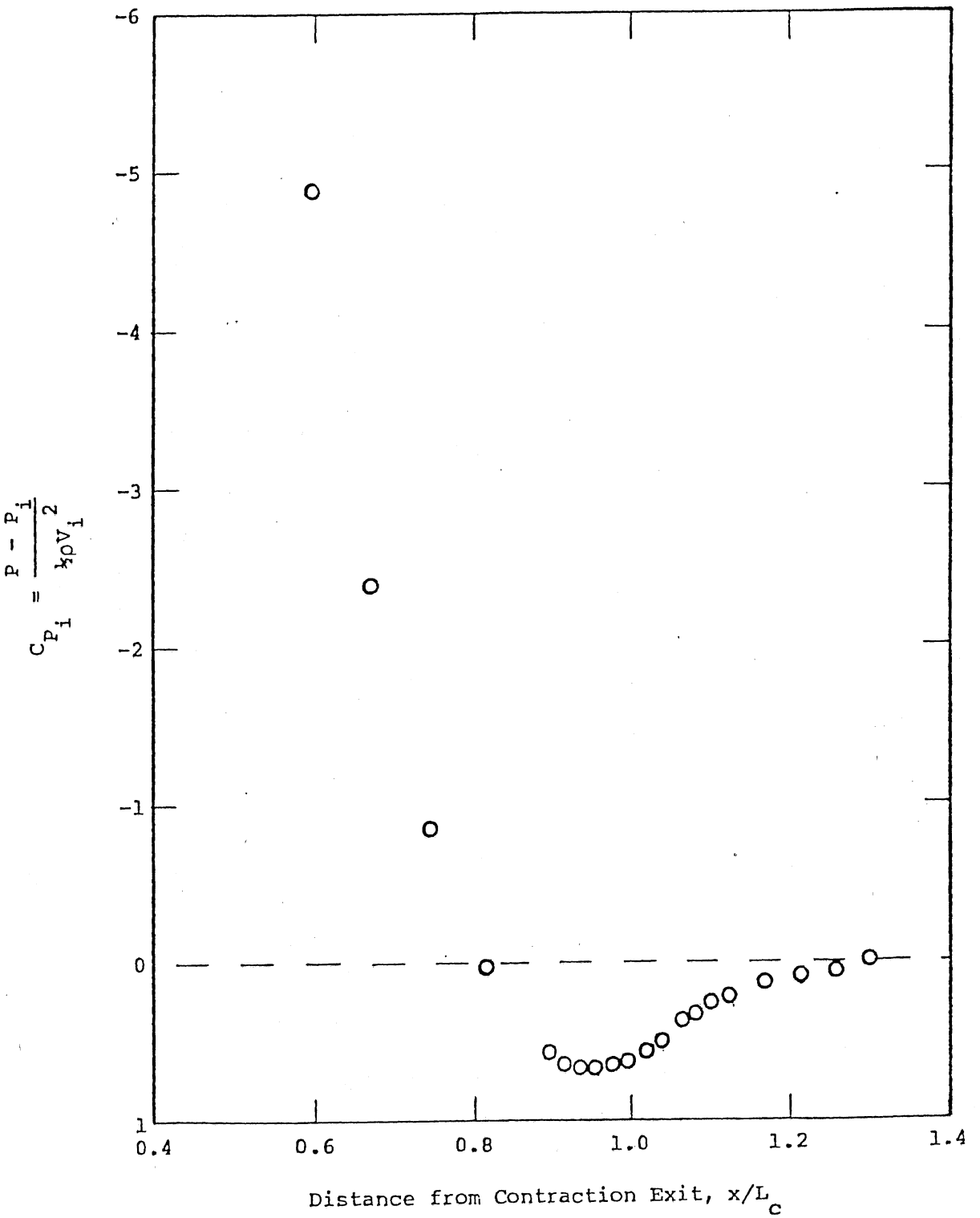

Fig. 15 – Contraction Wall Pressures, Bottom Centerline, Skewed Inlet Velocity Profile No. 1.

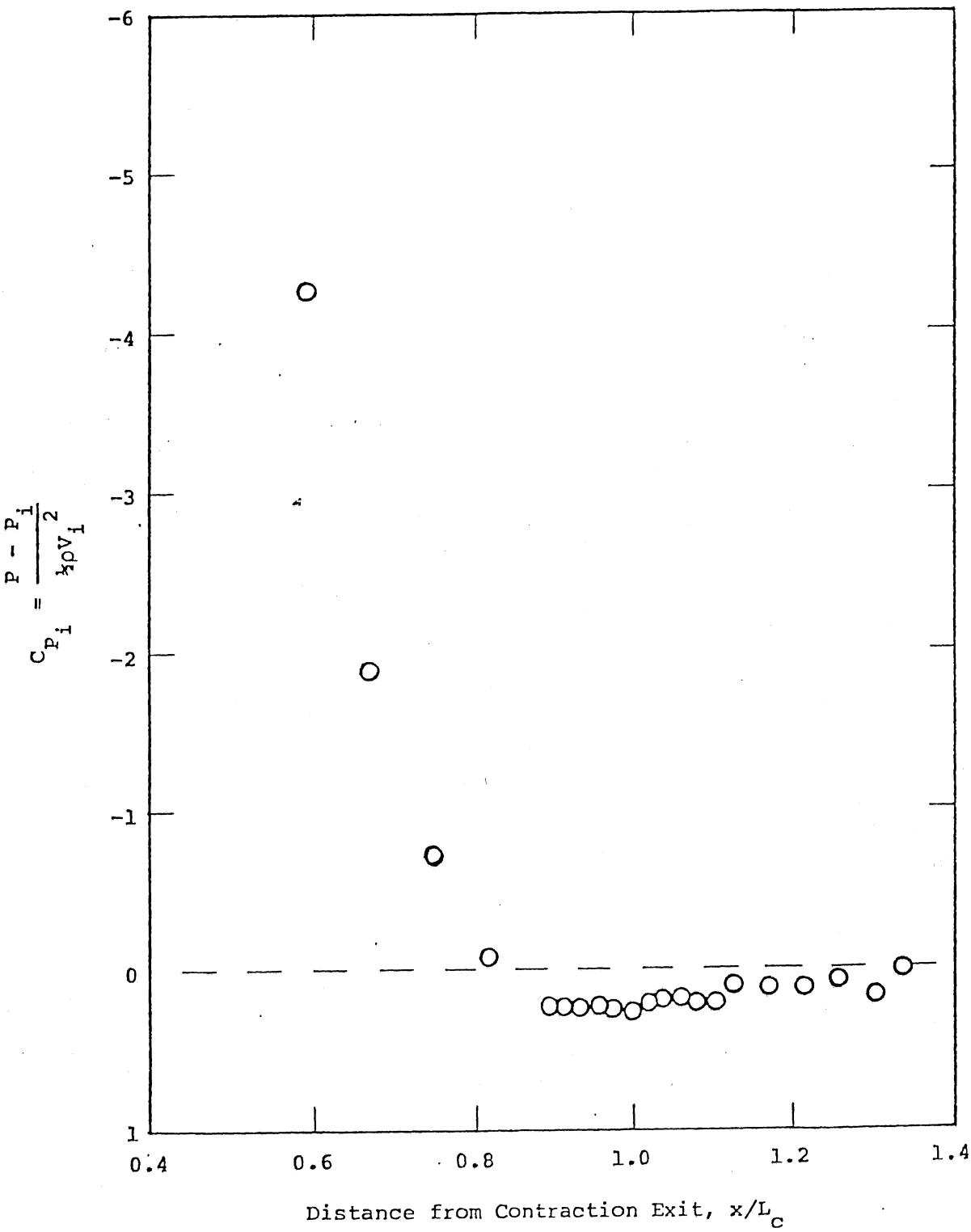

Fig. 16 - Contraction Wall Pressures, Bottom Centerline, Skewed Inlet Velocity Profile No. 2.

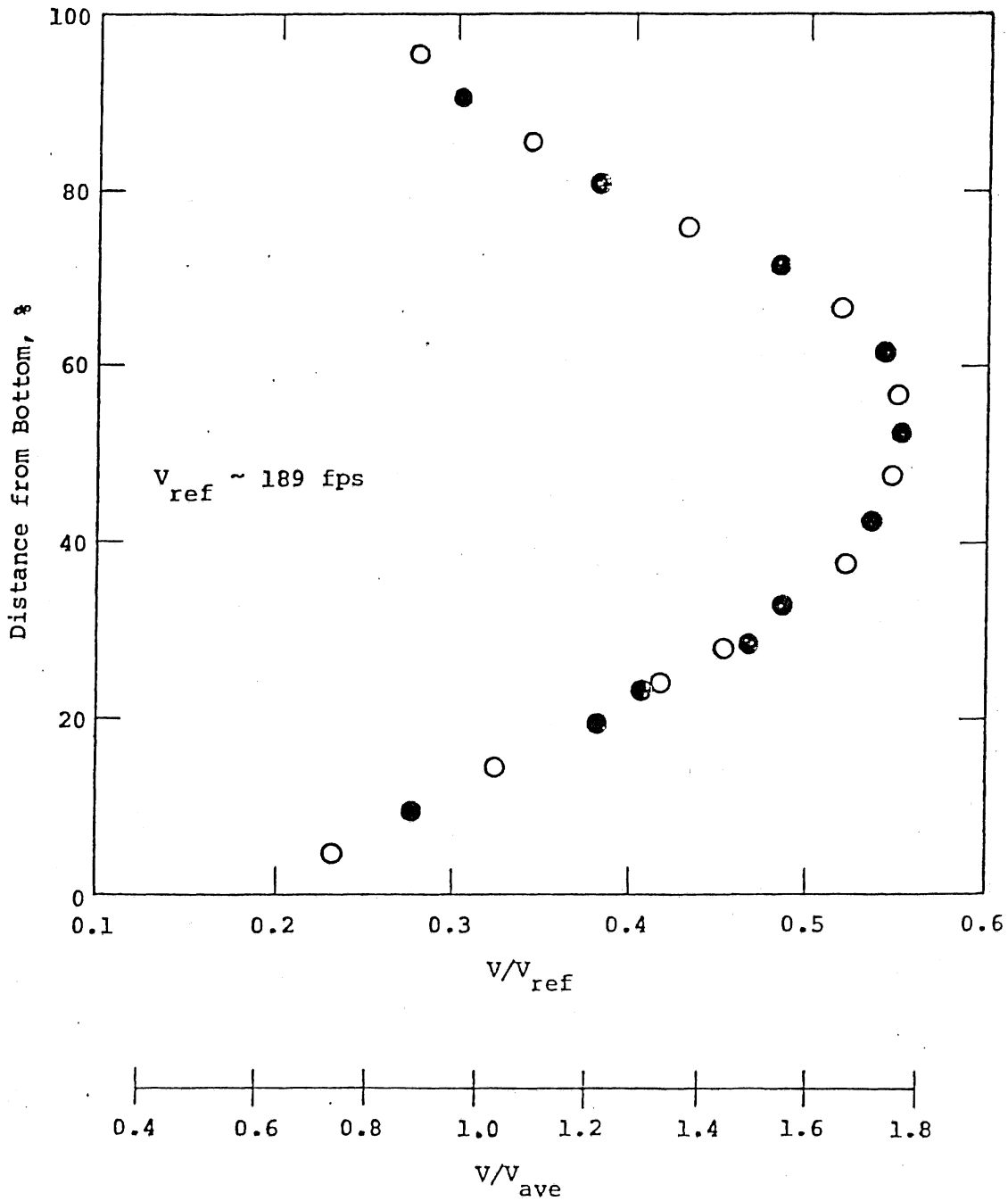

Fig. 17 - Vertical Velocity Profile at Diffuser Exit, with Fillets.

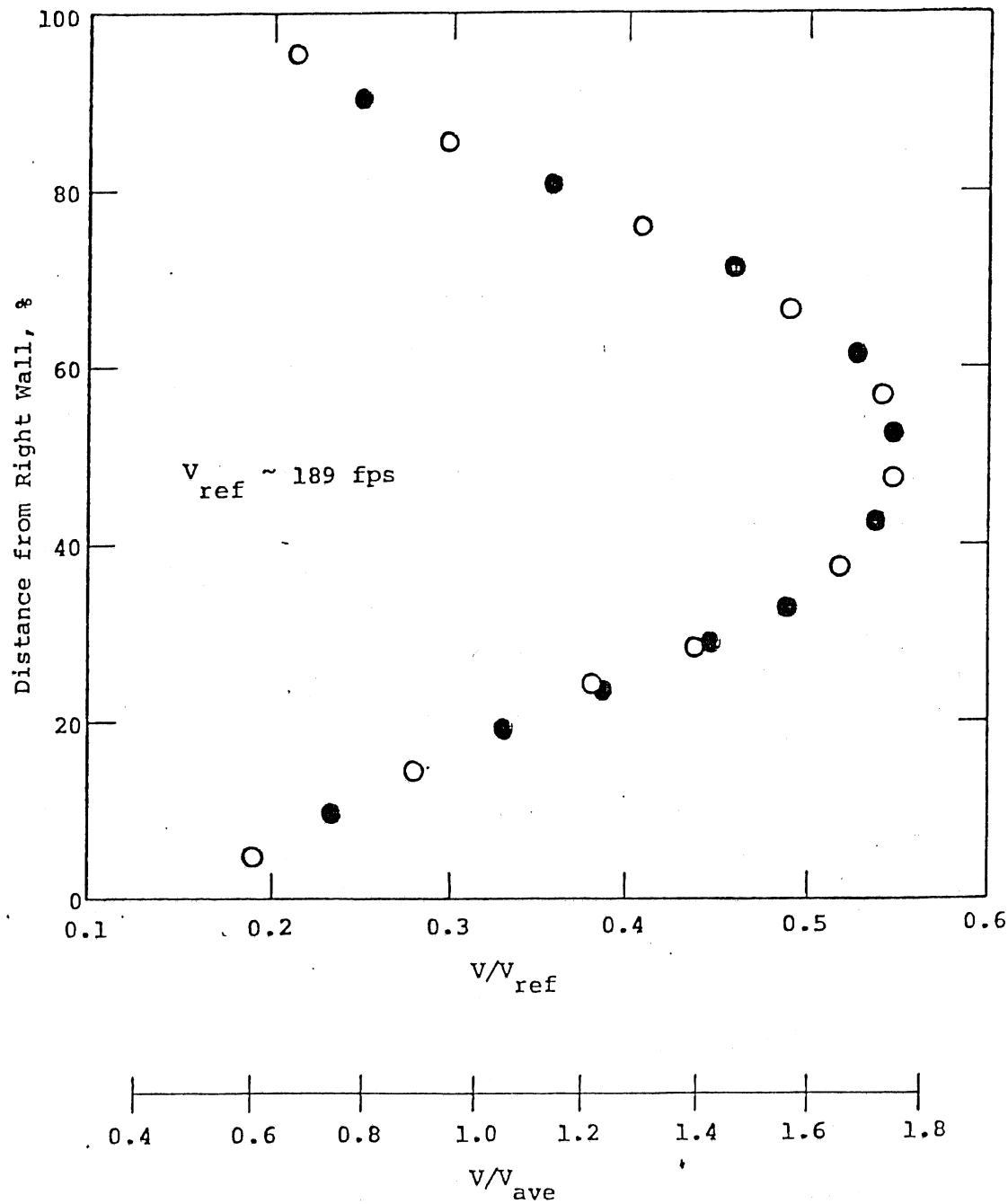

Fig. 18 - Horizontal Velocity Profile at Diffuser Exit, with Fillets.

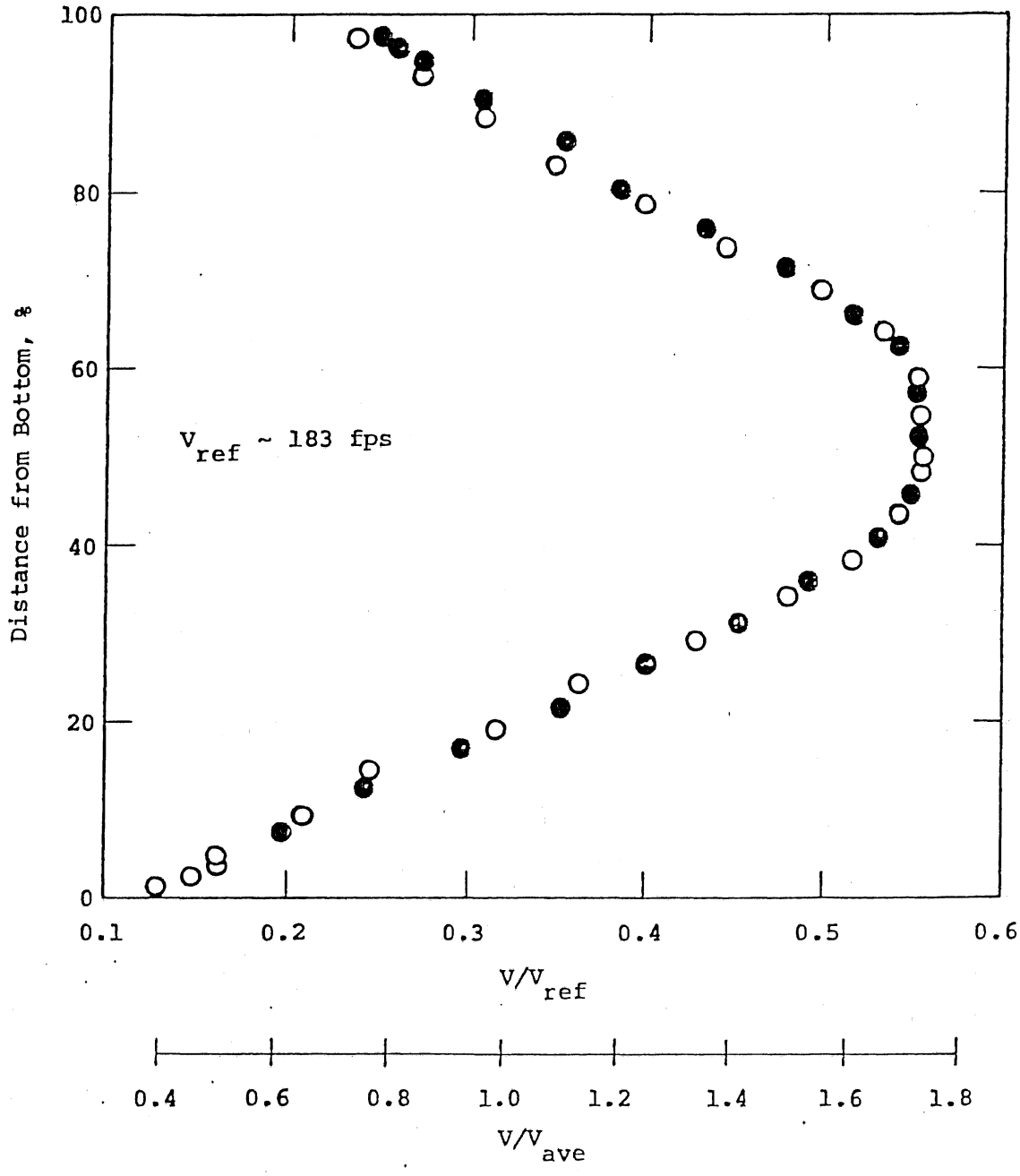

Fig. 19 - Vertical Velocity Profile at Diffuser Exit, No Fillets.

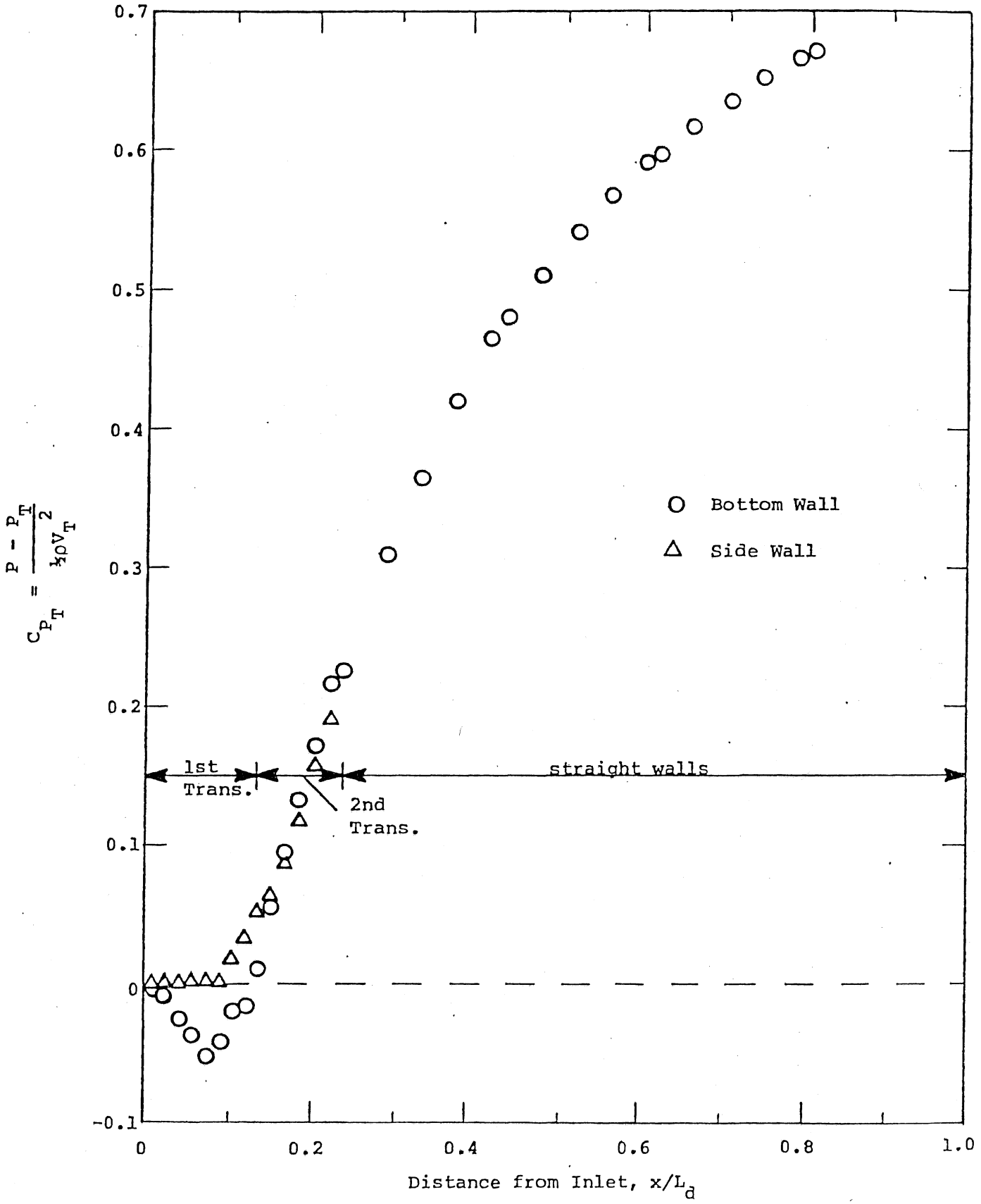

Fig. 20 - Diffuser Wall Pressures, Bottom and Side Centerlines

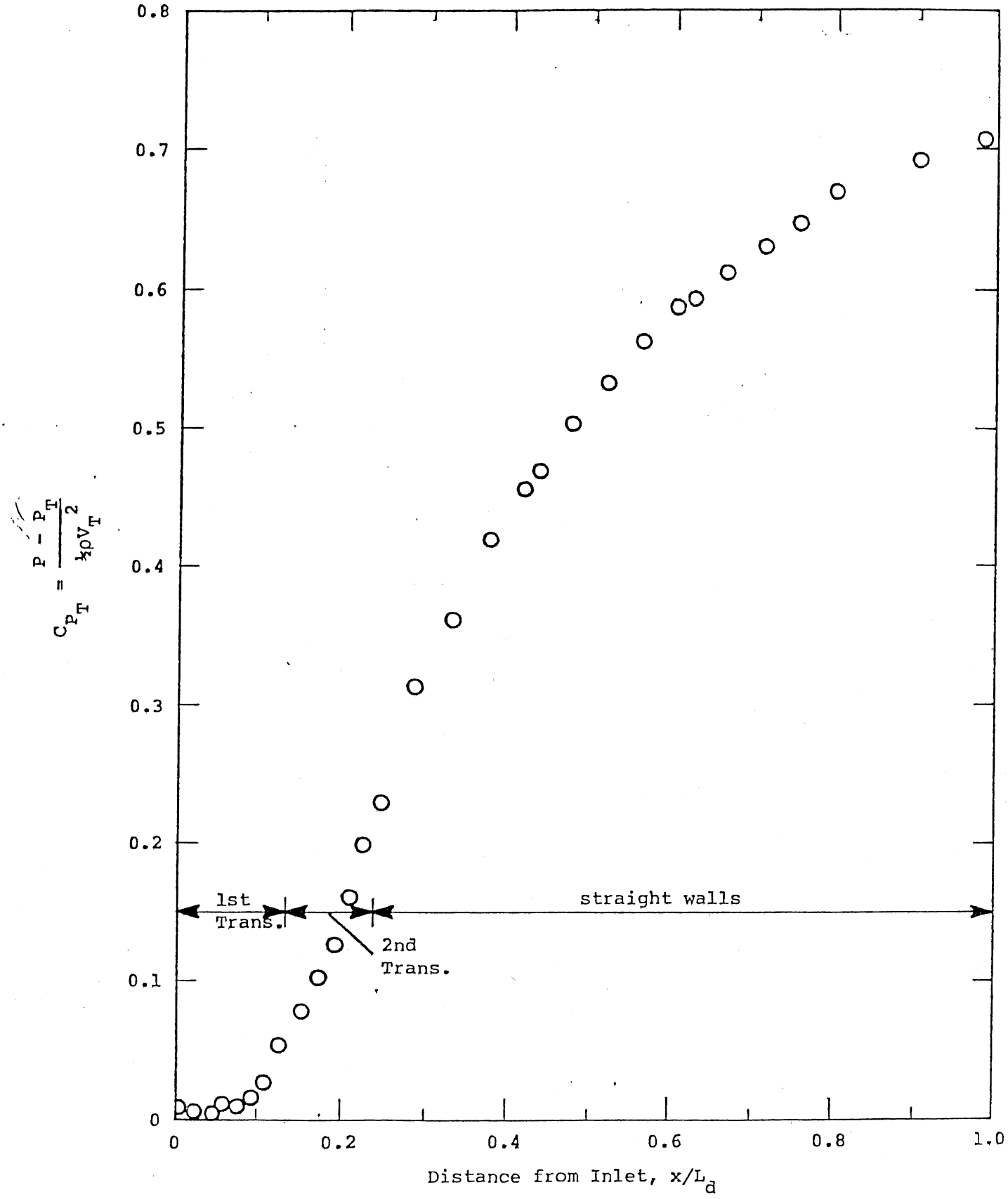

Fig. 21 - Diffuser Wall Pressures, Top Centerline.

Final Report on Phase A-2, Task B: Mathematical Modeling of the Kempf & Remmer Contraction

by

Charles C. S. Song

and

Shasradshandra Gavali

St. Anthony Falls Hydraulic Laboratory
University of Minnesota
Minneapolis, Minnesota 55414

Prepared for

SSV&K/DMJM:Joint Venture
1709 New York Ave., N.W.
Washington, D.C. 20006

July 1983

$$\frac{\partial \overline{G}}{\partial t} = -\frac{1}{V}\int_S F dS \cdot \hat{n} \qquad (3)$$

where $\overline{G}$ is the mean value of G and S is the boundary surface of the finite volume and $\hat{n}$ is a unit normal vector. Here $\overline{G}$ is also regarded as the value of G at the center of the volume. Equation 3 is a generalized conservation equation which can be solved either explicitly or implicitly.

The AR01 model is based on a two-step explicit method (also known as the predictor-corrector technique) first proposed by MacCormack [3]. This method divides the computation in two steps. The first step is to predict the present value of $\overline{G}$ using the previous (and known) value of F in Eq. 3. A new value of F is computed using the predicted value of $\overline{G}$. The second step is to compute a more accurate present value of $\overline{G}$ using the average value of F in Eq. 3. The equation of state is used to relate the density and the pressure.

This unsteady flow model is simple enough to be competitive with a steady flow model in solving a steady flow problem. Starting with an assumed initial flow condition, the model calculates the evolving flow at each successive time step, for a fixed boundary condition, until the flow ceases to vary. Because the original model was developed for the purpose of modeling large Mach number external flows, some effort was expended to make the model applicable to small Mach number internal flow problems. Some of the major developments performed at the St. Anthony Falls Hydraulic Laboratory are described below.

A. The Grid Geometry

A specific grid generating program for the K-R contraction was developed because the original program contained only a program for axially symmetric external flow. The K-R contraction is symmetric about a vertical plane so that only half of the flow needs to be modeled. The equations specified by the K-R

preliminary design were used to describe the boundary in such a way that dimensions like the approach length and the contraction length can be easily changed.

To generate the needed grid system, the flow field was first sliced into n equal thickness slabs, Δx, by n-1 vertical planes. Without the fillets at the corners, these slabs have rectangular cross sections. Fillets are assumed to remove a triangular area from each of the four corners. The height and the width of each slab is then divided into m and ℓ segments of variable lengths Δy and Δz, respectively. There are conflicting requirements for the grid size distribution. The curved boundary condition requires very small Δy and Δz near the boundary but the computer costs grow rapidly with decreasing grid size. Numerical experimentation led to the conclusion that a variable grid size distribution with a minimum size at a curved wall and a maximum size at the center of the channel with a ratio, $\Delta y_{max}/\Delta y_{min} = 2$, gave the optimum result.

B. Initial Conditions

The original program assumes that the flow is everywhere equal to the ambient flow at the initial instant. The model would then compute the subsequent changing flow at every incremental time step until a specified time is reached. If the computed results near the end of the specified time does not change much with time, then the solution is regarded as converged. This constant initial condition did not work well for the LCC model. The model would either not converge or converge to a set of incorrect values. For this reason the model was modified to accept a one-dimensional flow solution as the initial condition. This change resulted in a very significant improvement.

C. Low Mach Number Effect

There was initially some concern about the ability of the model to handle flow at low Mach number. However, it turned out that the problem was minor and was easily corrected. In fact, for the velocity computations, the model converged more rapidly for lower Mach number than for higher Mach number. The problem was with the pressure coefficient calculation which would not converge with small Mach number.

A close examination of the model revealed that the problem was a trivial one due to the definition of the pressure coefficient used in the model. The pressure coefficient used was

$$Cp = \frac{P - P_\infty}{\frac{1}{2}\rho_\infty U_\infty^2} = \frac{\frac{P}{\frac{1}{2}\rho_\infty C_\infty^2} - \frac{P_\infty}{\frac{1}{2}\rho_\infty C_\infty^2}}{M_\infty^2} \qquad (4)$$

For a very small Mach number the above equation requires the division of very small numbers by another very small number. The problem was corrected easily by using a more common expression of the incompressible flows.

Although the model could be further modified to be made more efficient for low Mach number, time did not permit further improvement.

D. Leakage

The modeling effort was confronted by a leak problem until it was largely solved near the end of the project period. There was a substantial amount of leak which appeared to decrease only linearly with the grid size while the computer costs increased as the third power of the inverse of the grid size. This would make accurate runs uneconomical.

Fortunately, after repeated efforts, an error in the program was found and corrected. The error resulted in incorrectly identifying the flat surface boundary in the boundary condition portion of the program. It was discovered after noting unrealistic v and w, distribution on the plane surfaces on which the boundary conditions used should be exact. There still remains a small (higher order) error in the curved surface boundary condition which could be removed only after further developmental effort. The model is believed to be sufficiently accurate and economical as it is.

E. Convergence Characteristics

Fortunately, with some modifications, the model converges well at small Mach number. Changes that are helpful to the speed of convergence are a) better initial conditions, b) gradual variation in grid size distribution, c) avoid dividing by Mach number, and d) more frequent smoothing operations than the original model has indicated. The number of time steps required for convergence is nearly independent of the Mach number and the number of grids. This is a rather surprising result. For the present model a total of 1200 time steps are required for an adequate convergence.

II. THE MODELING RESULTS

total of seven runs were performed using the Cray 1 computer of the
y of Minnesota. The results of these runs are presented below.

orm Inflow (Runs No. 1 and No. 1A)

ne geometry consists of an 8 m (26.25 ft) approach channel, the 11.8 m
t) contraction, and a 6.88 m (22.58 ft) test section. For Run No. 1,
ire length was divided into 27 equal $\Delta x = 0.9833$ m. The height and the
of the channel were divided into 19 and 11 variable segments,
vely; thus, the total number of grids was 5,643. The velocity at the
ce to the approach channel was assumed to be constant and parallel to the
the channel. The one-dimensional flow solution was used as the initial
on. The solution was essentially converged after 1200 time steps.
he computed (u, v) velocity distribution on the plane of symmetry
ne) is plotted in Fig. 1. In this figure the velocity vectors are
sented by line segments originating at circular symbols which represent the
ons. Similar plots of (u, v) velocity distributions over vertical
es of constant jz (the number of grids in z direction measured from the
ane) can also be made. For examples, the velocity distribution on the
al surface at the 1/4 width and that on the side wall are, respectively,
in Fig. 2 and Fig. 3. The vertical velocity profiles on the plane of
ry at the test section entrance and at the mid-test section are replotted
. 4. The corresponding data from the physical model measurement are also
in this figure for comparison. Very good agreement between the two is
ated.

face (xz-plane) is
-depth is shown
hown in Fig. 7.
ection entrance
ding
r comparison.

oss-sections were
distribution at
interesting to
ction and moving
tion is shown
. Figure 11
on, there is a
compare Fig. 11
itself at about
ry current
e centerline
a in Fig. 13.

(5)

tion. The
stream from
e measured

pressure distributions along the bottom corner and along the top corner are shown in Fig. 14.

The pressure coefficient referred to the inlet condition, C_{pi}, along the bottom centerline is plotted in Fig. 15. This pressure coefficient is defined as

$$C_{pi} = \frac{P - P_i}{\frac{1}{2}\rho V_i^2} \tag{6}$$

in which the subscript i represents the value at the inlet. This figure clearly shows the adverse pressure gradient near the beginning of the contraction. (The beginning of the contraction is at $x/L_c = 1.0$).

B. Nonuniform Flow A (Run No. 2)

This mathematical modeling run was made to simulate an experimental run in which the inflow velocity distribution was distorted by a screen. The velocity distribution along a vertical line 4 m upstream of the beginning of the contraction is shown in Fig. 16. This velocity distribution, assuming no variation in the z-direction, is used as an input to the mathematical model. Shown on the right-hand side of the same figure are the computed and the measured velocity profiles near the beginning of the test section. The mathematical model predicts about twice as much velocity variation in the test section as the physical model. However, both models indicate that the contraction is highly efficient in generating uniform velocity distribution because the inflow velocity distribution tested was unusually severe (50% distortion). As will be discussed in the next section, the difference in the velocity profile between the mathematical model and the physical model can be practically eliminated when a larger numerical viscosity is introduced in the mathematical model.

The (u, v) velocity distribution on the plane of symmetry is shown in Fig. 17. It depicts in detail how the contraction changes the nonuniform velocity into uniform velocity. The (u, w) velocity distribution on half of the top surface is shown in Fig. 18. The contraction made the fluid near the top surface to accelerate more than in the case of uniform inflow velocity distribution. The (v, w) velocity distributions at four cross sections are shown in Fig. 19 through Fig. 22.

The calculated and the measured pressure coefficient C_{pt} along the centerline on the bottom surface are compared in Fig. 23. Similar comparison for C_{pi} near the beginning of the contraction is shown in Fig. 24. Here, P_i and V_i refer to the bottom surface at the inlet 4 m upstream of the beginning of the contraction.

C. Nonuniform Flow B (Run Nos. 3 and 4)

For Run Nos. 3 and 4 the same inflow velocity profiles as shown in Fig. 25(a) were used. Notice that higher velocity is now on the top and lower velocity at the bottom. The only difference between Run Nos. 3 and 4 is in the frequency of the smoothing operations. The smoothing operation is equivalent to numerical viscosity which is required to make the mathematical modeling stable. The more frequently the smoothing operation is used the larger the equivalent numerical viscosity. For Run Nos. 1 to 3 the smoothing operation was applied after every 16 time steps which is about the minimum required for stability. For Run No. 4, this is increased to once every four time steps.

The dotted lines in Fig. 25 are the velocity profiles in the test section as computed by Run No. 3. The corresponding values calculated by Run No. 4 are shown by a solid line. This figure indicates a remarkable result that an appropriate amount of numerical viscosity is needed to accurately simulate the

case of nonuniform inflow velocity distribution. Clearly, viscosity contributes to the smoothing capability of a nozzle.

The (u, v) velocity distribution on the plane of symmetry as computed by Run No. 3 is shown in Fig. 26 and the corresponding (u, w) velocity distribution on the top surface is shown in Fig. 27. Similar plots for Run No. 4 are omitted because the differences would be insignificant because of the scale used.

The (v, w) velocity profiles as computed by Run No. 3 are shown in Fig. 28 through Fig. 31. The vortex generated by the viscous effect is clearly visible in Fig. 31. Because this figure represents only a half of the total channel cross section, there would be two counter rotating vortices. Similar (v, w) velocity profiles as computed by Run N4 are shown in Fig. 32 through Fig. 35. It is interesting to note that the increased numerical viscosity created four vortices, rather than two, a short distance downstream of the end of the contraction as clearly visible in Fig. 35.

The pressure coefficients, C_{pt} , along the centerline at the bottom surface, as computed by the mathematical modeling Run Nos. 3 and 4 are compared with the measured values in Fig. 36. The pressure coefficients based on the inlet condition, C_{pi} , are shown in Fig. 37. Again the agreement between the mathematical model and the physical model is quite good.

It is interesting to compare the adverse pressure distribution at the bottom surface as computed by Run Nos. 1 through 3 as shown in Figs. 15, 24 and 37. Greatest adverse pressure gradient is shown in Fig. 24 and the least adverse pressure gradient is shown in Fig. 37. A possible explanation is offered below. The contraction tends to produce uniform flow downstream by diverting the flow towards the top centerline. When the inlet velocity at the bottom is greater than that at the top, there will be more flow diverted to the

centerline and less acceleration along the curved bottom. Less acceleration or more deceleration means more adverse pressure gradient.

D. Other Runs (Run Nos. 5, 6, and 7)

Run No. 1 and the corresponding physical model had an 8 meter approach channel instead of the 4 meter approach channel specified in the K-R preliminary design. To study the effect of the approach channel length, Run No. 5 was performed. This run is identical to Run No. 1 except that the approach channel was shortened to 4 m. The resulting velocity and pressure distributions were almost indistinguishable from those of Run No. 1. The (u, v) velocity distribution on the coefficient, C_{pi}, along the centerline on the bottom surface is shown in Fig. 39 using dotted lines.

Run No. 6 is identical to Run No. 5 except that the contraction length L_c was increased by 2 meters. The coefficients used by K-R representing the bottom surface and the side wall were modified to reflect the increased L_c. The resulting pressure coefficient C_{pi} along the centerline on the bottom surface is plotted in Fig. 39 using a solid line. By lengthening the contraction the pressure gradient is significantly reduced because the maximum value of C_{pi} is also reduced. More about the effect of modified contraction will be given under Task C.

Run No. 7 is a repeat of Run No. 3 except the the fillet was introduced in the new run. The introduction of fillet did not seem to change the result significantly except that the numerical errors might have increased slightly.

III. DISCUSSIONS AND RECOMMENDATIONS

The AR01 mathematical model has been successfully adapted to the contraction and the test section of the LCC preliminary design shape. The model is quite efficient and can accurately simulate small Mach number steady as well as unsteady flows. The cost of one run using 5,643 grids is about $80 and will increase linearly with the number of grids. For all cases that comparison was possible, excellent agreement between mathematical modeling results and the experimental data was obtained.

By and large the K-R contraction is quite efficient in generating uniform velocity distribution at the test section provided that the velocity distribution at the inlet is fairly uniform. Significant amounts of adverse pressure gradients exist on the bottom surface in the vicinity of the beginning of the contraction. The greatest amount of adverse pressure gradient occurs along the corner of the bottom surface. The adverse pressure gradient worsens as the inflow velocity profile skews towards the bottom so that more flow has to be diverted upward by the contraction. This raises the possibility of flow separation under some unfavorable conditions. The adverse pressure distribution can be significantly reduced by lengthening the contraction length of the K-R design. However, a more efficient profile can be found by iteration using the mathematical model.

The nonsymmetrical contraction in the vertical direction may also produce small amounts of (v, w) velocity components in the test section. The cross flow is towards the top centerline in the contraction but reverses its direction in the test section. This meandering flow is combined with a twin vortex to form a

complex velocity distribution in the test section when relatively small numerical viscosity is used. For a larger numerical viscosity there may be four vortices generated at the test section.

So far the model was tested only for steady undirectional inflow velocity distribution. In the real case the inflow velocity may contain y and z velocity components due to the elbows and circulations generated by the pump. There may also be some unsteadiness in the inflow velocity distribution. Thus, there is more to the nonuniformity of velocity distribution than the uniformity of u alone. This mathematical model is capable of simulating vortices and flow unsteadiness which may be valuable in more completely defining the quality of the contraction and the test section. Therefore, it is suggested that the quality of the contraction and the test section be further evaluated in terms of its sensitivity to vortices and velocity fluctuations.

The physical model will not be completely dynamically similar with the prototype. Both Reynolds number and Mach number distortions exist. As the present mathematical modeling has suggested, as far as the secondary current and vortices are concerned, Reynolds number distortion may be important. On the other hand, Mach number distortion is likely to affect the response of LCC to unsteady flows either hydrodynamically or hydroelastically generated. By adopting AR02 which contains boundary layer computation to low Mach number application, the quality of the entire upper leg of the channel, including the diffuser, could be evaluated. This evaluation can include vortices, flow separation, flow unsteadiness, etc.

With considerable effort, the model could also be generalized to include the free-surface capability.

IV. REFERENCES

1. Jacocks, J. L. and Kneibe, K. R., "Computation of Three-Dimensional Time-Dependent Flow Using the Euler Equation," Arnold Engineering Development Center, TR-80-49, July, 1981.

2. Koenig, K., "Numerical Solution of the Three-Dimensional Unsteady Euler Equation," Final report, USAF-SCEEE, Summer Faculty Research Program, Aug., 1982.

3. MacCormack, R. W., "The Effect of Viscosity in Hypervelocity Impact Cratering," AIAA, Paper No. 69-354, May, 1969.

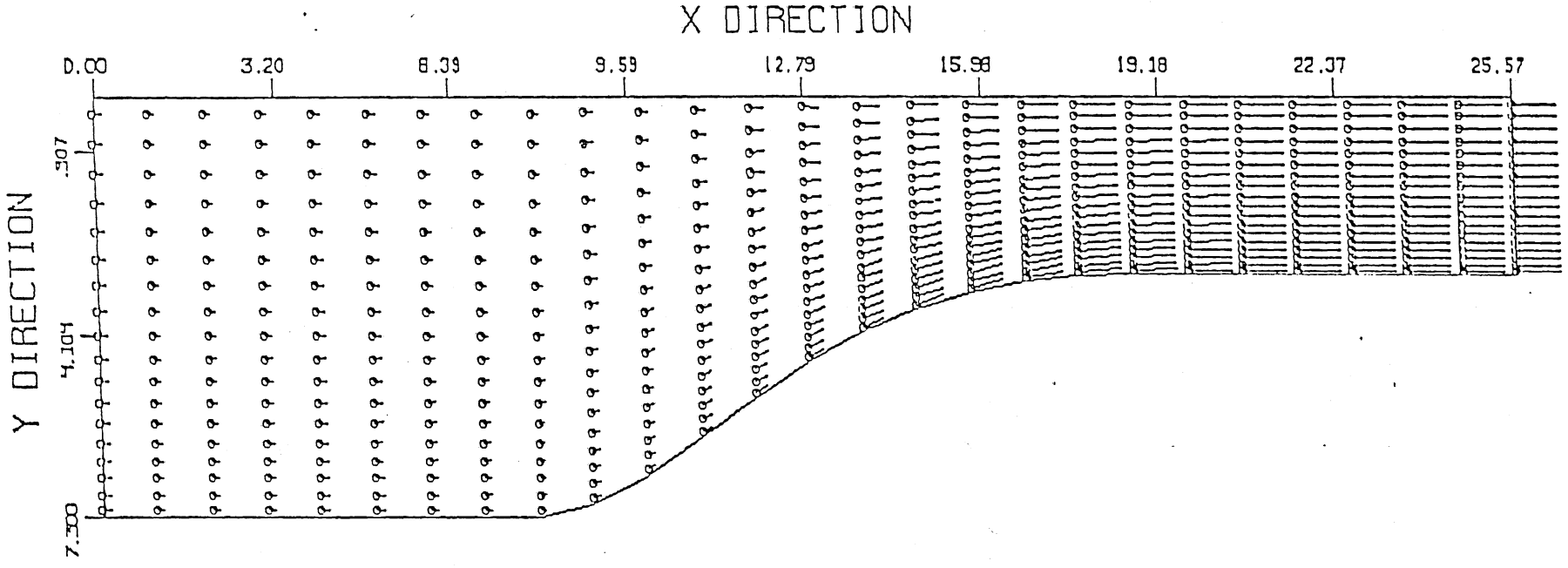

Fig. 1. (u,v) distribution on the plane of symmetry, uniform entrance velocity (Run No. 1).

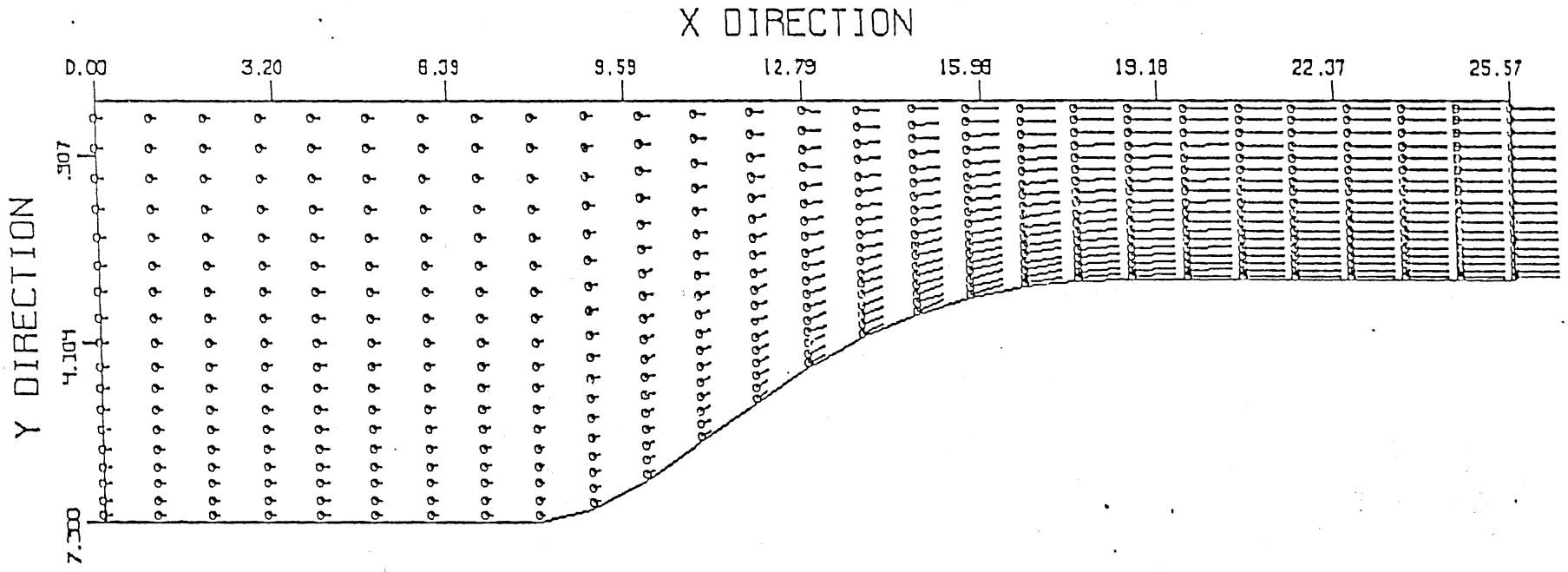

Fig. 2. (u,v) distribution on the vertical surface at ½ width, uniform entrance velocity (Run No. 2).

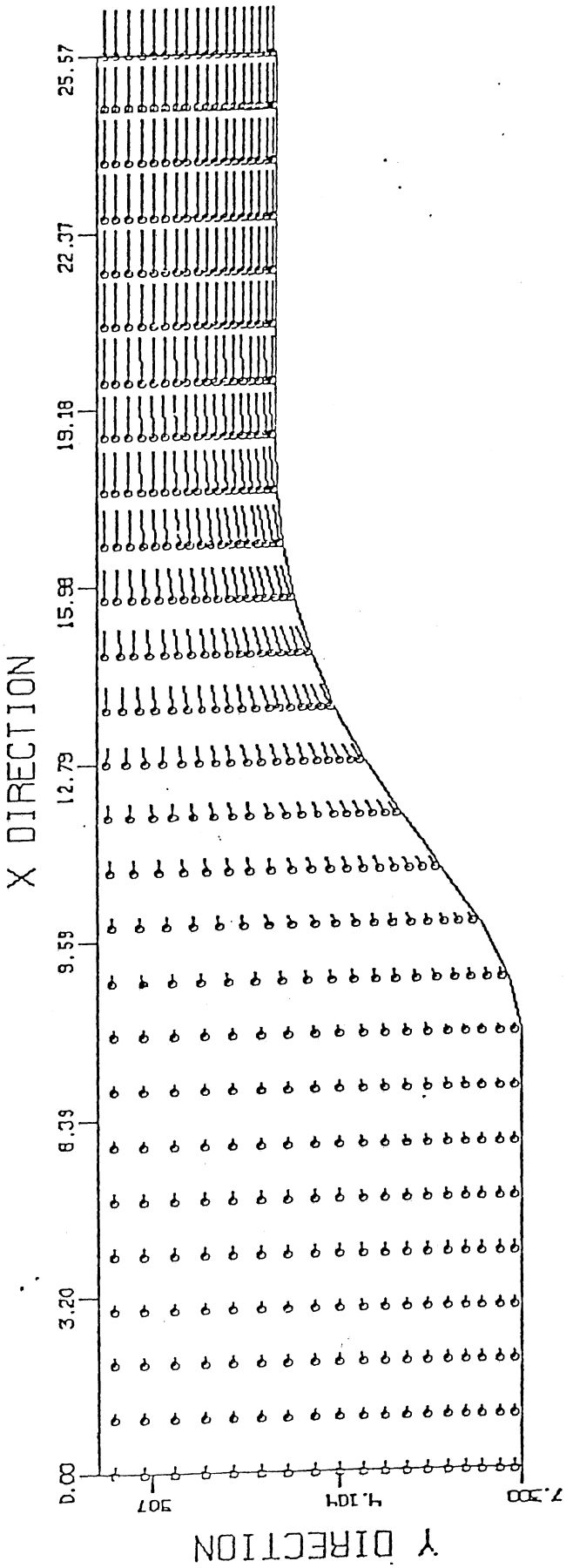

Fig. 3. (u,v) distribution on the side wall, uniform entrance velocity (Run No. 1).

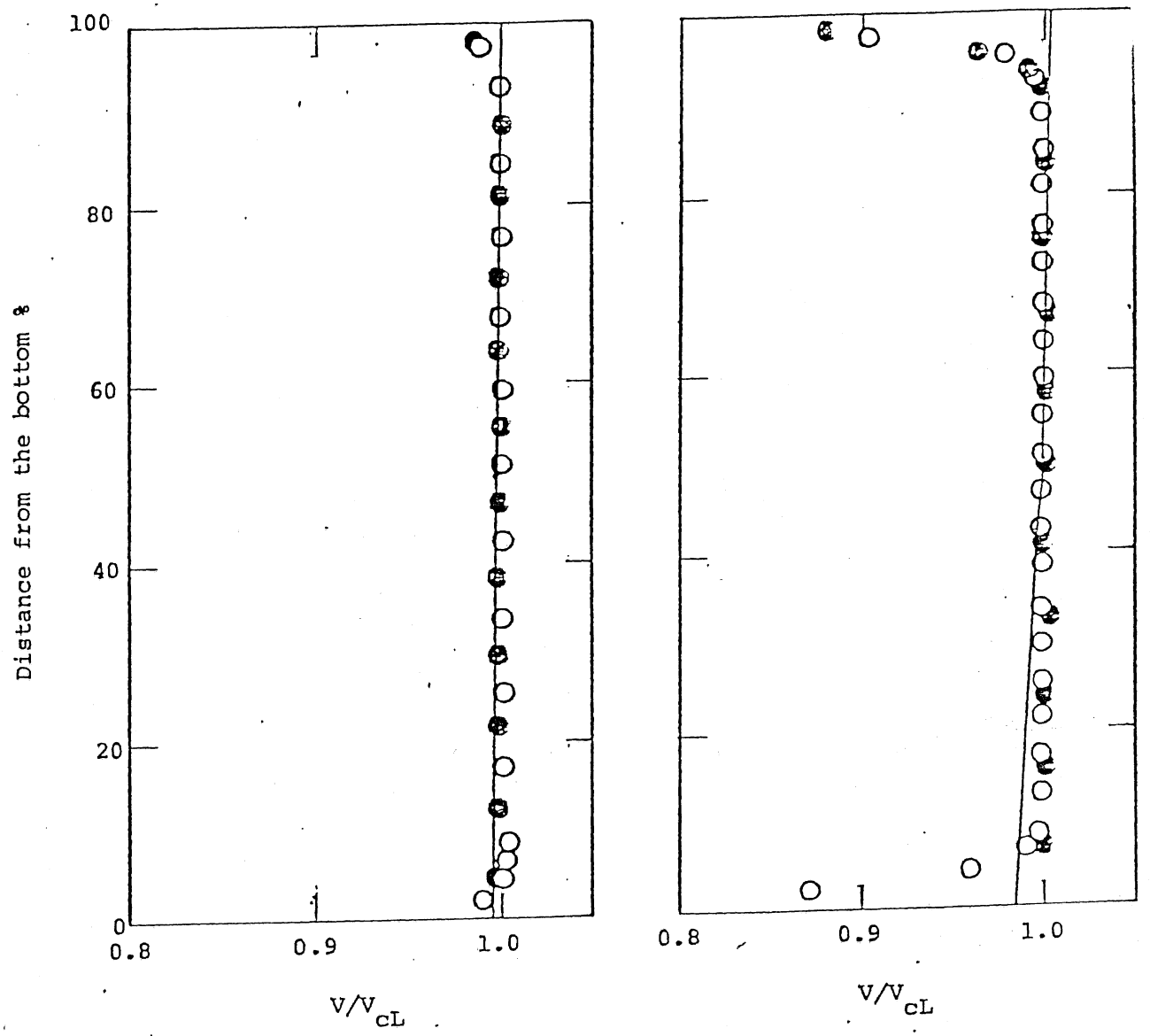

Fig. 4. Vertical velocity profiles, comparison between mathematical model and physical model (Run No. 1).

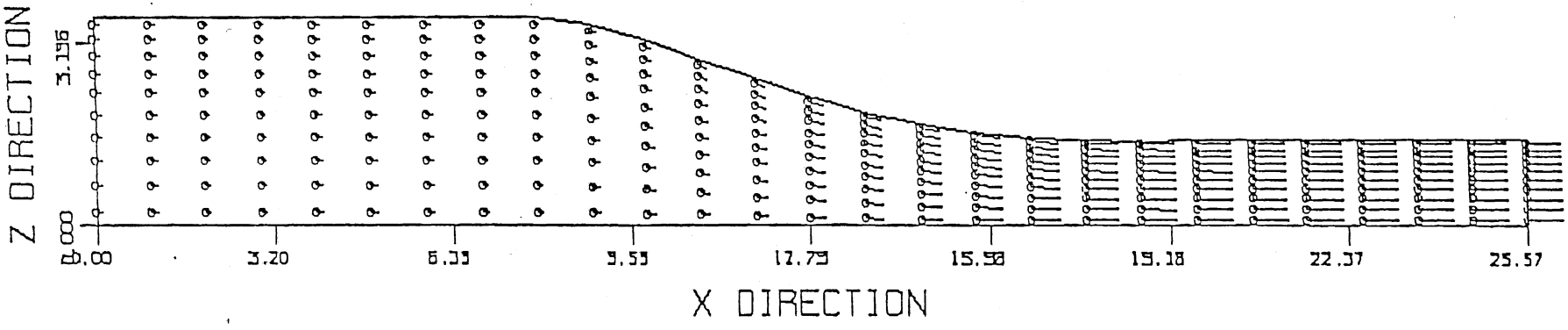

Fig. 5. (u,w) distribution on half of the top surface (Run No. 1).

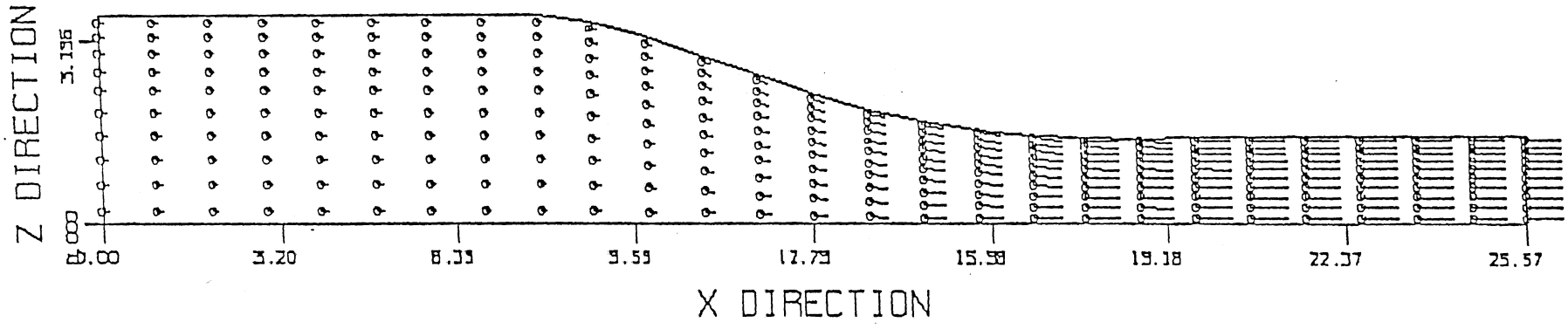

Fig. 6. (u,w) distribution on the surface at mid depth (Run No. 1).

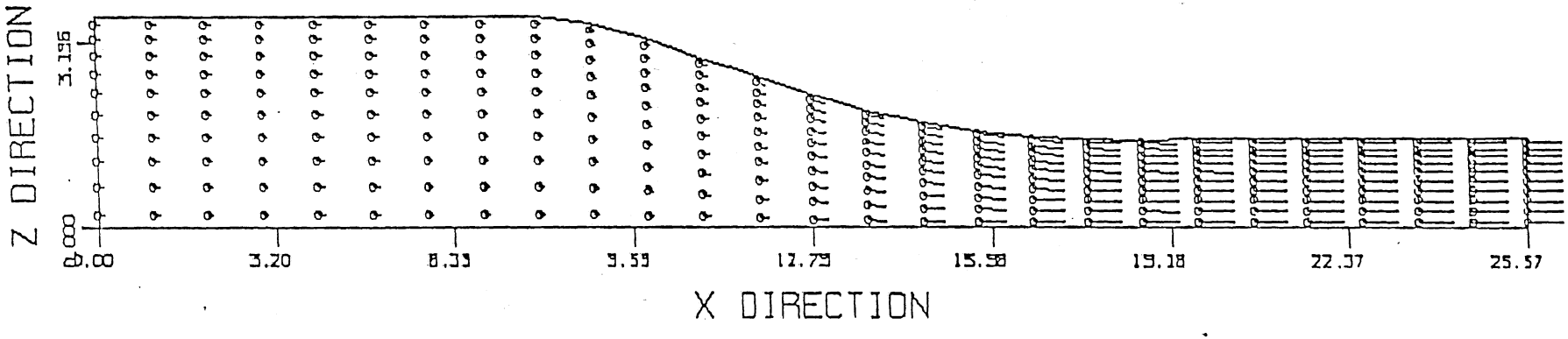

Fig. 7. (u,w) distribution on the bottom surface (Run No. 1).

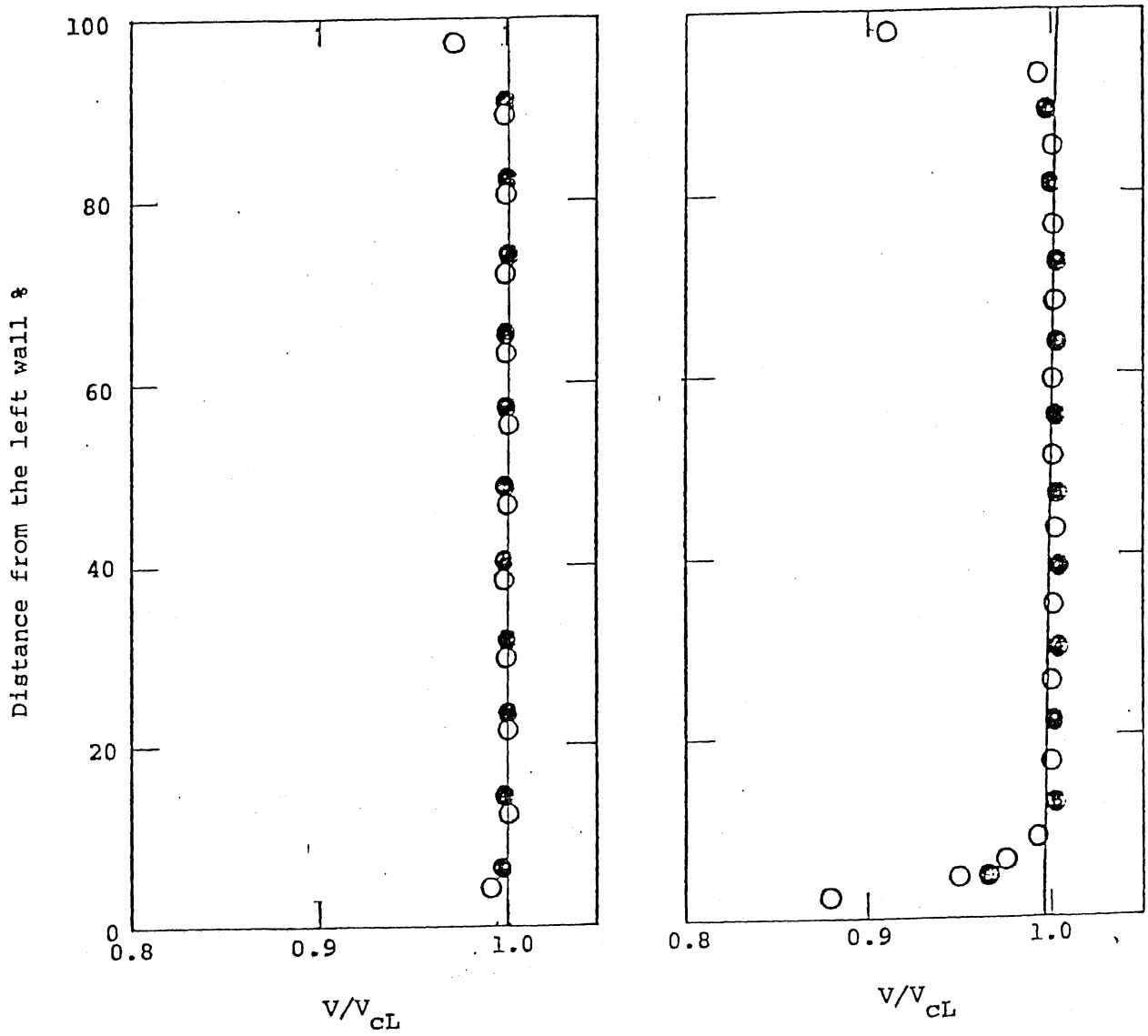

Fig. 8. Horizontal velocity profiles, comparison between mathematical model and physical model (Run No. 1).

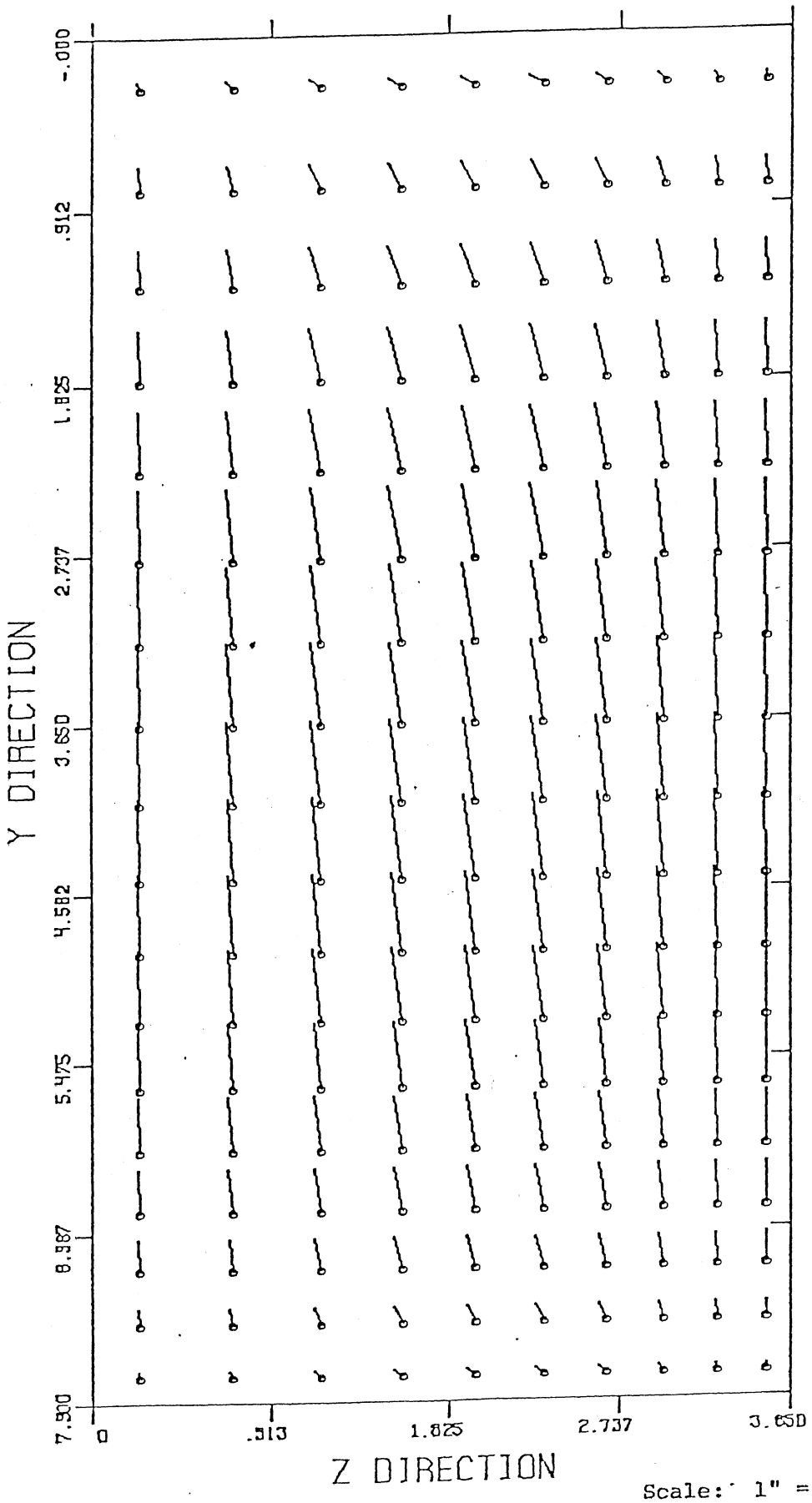

Fig. 9. (v,w) distribution on the cross section about 1.5 m upstream of the beginning of the contraction (Run No. 1)

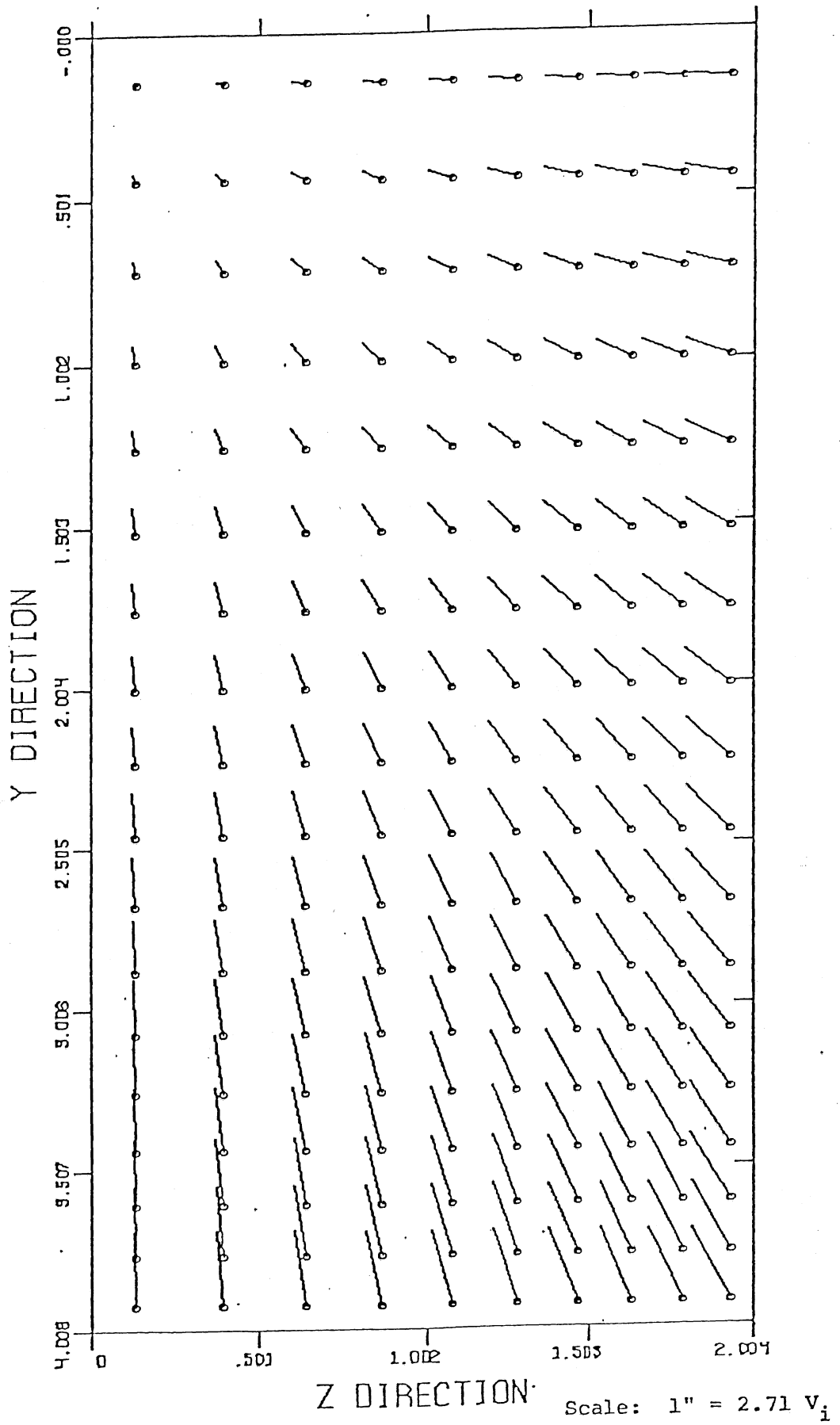

Fig. 10. (v,w) distribution on the cross section at the middle of the contraction (Run No. 1).

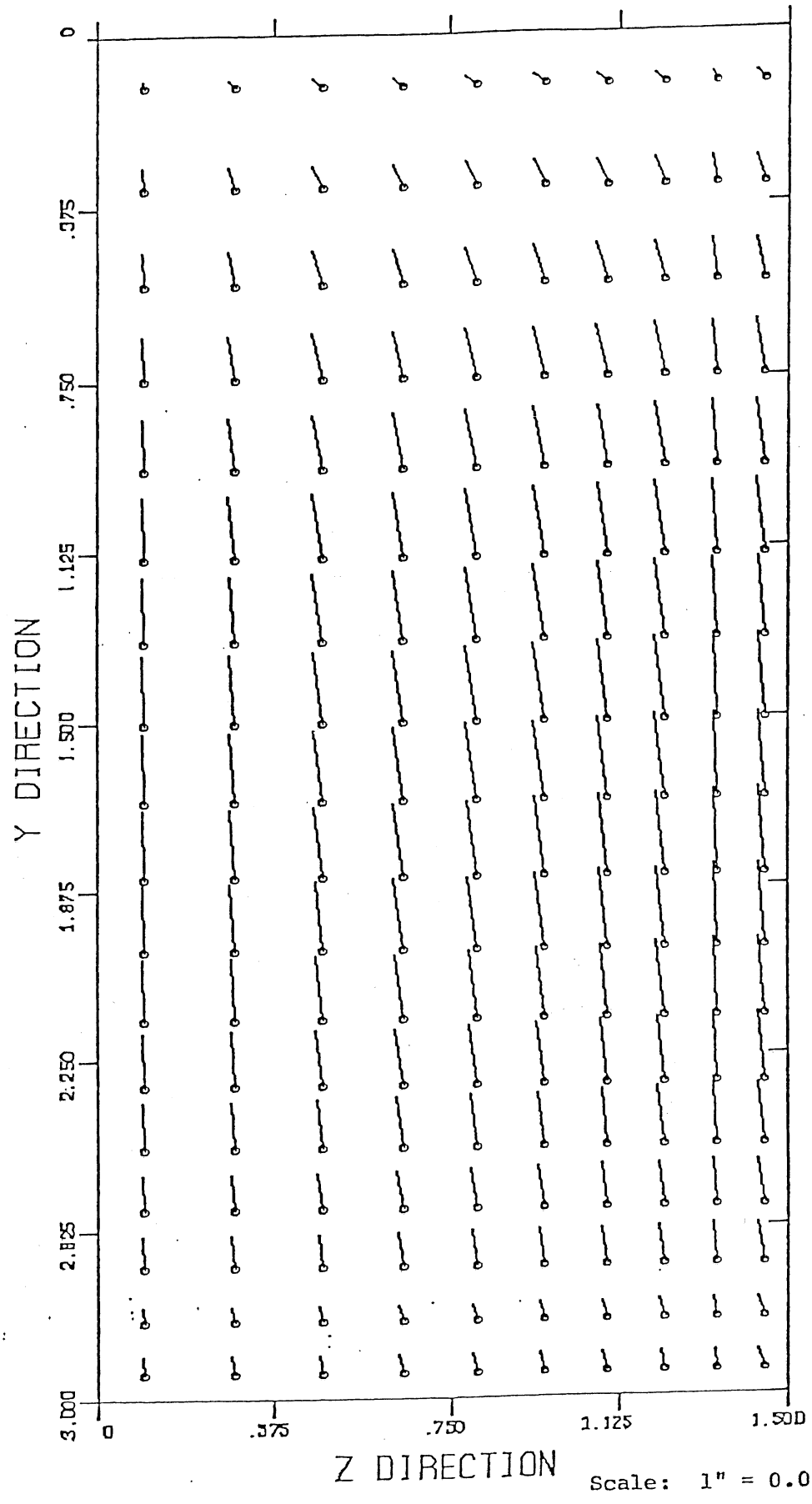

Fig. 11. (v,w) distribution on the cross section at about 0.5 m downstream of the end of the contraction (Run No. 1).

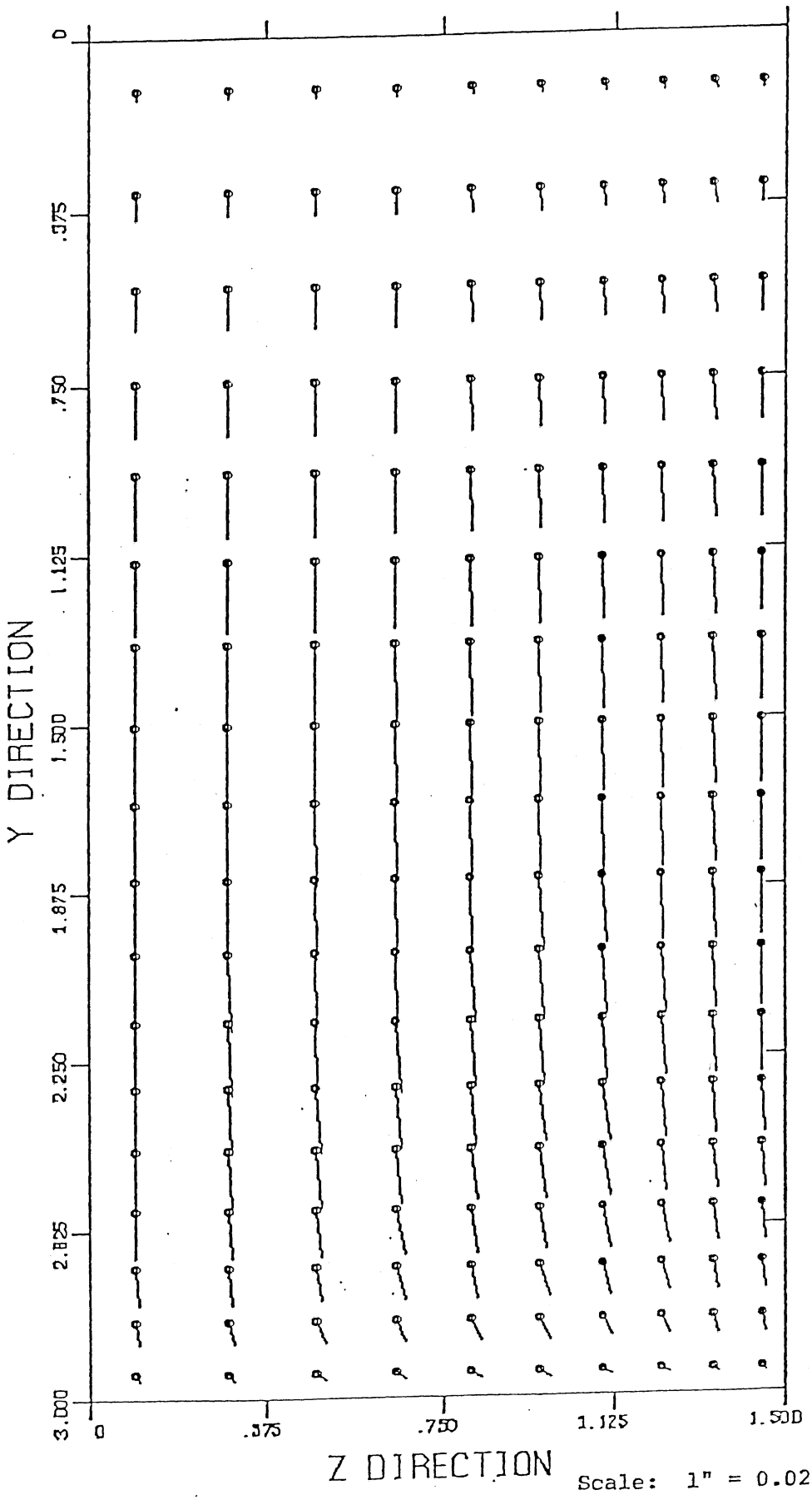

Fig. 12. (v,w) distribution on the cross section at about 2.5 m downstream of the end of the contraction (Run No. 1).

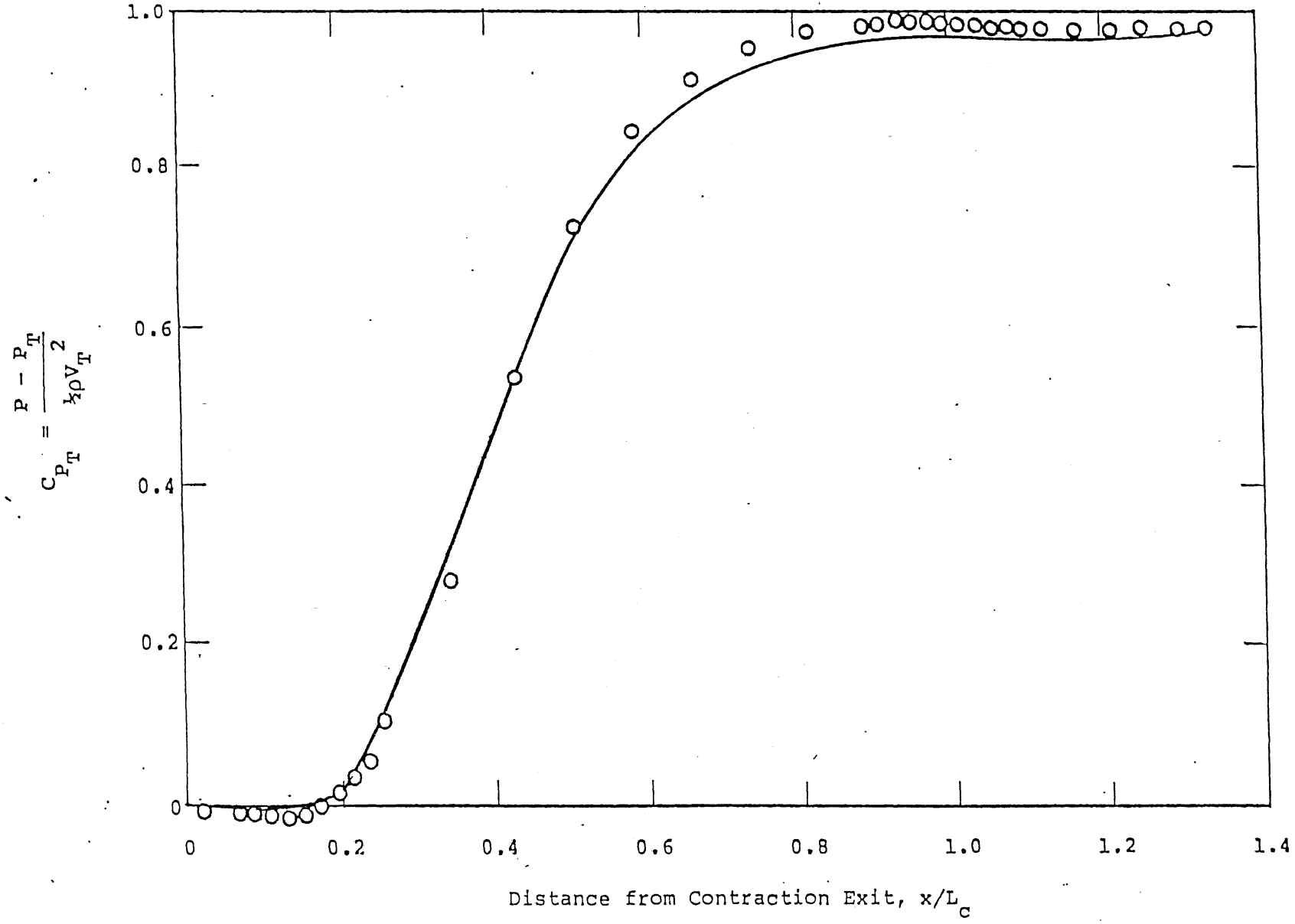

Fig. 13. Pressure coefficient along the centerline of the bottom surface (Run No. 1).

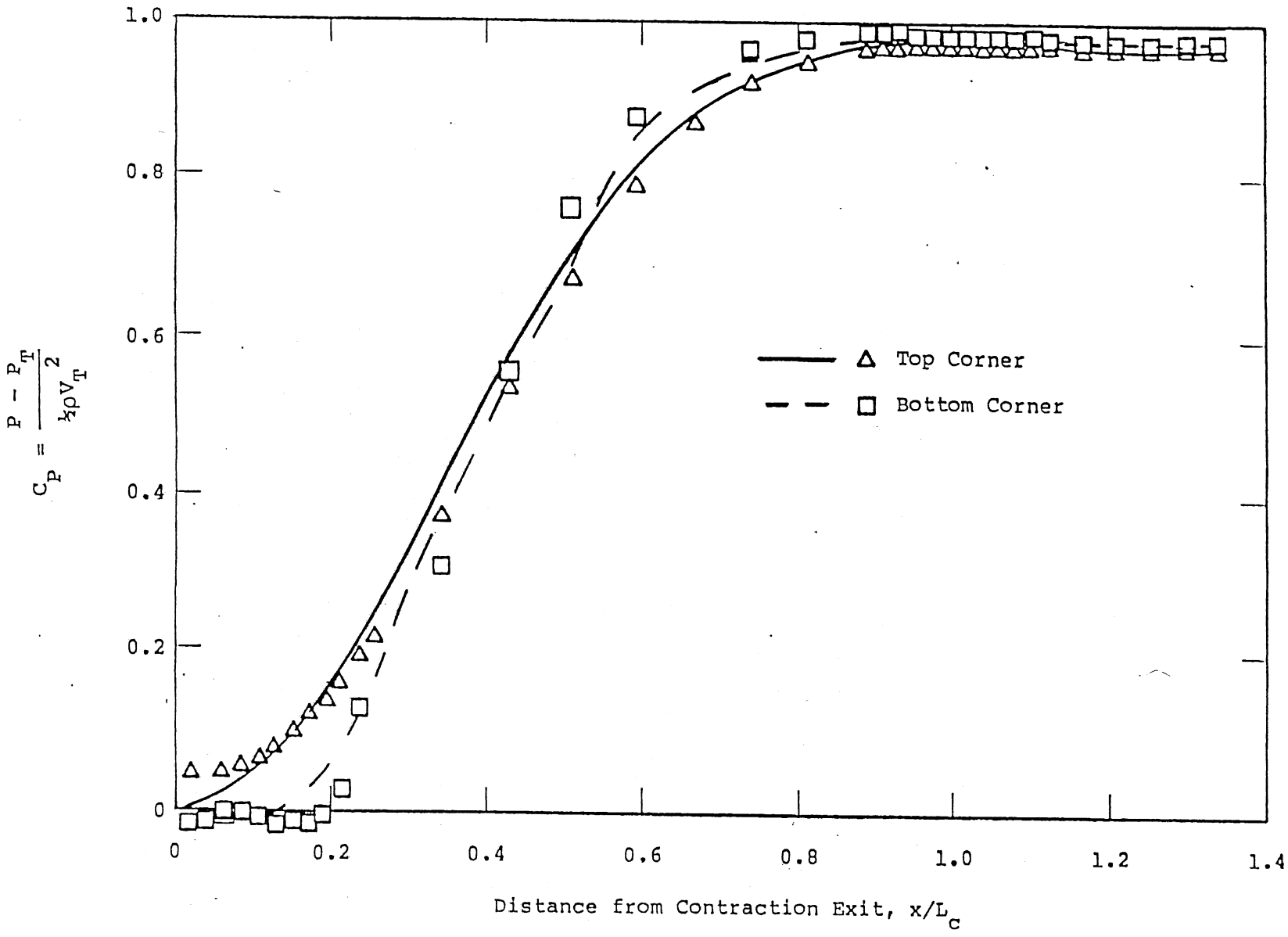

Fig. 14. Pressure coefficients along the bottom corner and top corner (Run No. 1).

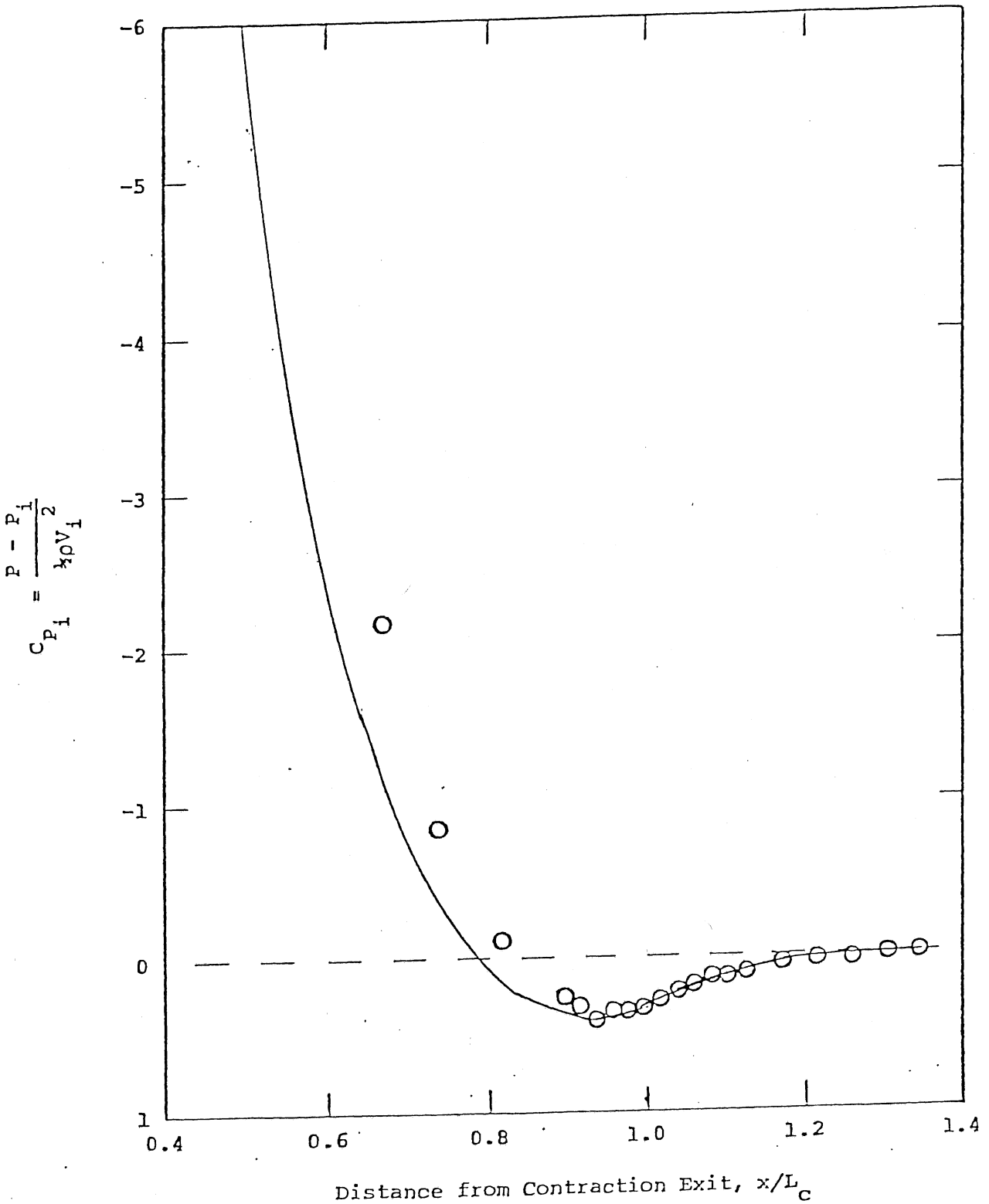

Fig. 15. Pressure coefficient along the center line of the bottom surface near the beginning of the contraction (Run No. 1).

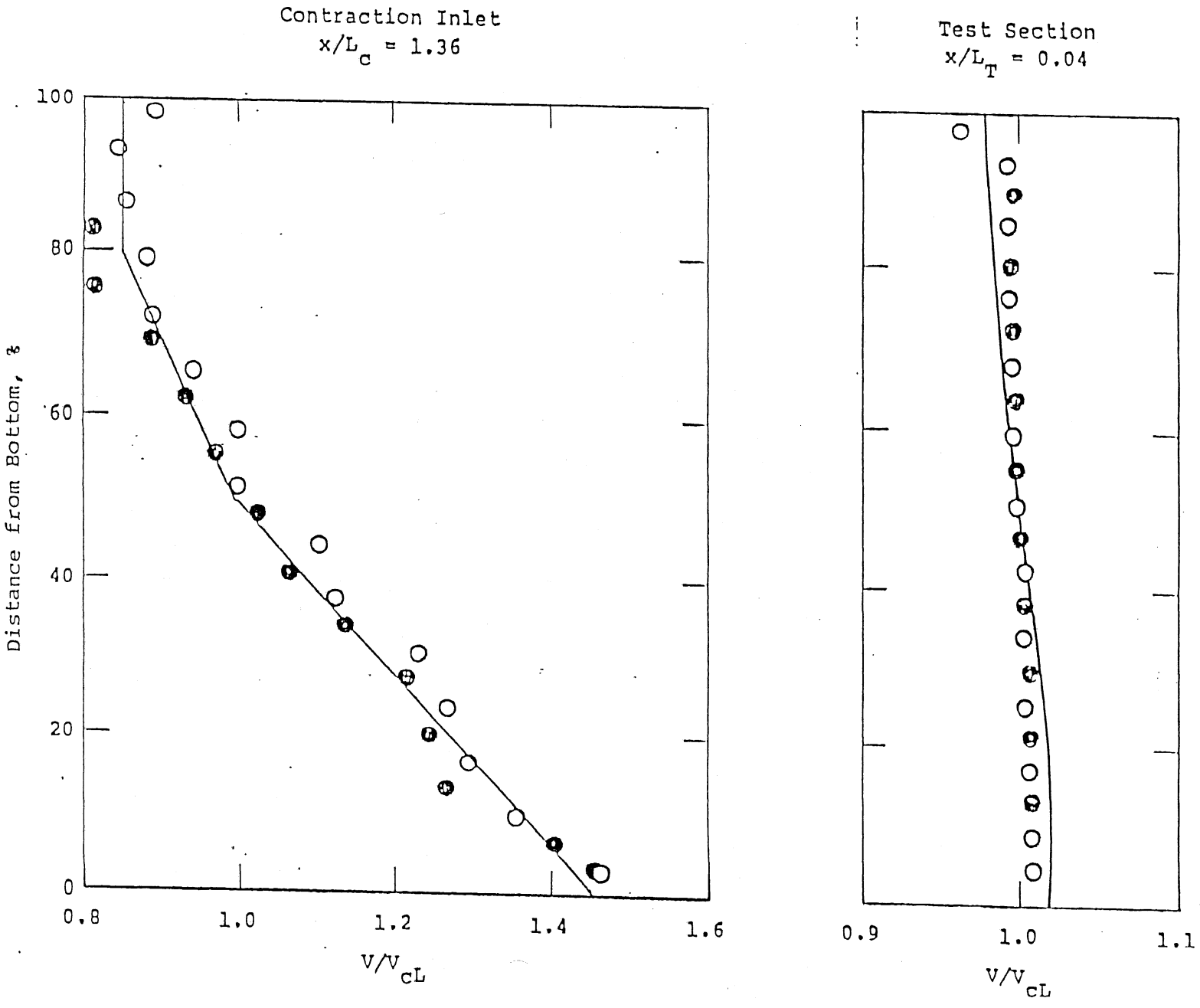

Fig. 16. Vertical velocity profiles on centerlines (Run No. 2).

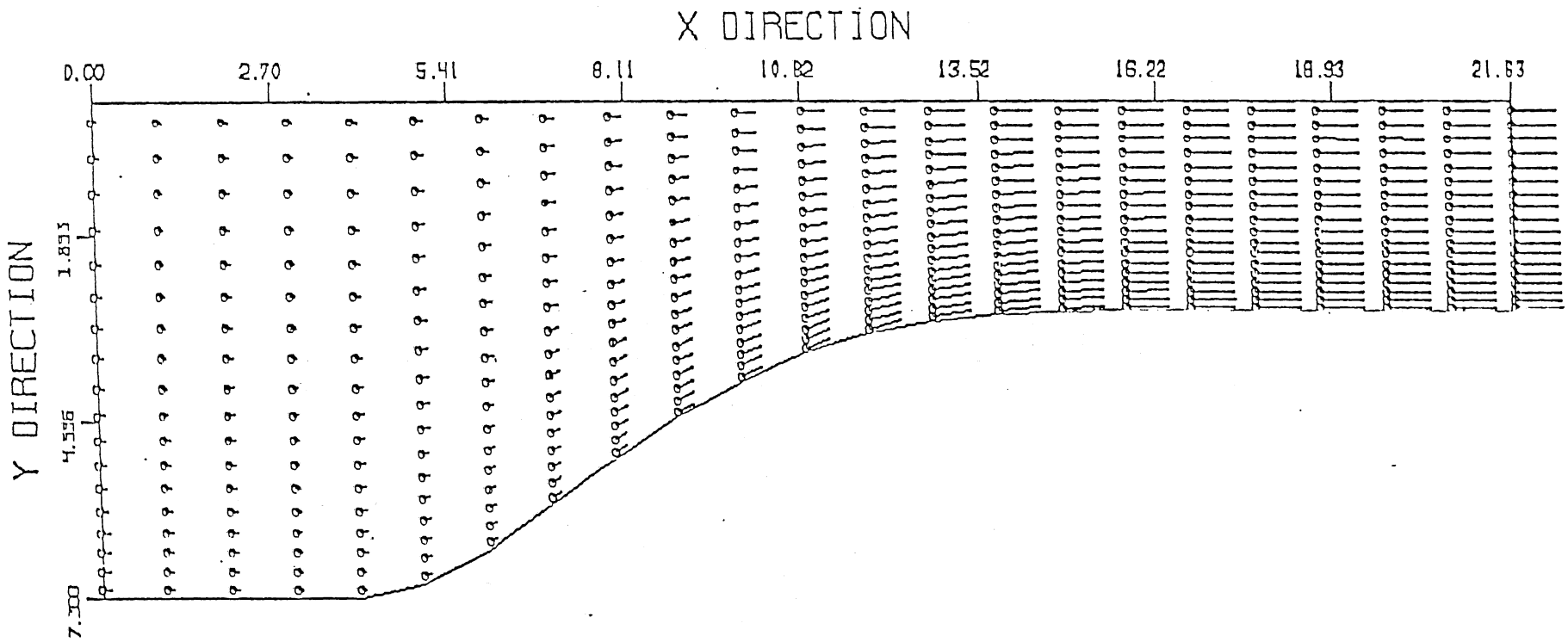

Fig. 17. (u,v) distribution on the plane of symmetry, Non-Uniform Velocity distribution A (Run No. 2).

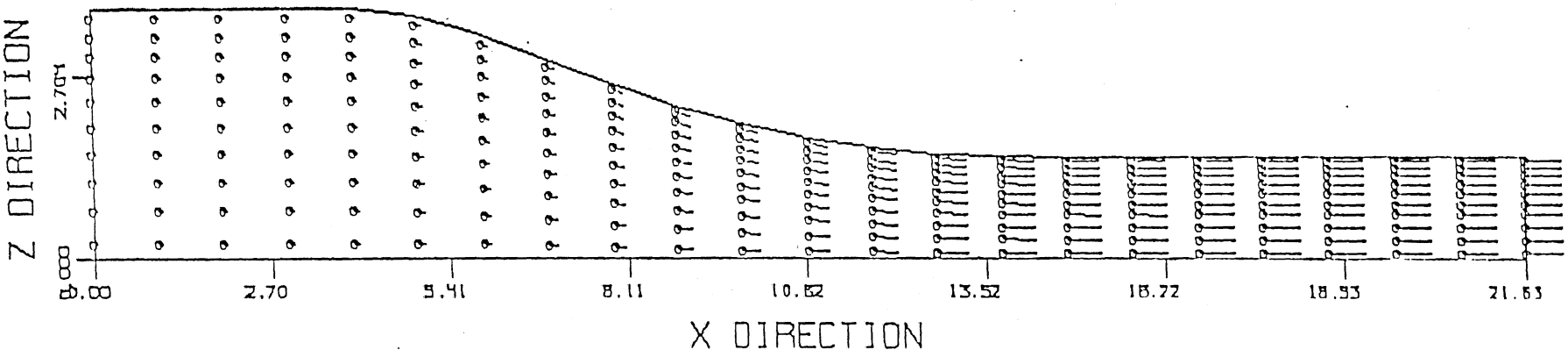

Fig. 18. (u,w) distribution on half of the top surface, Non-Uniform Velocity distribution A (Run No. 2).

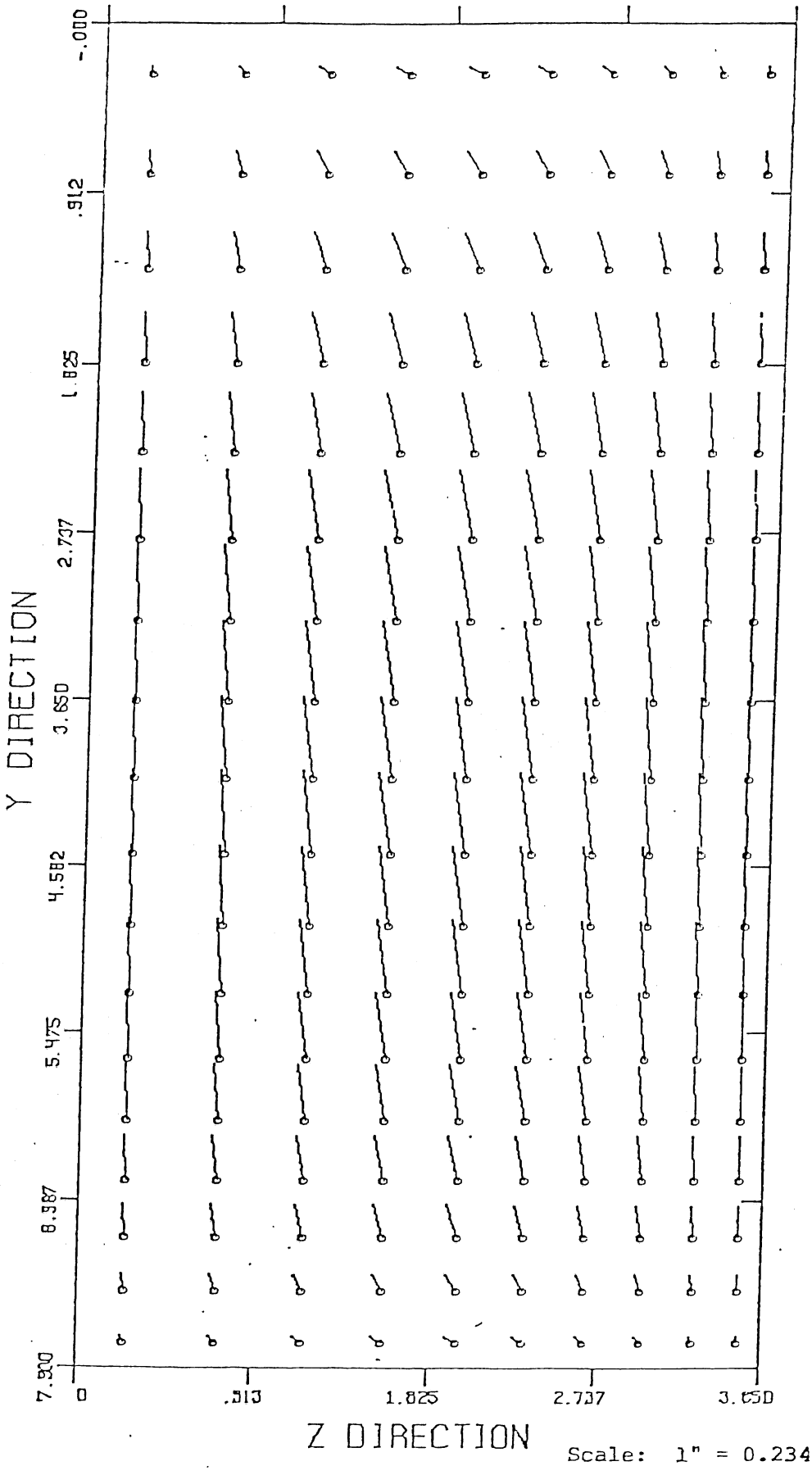

Fig. 19. (v,w) distribution on the cross section about 1.5 m upstream of the beginning of the contraction (Run No. 2).

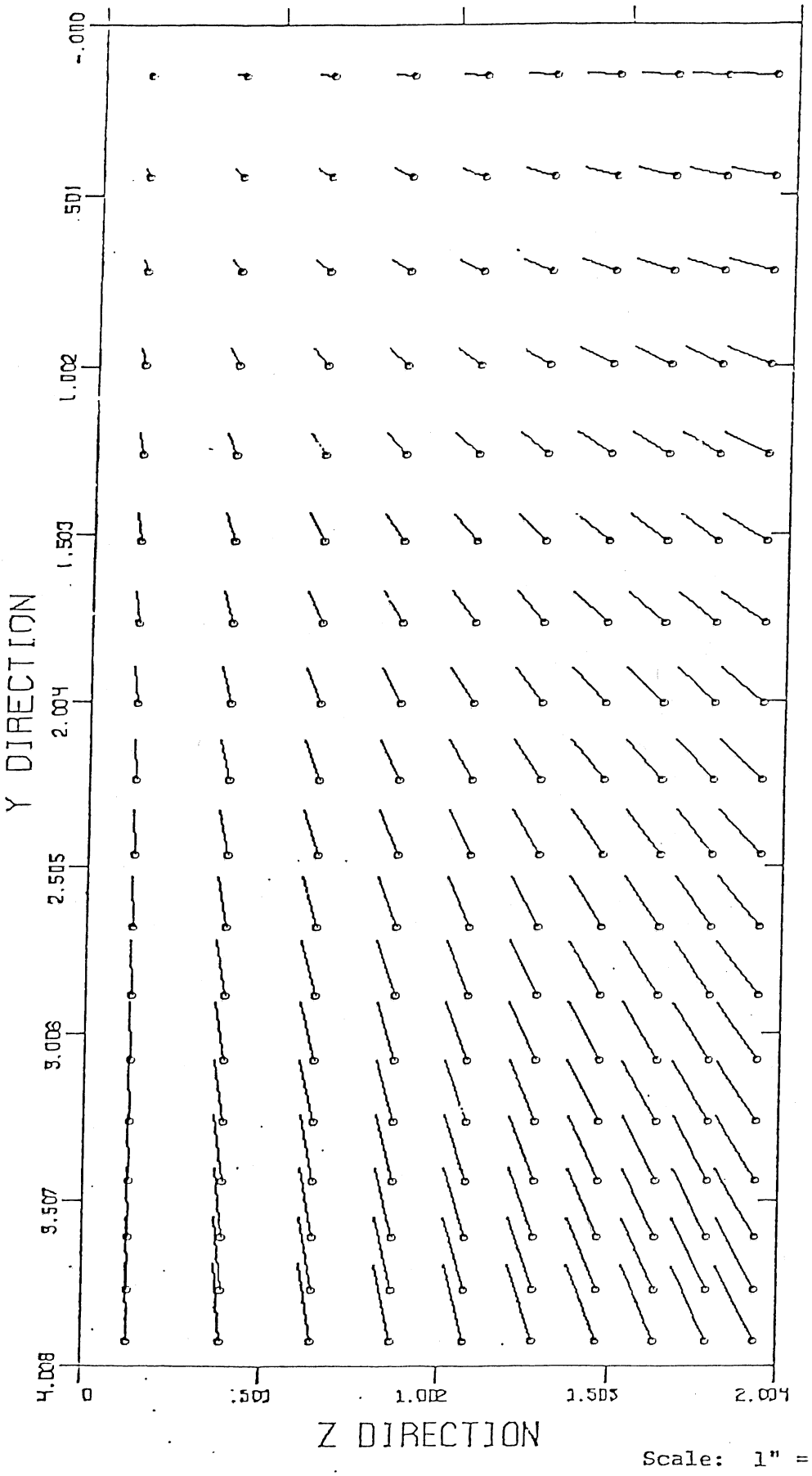

Fig. 20. (v,w) distribution on the cross section about 1.5 m upstream of the beginning of the contraction (Run No. 2).

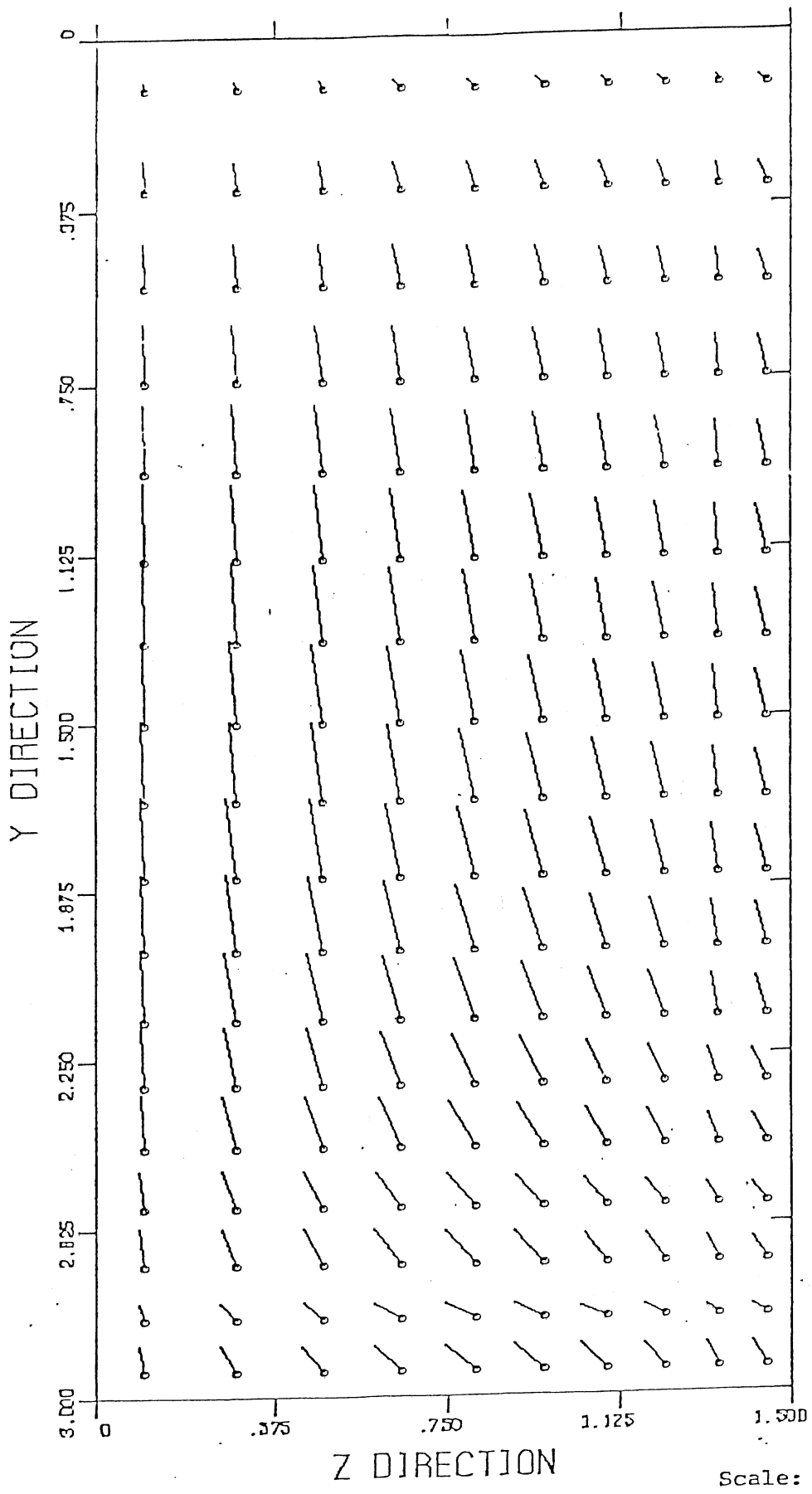

Fig. 21. (v,w) distribution on the cross section at about 0.5 m downstream of the end of the contraction (Run No. 2).

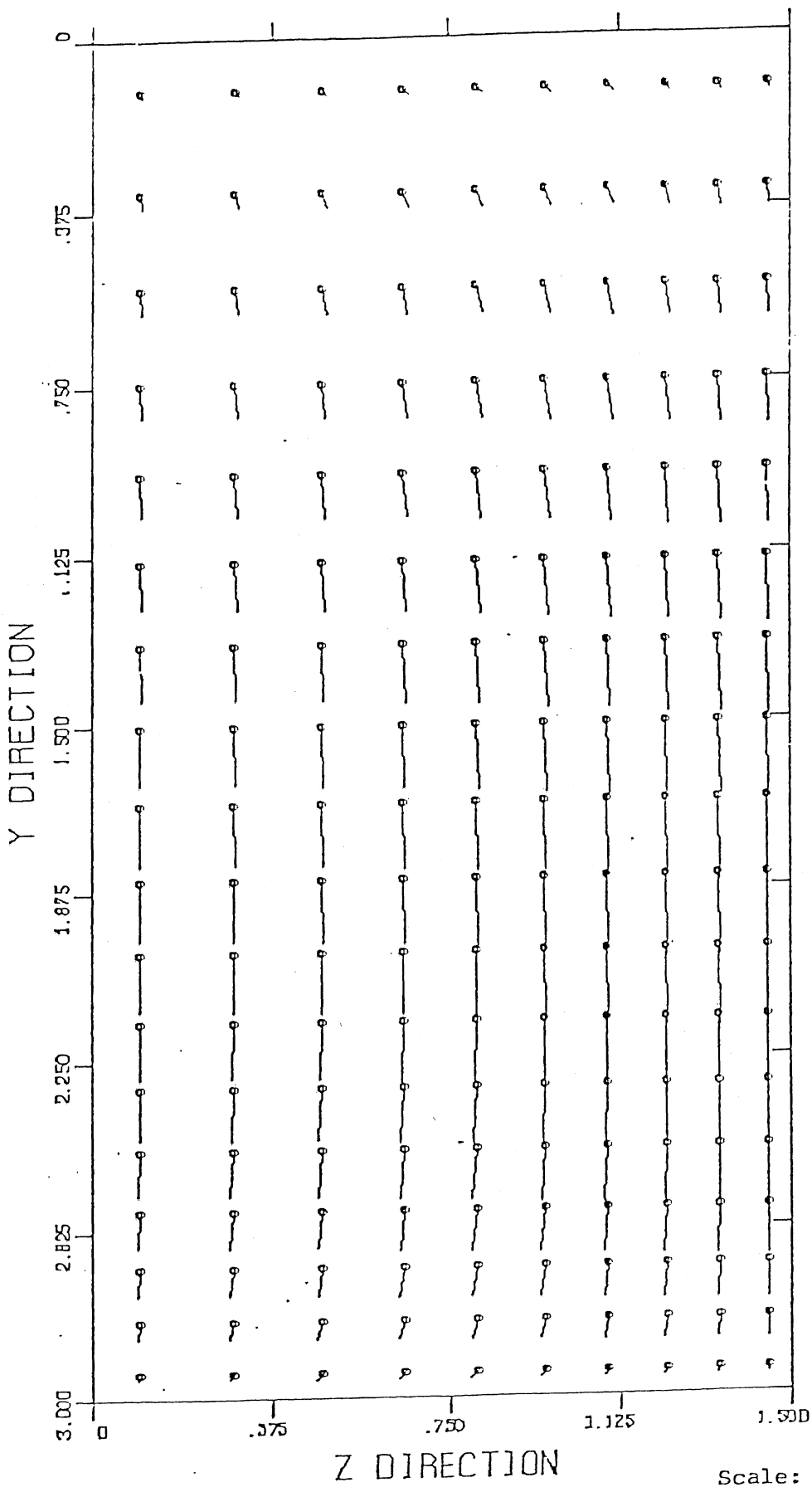

Fig. 22. (v,w) distribution on the cross section at about 2.5 m downstream of the end of the contraction (Run No. 2).

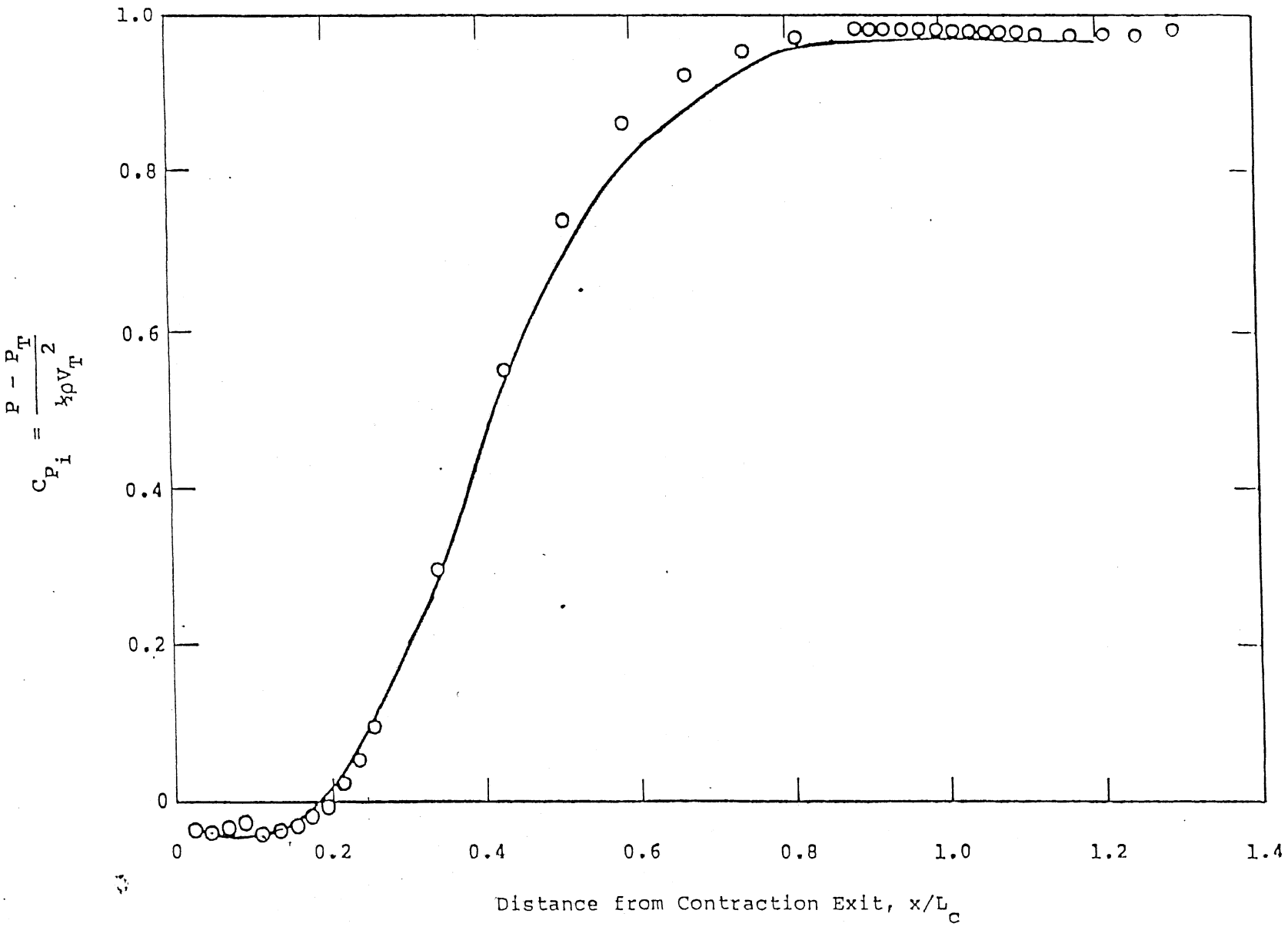

Fig. 23. Pressure coefficient along the centerline of the bottom surface (Run No. 2).

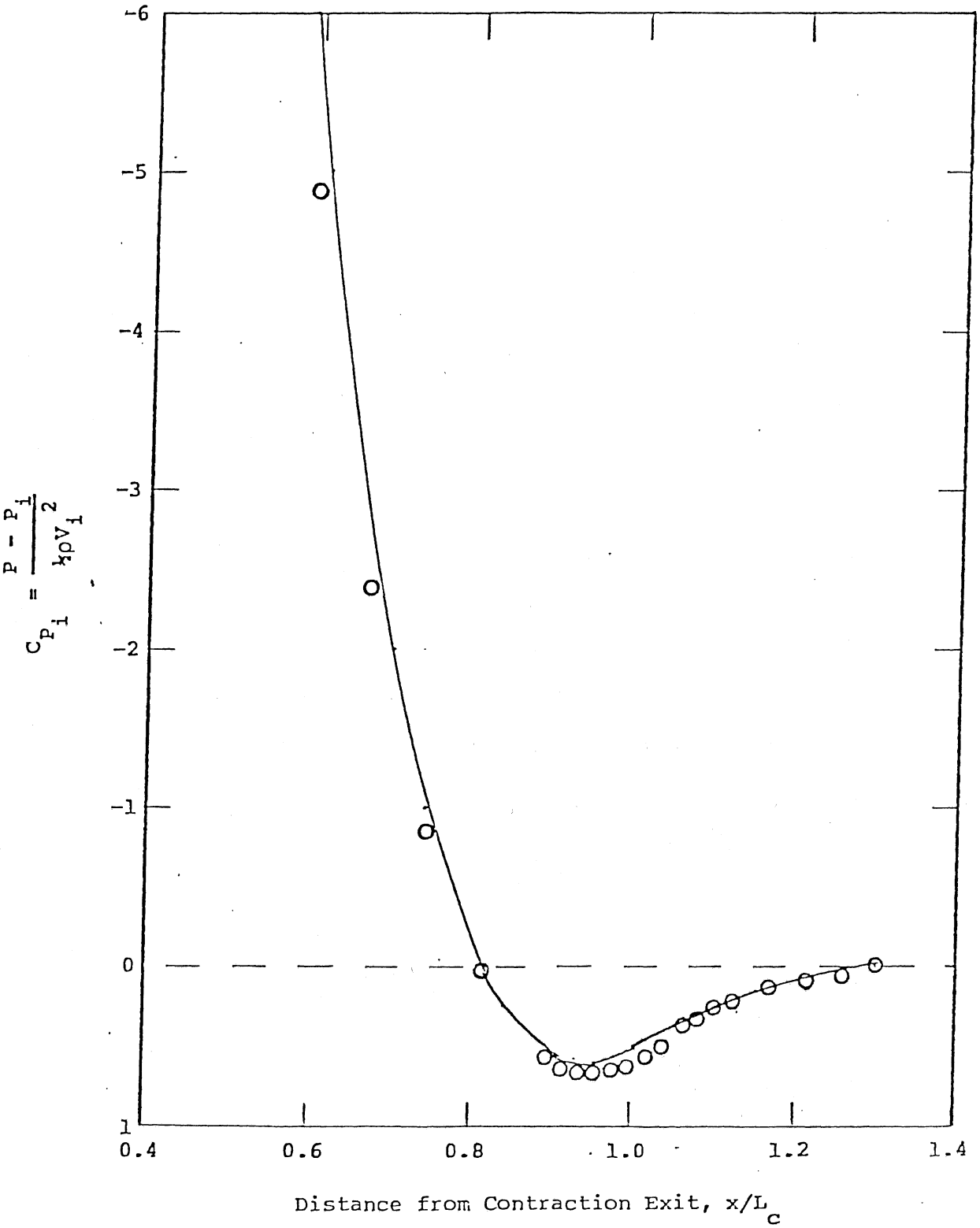

Fig. 24. Pressure coefficient along the center line of the bottom surface near the beginning of the contraction (Run No. 2).

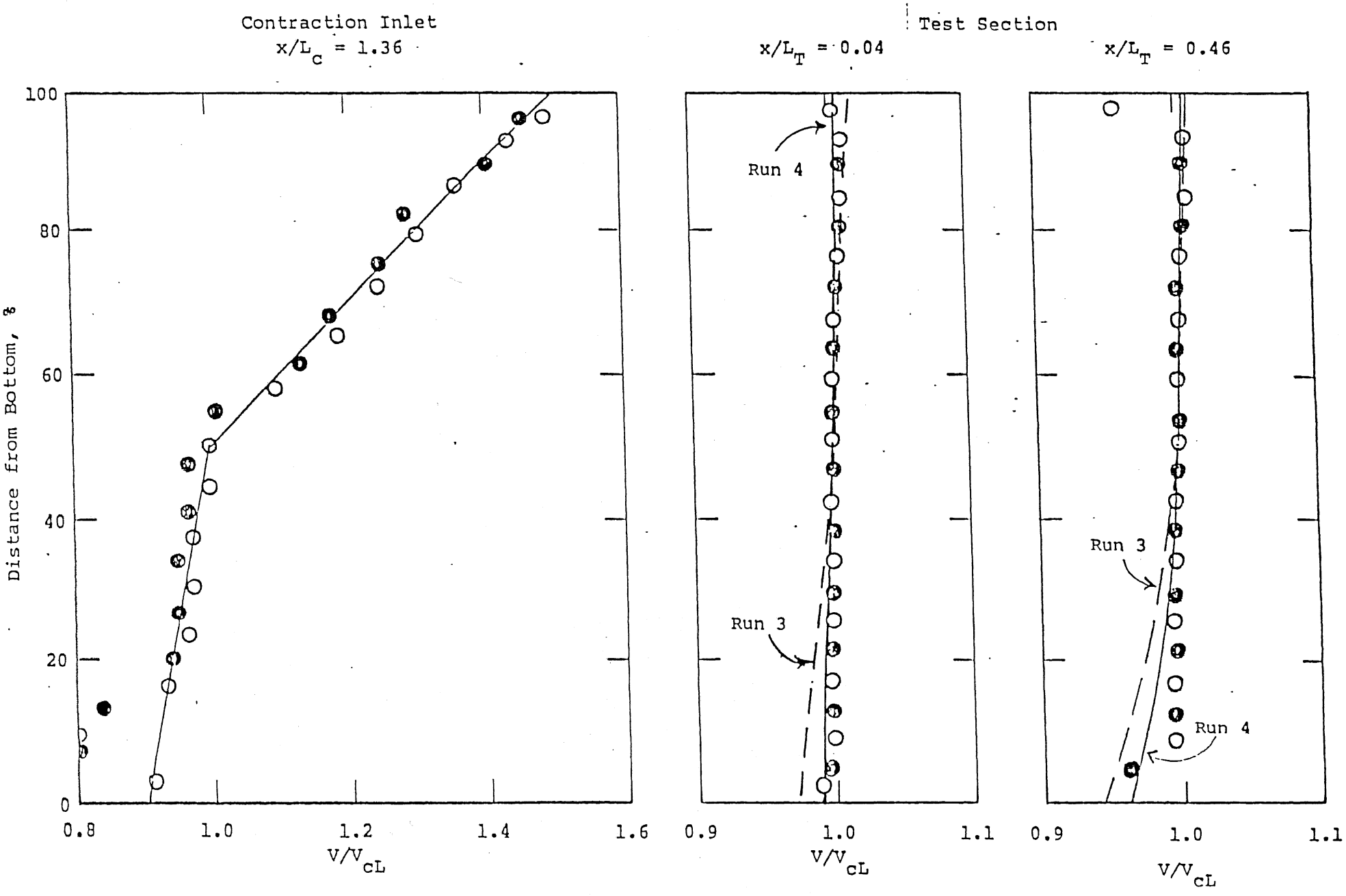

Fig. 25. Vertical velocity profiles for non-uniform flow B (Runs No. 3 and No. 4).

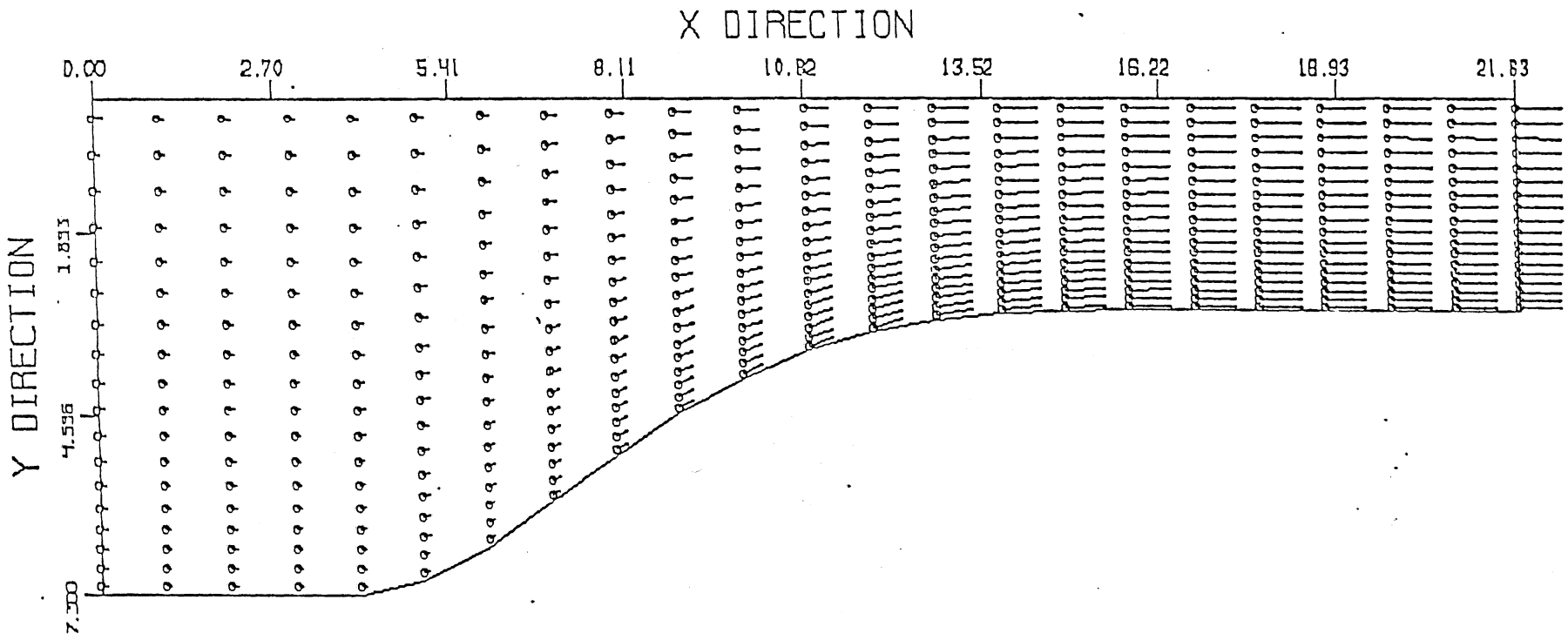

Fig. 26. (u,v) distribution on the plane of symmetry, non-uniform velocity distribution B (Run No. 3, small numerical viscosity).

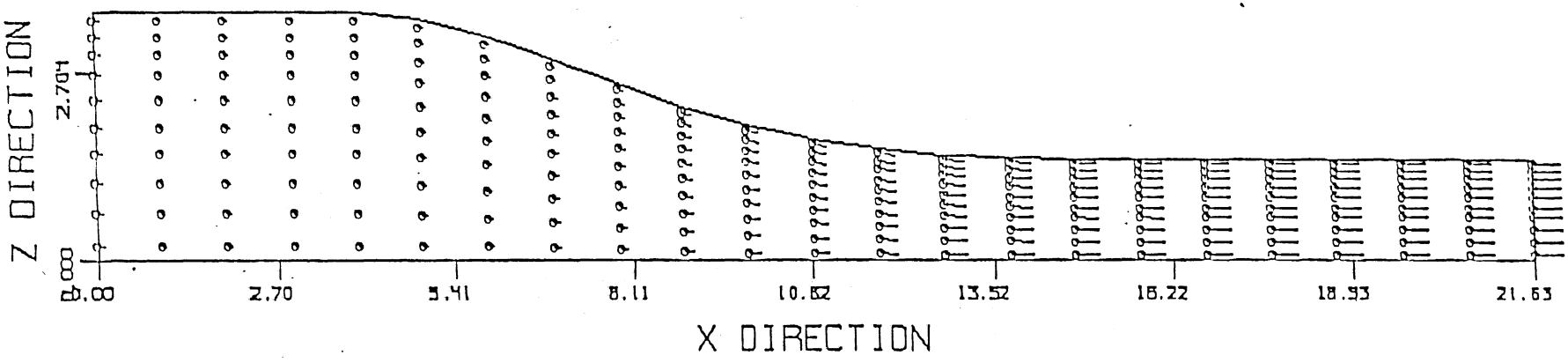

Fig. 27. (u,w) distribution on half of the top surface, non-uniform velocity distribution B (Run No. 3, small numerical viscosity).

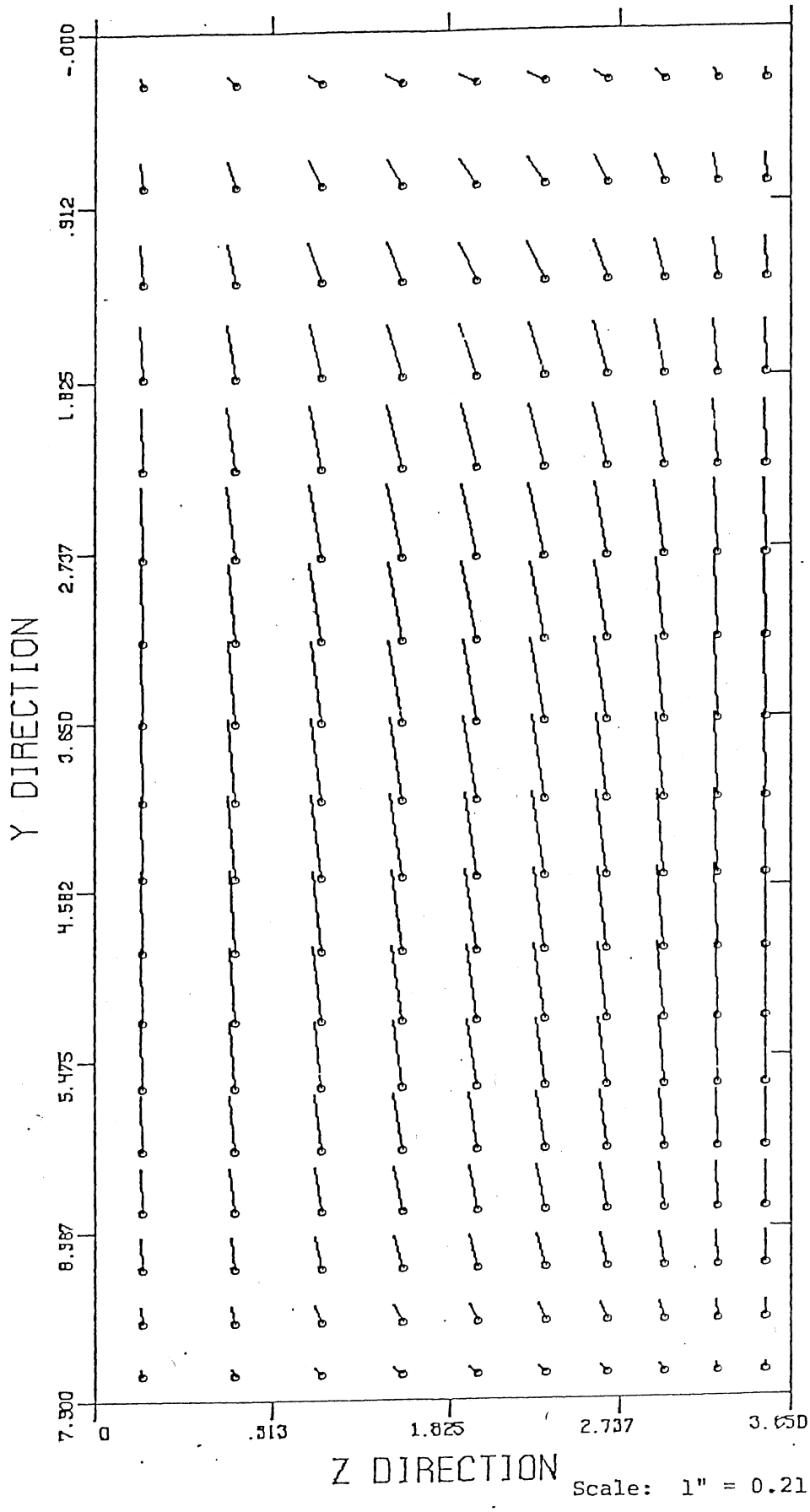

Fig. 28. (v,w) distribution on the cross-section about 1.5 m upstream of the beginning of the contraction, Non-Uniform Velocity distribution B (Run No. 3, small numerical viscosity).

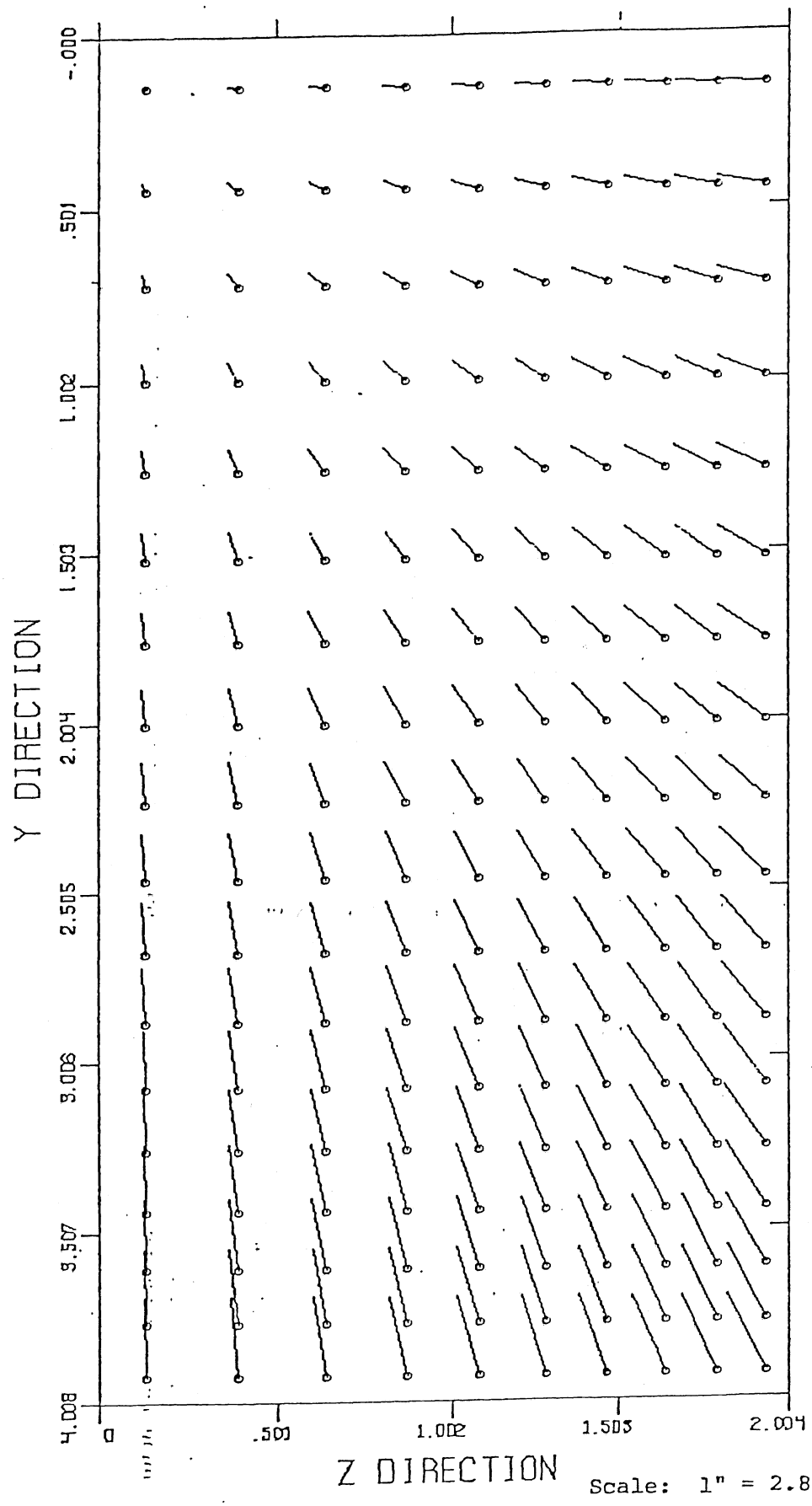

Fig. 29. (v,w) distribution on the cross-section at the middle of the contraction, Non-Uniform Velocity distribution B (Run No. 3, small numerical viscosity).

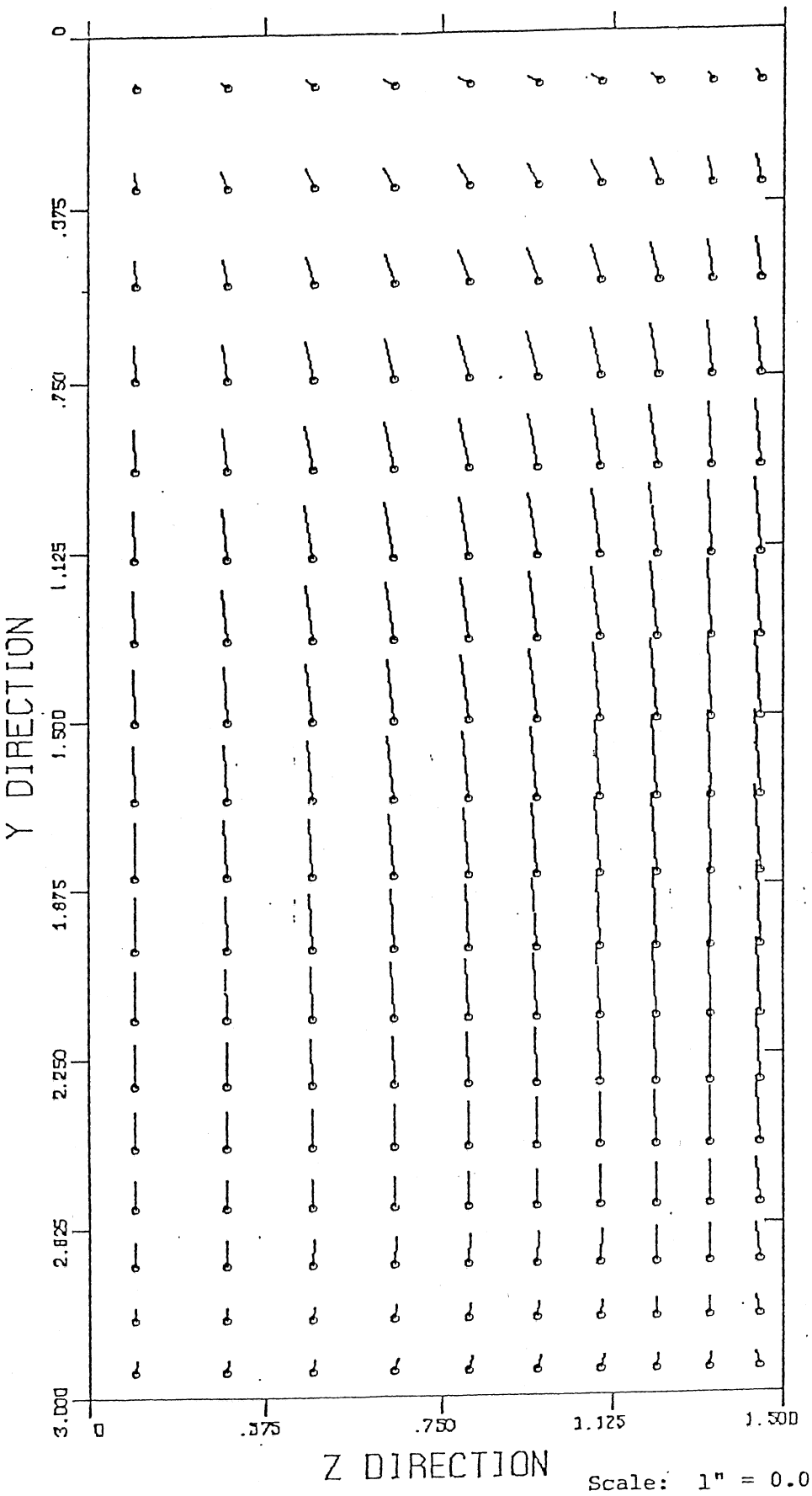

Fig. 30. (v,w) distribution on the cross-section at about 0.5 m downstream of the end of the contraction, Non-Uniform Velocity distribution B (Run No. 3, small numerical viscosity).

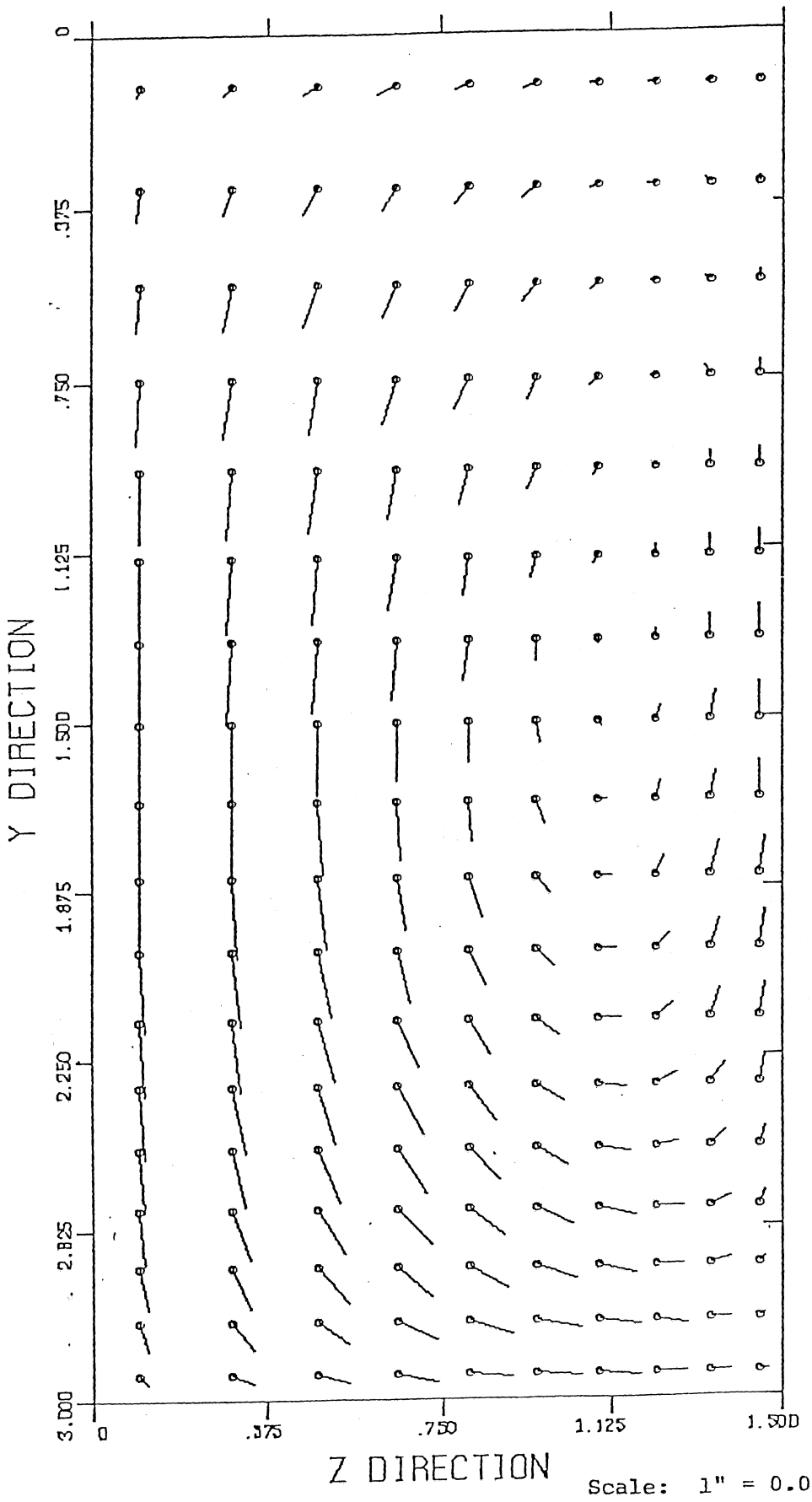

Fig. 31. (v,w) distribution on the cross-section at about 2.5 m downstream of the end of the contraction, Non-Uniform Velocity distribution distribution B (Run No. 3, small numerical viscosity).

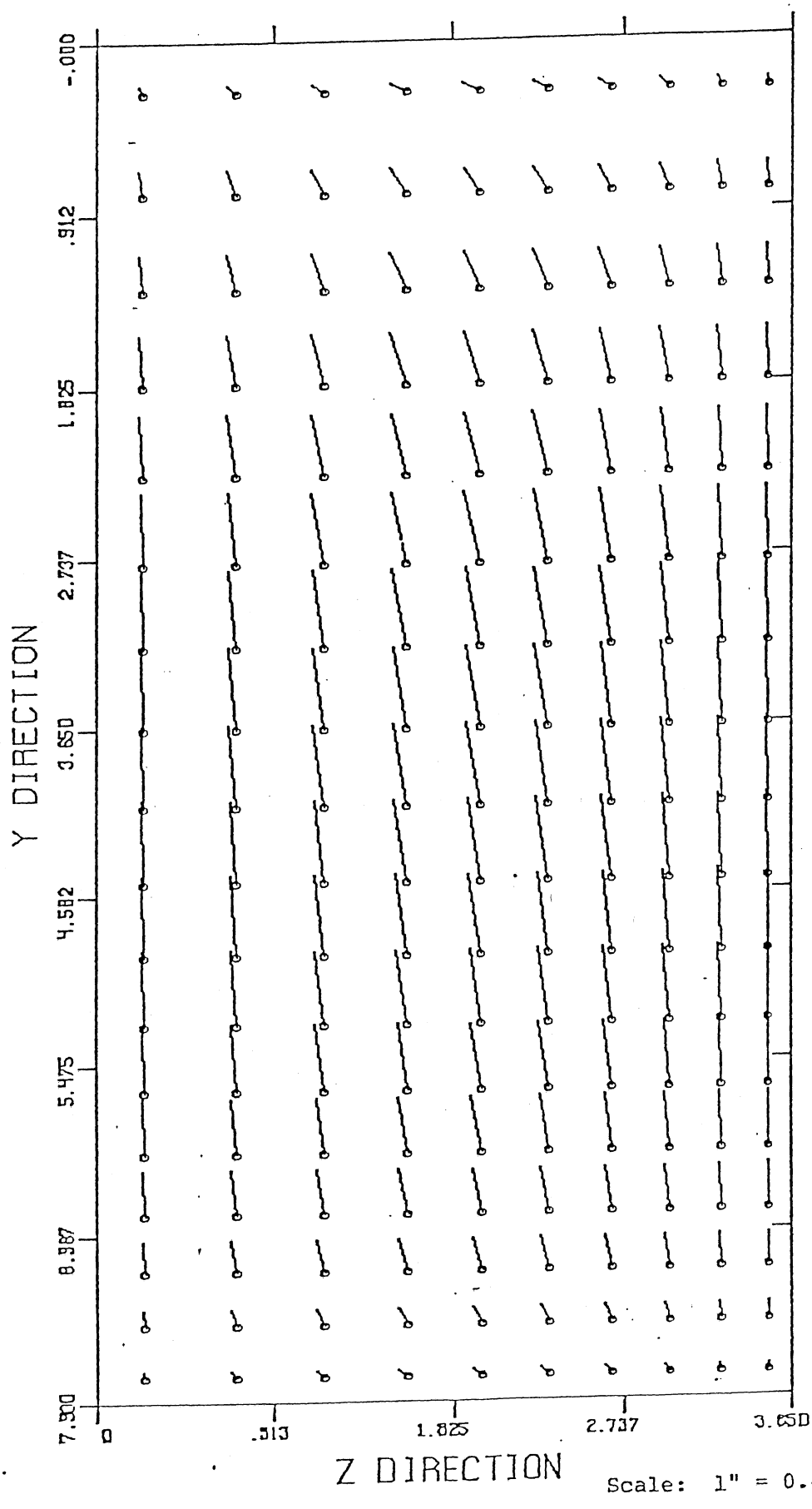

Fig. 32. (v,w) distribution on the cross section at about 1.5 m upstream of the beginning of the contraction, Non Uniform Velocity distribution B (Run No. 4, large numerical viscosity).

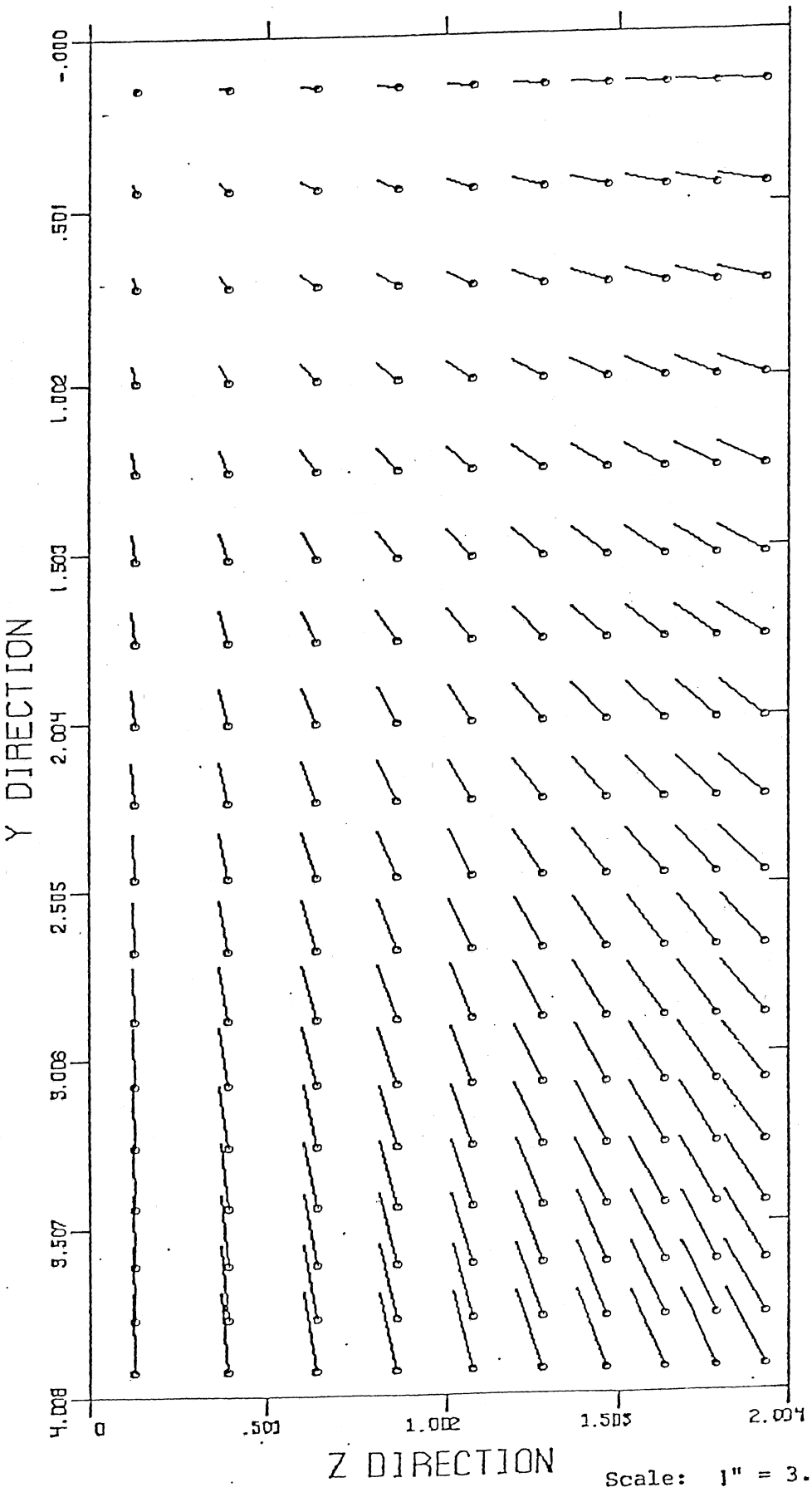

Fig. 33. (v,w) distribution on the cross section at the middle of the contraction, Non Uniform Velocity distribution B (Run No. 4, large numerical viscosity).

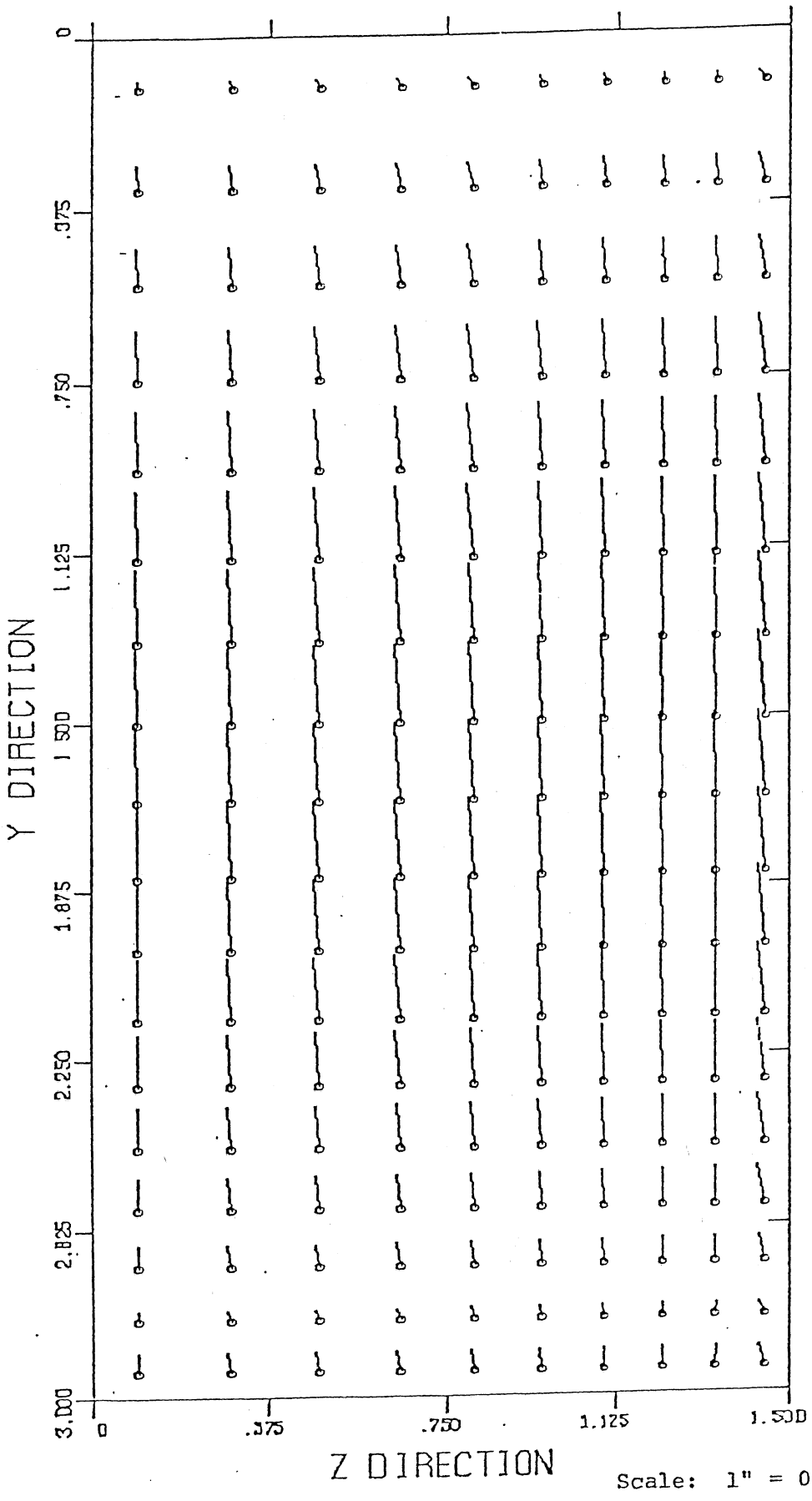

Fig. 34. (v,w) distribution on the cross section at about 0.5 m downstream of the end of the contraction, non uniform velocity distribution B (Run No. 4, large numerical viscosity).

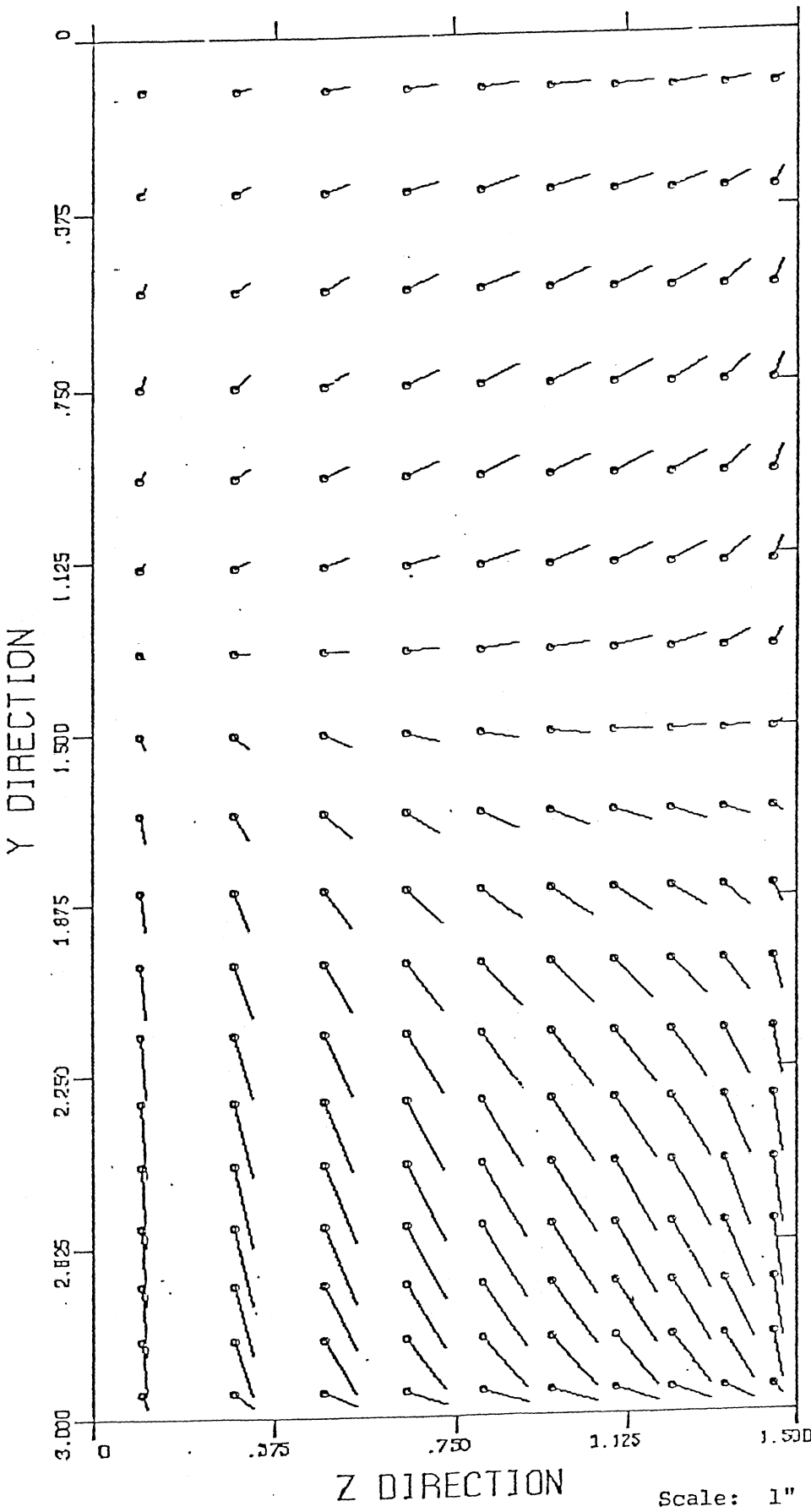

Fig. 35. (v,w) distribution on the cross section at about 1.5 m downstream of the end of the contraction, non uniform velocity distribution B (Run No. A

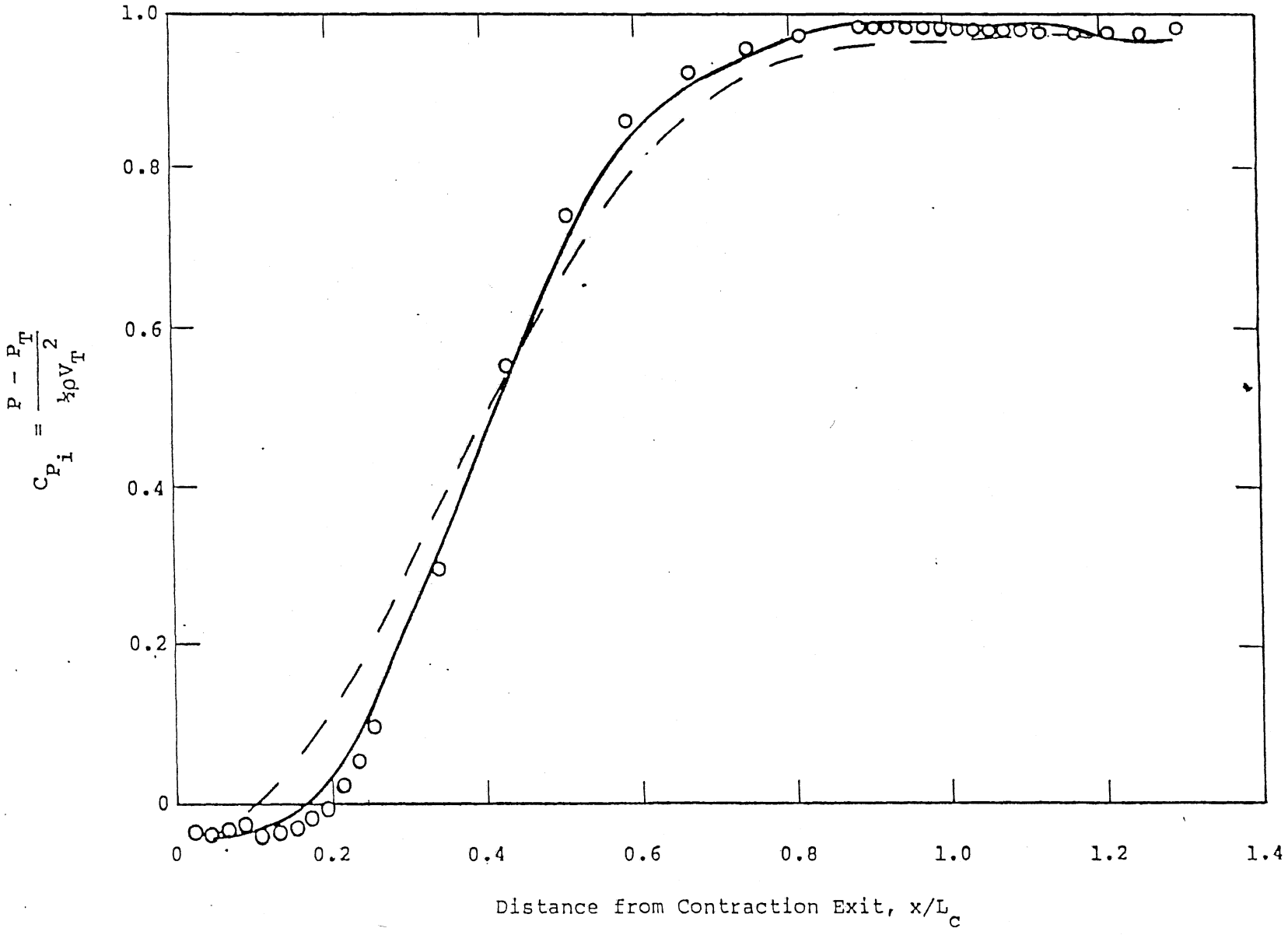

Fig. 36. Pressure coefficient along the center line of the bottom surface, non-uniform velocity distribution B (Runs No. 3 and No. 4).

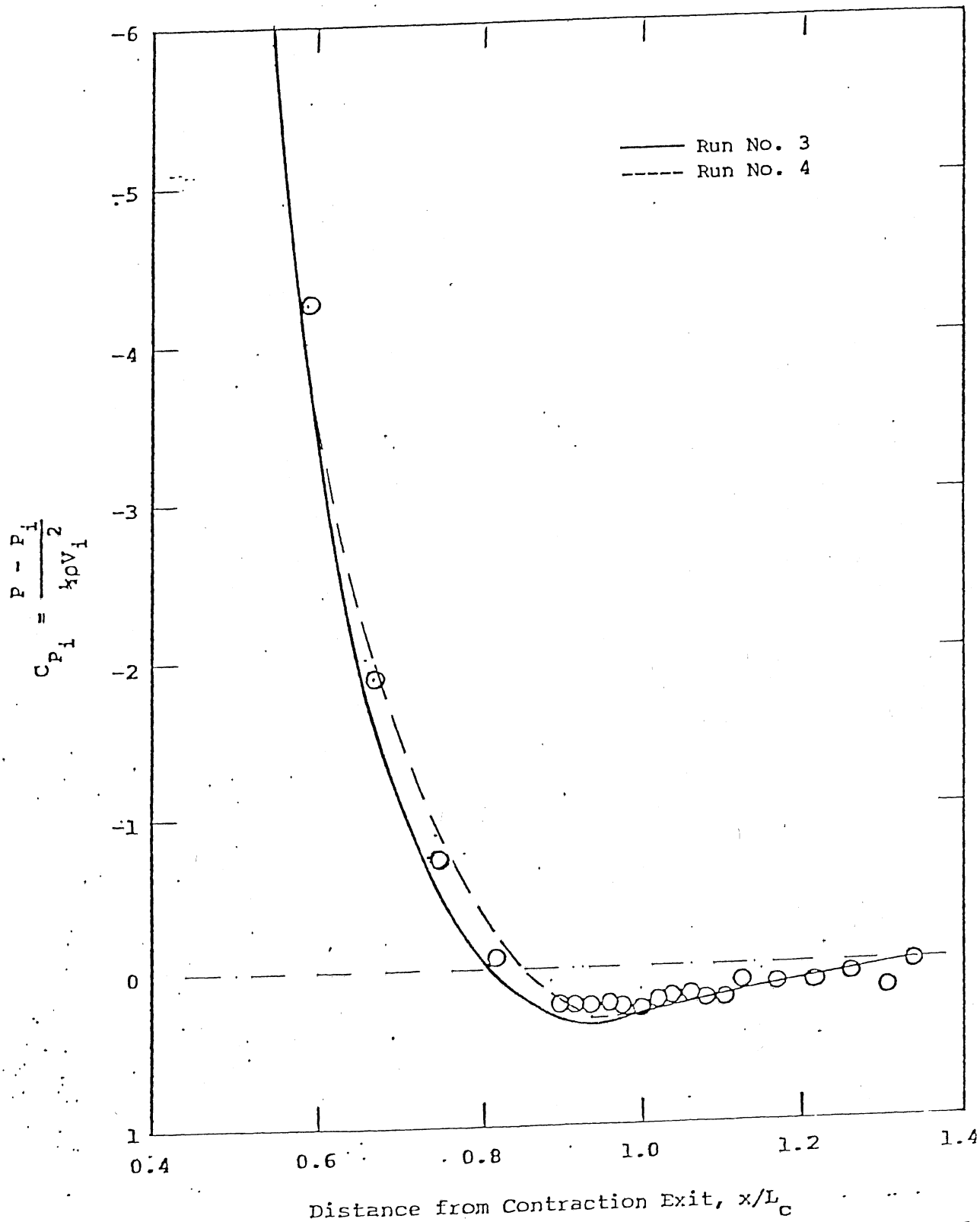

Fig. 37. Pressure coefficient along the center line of the bottom surface near the beginning of the contraction, non uniform velocity distribution (Run No. 3 and No. 4).

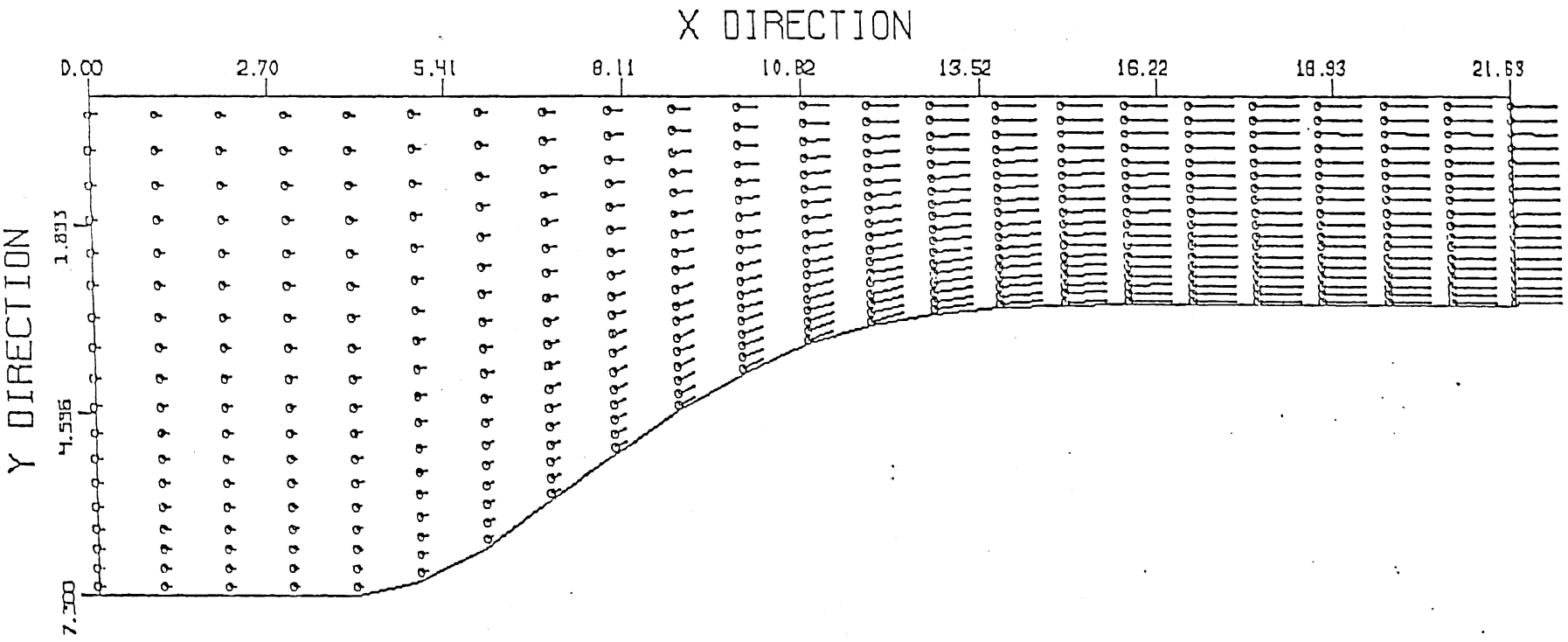

Fig. 38. (u,v) distribution on the plane of symmetry, uniform velocity distribution (Run No. 5).

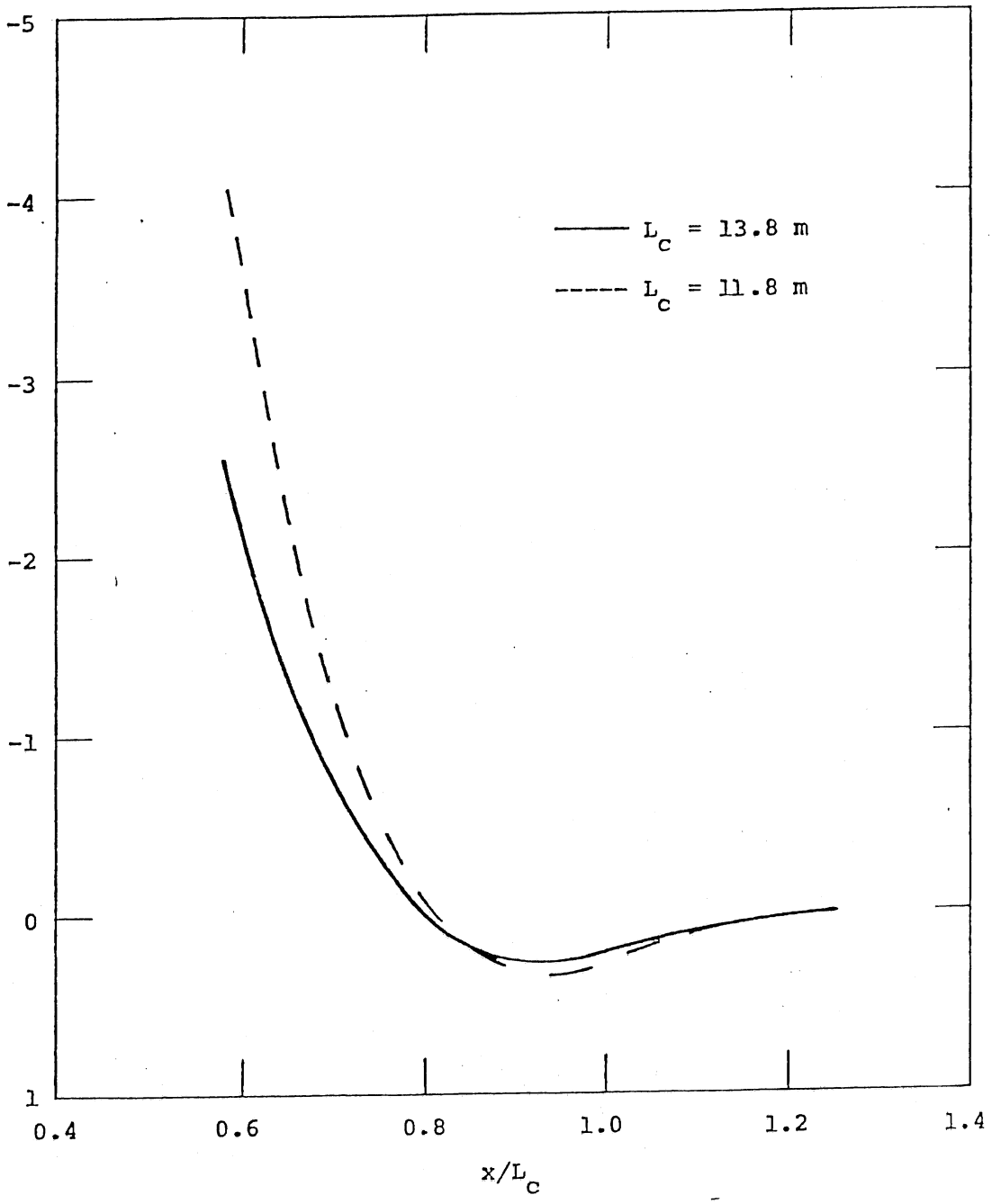

Fig. 39. Pressure coefficient along the center line of the bottom surface near the beginning of the contraction (Runs No. 5 and No. 6).

Final Report on Phase A-2, Task C:

Evaluation of Overall Hydrodynamic Performance of the Large Cavitation Channel (LCC)

by

J. M. Wetzel, R. E. A. Arndt, T. Morel,
C. C. S. Song, and J. M. Killen

St. Anthony Falls Hydraulic Laboratory
University of Minnesota
Minneapolis, Minnesota 55414

Prepared for

SSV&K/DMJM:Joint Venture
1709 New York Ave., N.W.
Washington, D.C. 20006

July 1983

Task C: Evaluation of Overall Hydrodynamic Performance of the Large Cavitation Channel (LCC)

by

J. M. Wetzel, R.E.A. Arndt, T. Morel*, C.C.S. Song, and J. M. Killen

St. Anthony Falls Hydraulic Laboratory, University of Minnesota

I. INTRODUCTION

This task consists of an evaluation of several items related to the overall hydrodynamic performance of the LCC. The Task A report has included experimental data on the hydrodynamic characteristics of the K&R contraction and diffuser. Results of the mathematical modeling of the K&R contraction have been presented in the Task B report. Based on the findings in these two tasks, modifications of the preliminary design are suggested that should result in an improvement of the overall performance. As good agreement has been obtained between the physical and mathematical model for the K&R contraction, the modifications are based primarily on further analysis of contraction shapes using the math model. The experimental data for the K&R diffuser have been used to suggest a change in the transition design and also served as the basis for computations to assess the cavitation susceptibility of the turning vanes in the first elbow. A preliminary evaluation has also been made of several concepts for alternate test sections that could be utilized within the overall configuration of the LCC established for the 10x10x40 ft closed test section.

---

*Present with Integral Technologies, Inc.

II. MODIFICATIONS TO THE PRELIMINARY K&R DESIGN

A. Contraction

1. Preliminary Kempf and Remmers Design

The original design proposed by Kempf and Remmers specified an asymmetric contraction going from 7.3 m square to 3 m square. The top wall is straight and horizontal. The bottom and the side wall shapes are prescribed by an equation proposed by Schreck and used by Wille [1] in one of his studies:

$$\frac{r - R_1}{R_2 - R_1} = \left(\frac{z}{L}\right)^3 \left[2 - \left(\frac{z}{L}\right)^3\right] \qquad (1)$$

where R_i is the transverse exit dimension, R_2 is the inlet dimension, L is the nozzle length, r is the transverse wall coordinate and z is the streamwise coordinate. Although all sides are prescribed by the same equation, due to the asymmetry the bottom wall contracts twice as much as the two side walls. Analyzing the Schreck equation, one observes that even though it is a sixth order curve, it reduces at the inlet end to a parabola, and at the exit end to a cubic.

A 1/10 scale model of the contraction was built and tested using air flow, as described in the Task A report. The model was equipped with numerous taps for wall pressure measurement, and some data obtained are shown in Figs. 1 and 2, where mean curves have been drawn through the data points.

The area of most concern in this contraction was the lower surface because it has the largest curvature, especially the corner region influenced additionally by the side wall curvature. This expectation was borne out by the

experimental data showing the largest pressure extrema in the bottom corner. Similar extrema can be seen in the data taken along the bottom centerline, but the top corner had no extrema at all, indicating an almost smooth flow acceleration from the settling chamber to the test section taking place in this area.

At the exit end of the contraction, the pressures along the bottom surface reached a minimum around $C_p = 0.04$, i.e., a value low enough to give no concern from the point of view of flow separation. Based on these values one would expect that the velocity profile at the contraction exit plane will have only a small non-uniformity caused by streamline curvature inside the contraction; this nonuniformity should be on the order of 0.75 percent, which is within the prescribed requirements. (It should be noted that this type of nonuniformity decays rapidly, exponentially within the test section, and thus such a small value is of no concern.) The experimental velocity profiles measured at the contraction exit in the 1/10 scale model confirmed that the nonuniformity is indeed very small.

At the inlet end the pressure coefficients were much larger, reaching values of 0.44 in the lower corner. The corner pressure profile had a nontypical shape without a clean prominent maximum, which suggested possible flow separation. Tufts placed along the bottom surface indicated localized separation in the bottom corner at the contraction inlet plane, and these two findings gave rise to concerns about the K&R design.

The onset of separation is governed, according to the Stratford's criterion [2], by two main parameters: maximum value of C_p and dC_p/dx. The Kempf and Remmers nozzle is relatively abrupt at the inlet end, which leads to high values of C_p. Furthermore, the parabolic variation at the inlet means that there is a discontinuity in wall curvature at the inlet plane, giving rise to a very

steep gradient of C_p . Both of these combine to produce the observed separation, which could be further enhanced by nonuniform inlet conditions in the settling chamber.

2. Modified K&R Contraction

As mentioned under Task B, one alternative contraction profile was tested with the time dependent three-dimensional flow mathematical model. This alternative contraction is a simple extension of the K&R design with the total contraction length increased from 11.8 meters to 13.8 meters. The total contraction L_c can be divided into two parts: the inlet part L_i , and the exit part L_e , at the point of inflexion. For the K&R design, this will result in $L_i = 0.2632\ L_c$ and $L_e = 0.7368\ L_c$. This means only 0.5264 m was added to the inlet part and 1.4736 m was added to the exit portion.

The computed pressure coefficient C_{pi} along the centerline on the bottom surface for the original contraction (dotted line) and for the alternate contraction (solid line) are compared in Fig. 3. This figure indicates a 27 percent reduction in the adverse pressure gradient in the inlet portion of the contraction due to a 14 percent increase in the contraction length. The pressure coefficients referred to the test section condition, C_{pt} , along the centerline on the bottom surface are plotted in Fig. 4. This figure shows that the pressure coefficient C_{pt} in the exit portion is nearly identical when compared for two points having the same relative positions. The pressure coefficients C_{pt} along the bottom corner without fillet are plotted in Fig. 5. The adverse pressure gradient near the exit is reduced by lengthening the contraction.

The contraction geometry specified by the K&R design may not necessarily be the optimum shape. It may be possible to lengthen the entrance part more than the exit part. However, one must be very careful when trying to reduce the

length of the exit portion because the modeling results under Task B have suggested that there are problems of secondary currents and vortices. The damping of oscillatory motions generated by the propeller could also be influenced by the contraction geometry.

Further refinement on the contraction design should consider new geometrical forms with fillets and their effect on pressure distribution, uniformity of velocity distribution at the test section, secondary currents and vortices (which may affect the critical cavitation number), and flow unsteadiness as influenced by nonuniform and unsteady inflow conditions. The time dependent three-dimensional flow model currently available is an excellent tool for this purpose.

3. Matched cubic design

Due to the necessary time for development of improved computational techniques as described in Task B, a parallel study of alternatives to the Kempf and Remmers design was initiated. This study utilized the same computer program used originally by Morel to develop his contraction design procedures. This program solves the Euler equations for two-dimensional or axially symmetric shapes. The idea to use this program and apply it to a rectangular nozzle was triggered by the observation that the experimental pressure profiles measured along the centerline and along the corner of the bottom surface were not very different. Further, the contraction ratio in the top and side elevations are the same, producing the same area variation that an axisymmetric nozzle would have. Thus, it was reasoned that a meaningful approximation to the flow could be generated by an axisymmetric calculation. This idea was tested by inputting the K&R coordinates into the axisymmetric program, and the results were compared to the experimental data (see broken lines in Figs. 1 and 2). The agreement was very encouraging, suggesting that the axisymmetric calculations might be

utilized during the development period of the truly three-dimensional program, and during this interim could be used to provide guidance in consideration of an alternate design.

Because of the extremely tight time constraints in this program, coupled with the desire to study as many options for modification to the preliminary K&R design as possible, it was decided that this approximate procedure would be utilized as an extension to the axisymmetric nozzle design procedure of Morel [3, 4] while the new computer program would be used initially to study the preliminary K&R design. Continuing with the philosophy of considering as many design options as possible, a different design modification was subsequently considered with the new program as described above.

The design modification considered herein results in a contraction that is about ten percent longer than the original K&R design, with a total length of 13 m. The shape is described by the following equation:

$$\frac{r - R_2}{R_1 - R_2} = 1 - \frac{1}{X^2}\left(\frac{z}{L}\right)^3 \qquad \frac{z}{L} < X$$

$$= \frac{1}{(1 - X)^2}\left(1 - \frac{z}{L}\right)^3 \qquad \frac{z}{L} > X \qquad (2)$$

where X is a dimensionless shape factor and the other parameters are the same as in the Schreck/Wille formula. The chosen dimensionless shape factor defining the match point of the two cubics is X = 0.37, which gives almost the same shape at the exit as the original K-R design, while providing a more gradual inlet end. Another difference lies in the maximum wall slope, which for the original K-R design is 35.5 degrees along the bottom wall, while the new design has a maximum slope of 43.4 degrees.

Using this approach a matched cubic design was finalized for which the axisymmetric calculations showed $C_{pT} = 0.044$ and $C_{pi} = 0.41$. By contrast, the original K&R design evaluated using the approximate axisymmetric model gave $C_{pT} = 0.044$ and $C_{pi} = 0.55$. Although the axisymmetric results cannot be applied directly to the actual rectangular contractions, the change in C_{pi} obtained is believed to be a reliable indication of the improvement that will result by modifying the K&R design discussed in Task B.

The modification considered herein results in a lengthening of the contraction that is applied exclusively to the low speed inlet end. Therefore, some of the resulting change in length could be compensated by a reduction in the length of the settling section. This is true since the added length which is only slowly varying in cross section, is available for turbulence decay, and so it may be viewed for the most part as an extension of the settling chamber.

By way of contrast, a stretching of the K&R contraction was considered in Section A.2 above. It is believed that some of the increased length in that design could also be compensated for by a reduction in the length of the settling section using the arguments cited above.

B. Diffuser Transition Section

1. Preliminary K&R Design

To minimize the possibility of cavitation in the system, one has to take care to avoid low pressures in the test section area where the pressure is the lowest of the whole circuit. One precaution that is often taken is to place a gradual transition section between the test section and the diffuser; Kempf and Remmers proposed constructing this transition in two parts. In the first part the side walls are kept parallel, and the bottom alone is curved. In the second section the bottom becomes straight (but inclined at 4.972 degress), and the two

sides open gradually outward along a curved shape. The curve used to form the bottom shape is a quartic, and the side wall curve is a parabola. At the end of the second transition the side walls are inclined 2.75 degrees from the centerline. The whole transition section is 7 m long.

2. Alternate Design

The transition sections proposed by Kempf and Remmers are more gradual than the contraction exit end. It is our opinion that this is not necessary because, if cavitation should appear, it would do so at the contraction exit first. It seems more consistent simply to make the transition the same as the contraction exit. As previously shown in the contraction data, the pressure along the bottom wall did have a small minimum near the exit, but cavitation is not a concern at the bottom. At the top surface where the cavitation could in fact be a problem, the contraction data showed no pressure minimum. Thus, the asymmetric contraction works to an advantage in this respect, and using the contraction shape for the transition section should be adequate.

The proposed transition would thus be a cubic, in contrast to the K&R quartic. There is no advantage in going beyond the third power, which already guarantees continuous wall curvature. As a result the cubic is the shortest safe shape to produce the desired transition from parallel to diverging walls. Using the reverse of the contraction end for the transition has one positive attribute that the shape has already been validated in the scale model experiments.

In order to determine the length of the transition, the condition of tangency at the transition/diffuser juncture has to be used. Taking the diffuser spreading angle to be the same for both the width and the height with a value of 5.24 degrees (a mean of values used by Kempf and Remmers), the distance in which the cubic reaches that slope has to be calculated. The slope is given

by:

$$\frac{dr}{dz} = \frac{R_1 - R_2}{L(1-X)^2} \; 3\left(\frac{z}{L}\right)^2 \tag{3}$$

where $R_1 = 7.3$, $R_2 = 3.0$, $L = 13.0$, and $X = 0.37$. Equating this slope to 5.24 degrees z can be calculated:

$$\frac{dr}{dz} = 2.50014 \left(\frac{z}{L}\right)^2 = \tan 5.24^\circ = 0.09171$$

$$\frac{z}{L} = 0.19153$$

$$z = 2.4898 \text{ m} \tag{4}$$

The dimensions of the diffuser inlet (transition exit) may then be calculated from the cubic equation:

$$r = R_2 + \frac{R_1 - R_2}{(1-X)^2} \left(\frac{z}{L}\right)^3$$

$$r = 3 + 10.834 \left(\frac{z}{L}\right)^3$$

$$r = 3.0761 \text{ m} \tag{5}$$

The length of the straight-walled diffuser itself is obtained from:

$$L = (5.3 - 3.0761)/2 \tan 2.62^\circ = 24.300 \text{ m} \tag{6}$$

The total length of the transition plus the diffuser is then 26.790 m. The original design has a total length of 29.4851 m, i.e., the new design provides a saving of 2.695 m in overall length.

C. Diffuser

As mentioned above, the diffuser proposed by Kempf and Remmers has an average included angle of 5.24 degrees. The decision on whether this choice is adequate will be made at this time based on the 1/10 scale model study results, which were obtained with a bare tunnel. One critical question is whether the diffuser flow will remain attached, and preliminary results obtained with the empty test section showed no separation for that flow condition. Another question is whether the maximum velocity at the diffuser exit is not excessively large (insufficient velocity profile diffusion) to create concerns about cavitation occurring on the turning vanes in the first corner. The preliminary data obtained with the empty test section suggested a possibility of cavitation, since the maximum velocity at the diffuser exit was about seventy percent higher than the area-averaged velocity. This possibility will be discussed in the following section. Diffuser performance should be evaluated with blockage in the test section. As this was not included in the test program due to time and funding limitations, effects of model blockage in the test section should be evaluated in the 1 to 5 scale model.

D. First Elbow Guide Vanes

The placement of a vaned elbow in a region of low static pressure and high velocity may result in cavitation of the vanes. This is particularly true for the first elbow, which is exposed to the most extreme conditions. It is therefore desirable to examine the guide vanes for their cavitation susceptibility.

To carry out such an analysis, the pressure distribution for the vane profile is required at the angle of attack or stagger angle necessary to provide the proper turning action of the flow. No data are available for the

vane profile proposed by K&R in the preliminary design. However, some experimental data are available for the vane profile used in the DTNSRDC 36-inch water tunnel. These data were taken in model studies conducted at the Laboratory some years ago [5]. The tests indicated that the stagger angle required to provide the best turning action was about 101 degrees, and the measured minimum pressure coefficient on the upper surface was -2.25 for that angle. Assuming that cavitation will occur when the local pressure drops to vapor pressure, the critical cavitation number for the vane shape is 2.25.

For purposes of computation it will be assumed that the vane at the elbow centerline will be most susceptible to cavitation as this is the region of highest velocity. Furthermore to evaluate an extreme condition, the pressure at the top of the test section will be taken as the vapor pressure.

By writing the Bernoulli equation along the centerline streamline of the test section and the first elbow, the following expression is obtained for the datum plane at the elbow:

$$\frac{P_T}{\gamma} + \frac{V_T^2}{2g} + z_T = \frac{P_o}{\gamma} + \frac{V_o^2}{2g} + K\frac{V_T^2}{2g} \qquad (7)$$

where $P_T = P_v/\gamma + h$

P_v = vapor pressure

h = depth at mid-section, 5 ft

V_T = test section velocity

z_T = vertical distance between centerlines, 3.83 ft

P_o = pressure at elbow

V_o = maximum velocity at elbow = $C\bar{V}_o = C(A_T/A_o)V_T$

K = diffuser loss coefficient

Rewriting this expression in the form of a local cavitation number at the elbow entrance plane with a ratio of test section to elbow area, A_T/A_o, of 0.32 gives

$$\sigma_{min} = \frac{P_o - P_v/\gamma}{V_o^2/2g} = \frac{86.26}{C^2 V_T^2/2g} + \frac{9.766}{C^2}\left[1 - K\right] - 1 \qquad (8)$$

Using different values of the ratio of maximum to average velocity, C, and diffuser loss coefficients with a maximum test section velocity of 50 fps, the values of σ_{min} have been calculated and are listed in the following table.

TABLE 1

	K = 0.12	K = 0.14	K = 0.16	K = 0.18	K = 0.20
C	σ_{min}	σ_{min}	σ_{min}	σ_{min}	σ_{min}
1.4	4.52	4.42	4.32	4.22	4.12
1.5	3.81	3.72	3.63	3.55	3.46
1.6	3.23	3.15	3.07	3.00	2.92
1.7	2.74	2.68	2.61	2.54	2.47
1.8	2.34	2.28	2.22	2.16	2.10
1.9	2.00	1.94	1.89	1.83	1.78
2.0	1.70	1.66	1.61	1.56	1.51

For the vane to be cavitation free, σ_{min} should be greater than 2.25. Experimental measurements of the diffuser exit velocity profile have indicated that $C \sim 1.7$. Thus, for all the diffuser loss coefficients, σ_{min} exceeds 2.25 but without much margin. With an additional 2 ft of head added at the

test section, i.e., h = 7.0 ft, the values of σ_{min} for C = 1.7 range from 2.92 to 2.65 for K = 0.12 and 0.20, respectively. In view of the fact that the above computations were based on steady flow values with a bare tunnel, it would be desirable to have a greater safety margin than the computations indicate. This may require a change in the vane profile to attain a less peaky pressure distribution.

III. WATER QUALITY AND CAVITATION TESTING

A. Introduction

Cavitation is a design consideration for a broad variety of devices handling liquids. Cavitation can affect performance, for example through increased drag of hydronautical vehicles, limitations on the thrust produced by various propulsion systems, decreased power output and efficiency of turbines, and a drop in head and efficiency produced by pumps. The accuracy of flow meters can be affected by cavitation. Noise and vibration occur in many applications, ranging from all forms of turbomachinery to large valves in industrial plants. Associated with the deleterious effects of performance breakdown, noise, and vibration, there is the possibility of erosion. Erosion can range in extent from a relatively minor amount of pitting after many years of operation to disastrous failure of large and expensive structures in a relatively short period of time.

There is a vast quantity of cavitation literature on topics ranging from basic mechanics to practical application. Several excellent reviews already exist [6, 7, 8]. There is one textbook in English [9], a few more textbooks in foreign languages (e.g. Karelin [10]) and a brief monograph [11]. Various aspects of the problem have been considered in the Annual Reviews of Fluids Mechanics [12, 13, 14]. Related phenomena have also been addressed [15, 16, 17, 18]. Several major symposia have been devoted to the topic [19, 20, 21, 22, 23, 24, 25, 26, 27, 28], not to mention the Annual Forum on Cavitation and Polyphase Flow held by the American Society of Mechanical Engineers, the periodic review of the topic in the Proceedings of the International Towing Tank Conference, and

other symposia devoted to hydraulic machinery, marine propulsion, naval hydrodynamics, etc.

From an engineering-design point of view there are two basic questions. First, will cavitation occur? Second, if cavitation is unavoidable, then the question is whether a given design can still function properly. Often economic or other operational considerations necessitate operation with some cavitation. Under these conditions it is necessary to understand the effects of cavitation on steady loading as well as any unsteady forces that may be induced.

Practical experience indicates that we must rely heavily on experimentation in the development of marine devices. In order to reliably predict cavitation inception or performance in cavitating flow in the laboratory, it is essential that the physics of the phenomenon be cleasrly understood so that proper modeling techniques are applied. In addition, estimates of operational lifetime and maintenance must rely on erosion tests carried out in the laboratory.

B. Occurrence of Cavitation

Cavitation is normally defined as the formation of the vapor phase in a liquid. The term cavitation (originally coined by R. E. Froude) can imply anything from the initial formation of bubbles (inception) to large-scale, attached cavities (supercavitation). The formation of individual bubbles and subsequent development of attached cavities, bubble clouds, etc., is directly related to reductions in pressure to some critical value, which in turn is associated with dynamical effects, either in a flowing liquid or in an acoustical field. Cavitation is distinguished from boiling in the sense that the former is induced by the lowering of hydrodynamic pressure, whereas the latter is induced by the raising of vapor pressure to some value in excess of the hydrodynamic pressure. The two phenomena are related. Cavitation inception

and boiling can be compared in terms of the vapor-bubble dynamics of sub-cooled and super-heated liquids [29]. Quite often a clear distinction between the two types of phenomena cannot be made. This is especially true for cavitation in liquids other than cold water.

Examples of cavitation can be found in the literature. More than one type of cavitation can occur simultaneously (e.g. sheet cavitation on the blade, vortex cavitation at the tips). It is also important to note that in many practical applications cavitation is a nonsteady phenomenon. In the classical propeller problem, the nonsteadiness is induced by periodic passage of each propeller blade through the ship's wake.

C. Cavitation Scaling

The fundamental parameter in the description of cavitation is the cavitation index

$$\sigma = \frac{p_o - p_v}{\frac{1}{2}\rho U_o^2} \tag{9}$$

wherein p_o and U_o are a characteristic pressure and velocity, respectively, ρ is the density, and p_v is the vapor pressure of liquid. Various hydrodynamic parameters such as lift and drag coefficient, torque coefficient, and efficiency, are assumed to be unique functions of σ when there is correct geometric similitude between the model and prototype. Generally speaking, these parameters are independent of σ above a critical value. This critical value is often referred to as the incipient cavitation number. It should be emphasized, however, that the point where there is a measurable difference in the performance is not the same value of σ where cavitation can first be detected visually or acoustically.

There are two ways of defining the critical value of σ. σ_i is defined as the incipient cavitation number, which is normally determined in a water tunnel at constant velocity by slowly lowering the test-section pressure until cavitation is first observed. A more repeatable quantity is the desinent cavitation index, σ_d, which is usually determined at constant speed in a water tunnel by first lowering the pressure until cavitation occurs and then slowly raising the pressure until the cavitation is extinguished. In order to eliminate confusion, the term σ_c will be used to imply a critical value throughout the rest of this report. σ_c can be thought of as a performance boundary such that

$\sigma > \sigma_c$ no cavitation effects,

$\sigma < \sigma_c$ cavitation effects: performance degradation, noise, and vibration.

In scaling cavitation inception (or desinence), it is assumed that cavitation occurs when the minimum pressure in the flow is equal to the vapor pressure. For steady flow over a streamlined body this implies

$$\sigma_c = - C_{pm} \tag{10}$$

where C_{pm} is the minimum pressure coefficient. In the case of a hydrofoil or a strut, C_{pm} is a function of angle of attack, α, as well as the shape of the body. The equivalent parameter for a turbomachine would be the normalized flow rate, Q/nD^3. In the case of a propeller, the effective parameter is the advance coefficient, $J = U/nD$. Hence, for fixed geometry

$$\sigma_c = f \begin{cases} \alpha & \text{- hydrofoils, struts} \\ Q/nD^3 & \text{- pumps and turbines} \\ U/nD & \text{- propellers} \end{cases} \tag{11}$$

Inception on hydrofoils has been studied by numerous investigators [30, 31, 32]. Much of this work is summarized in Knapp et al [9]. Typical data for a hydrofoil are reported by Kermeen [30]. Hydrofoil data of the type found in this paper can be used to predict the cavitating performance of a propeller [33].

Cavitation has an influence not only on steady-state phenomena but on nonsteady phenomena as well. An example is the work of Young and Holl [34]. They found a dependence of the frequency of vortex shedding behind wedges on the cavitation index. It should also be pointed out at this juncture that developed cavitation is basically a nonsteady phenomenon even though the external flow is steady. Clear, glassy cavitation can be observed attached to bodies, hydrofoils, etc. However, examination of these cavities with high-speed cinematography indicates that, under certain condition, the process is periodic. The frequency of the process is quite sensitive to the headform shape. This question is discussed in detail by several authors [7, 30, 31, 35, 36, 37].

The suitability of the cavitation index, σ, is dependent on the assumption of an inviscid fluid (i.e. pressure scaling with velocity squared), and the assumption that cavitation occurs when the minimum pressure in a given flow field is equal to the vapor pressure at the bulk temperature. It is further assumed, in the case of developed cavitation, that the cavity pressure is equal to the vapor pressure. With these assumptions in mind, σ is the primary scaling parameter for inception and is the primary independent variable for scaling all hydrodynamic parameters involving cavitating flow.

It is imperative to understand the limitations of the basic scaling law since much of the information about the effects of cavitation are deduced experimentally. The question of cavitation scale effects has been considered by many authors in the past (38, 39, 40, 41]. Unfortunately, most of the

experimental evidence is based on laboratory data obtained over a limited range of independent variables. There is little information available on the correlation between model and full scale. Since much of the developmental work in marine engineering is based on considerable testing, usually in a laboratory, it is necessary to establish accurate modeling or scaling laws in order to be able to extrapolate model data to field or service conditions with confidence.

For the case of streamlined bodies, reasonable correlation with Reynolds number is achieved, but a definite size effect is still apparent. Holl and Robertson [42] provided some convincing evidence that Weber number was also a significant parameter. This is in keeping with the unique measurements of Kermeen et al. [38] who found that the flow was in tension in the minimum pressure region of a streamlined body when cavitation was incipient.

Another type of scale effect was found by Holl [43]. Two types of cavitation are noted on the same NACA 16012 hydrofoil section. One set of data corresponds to a band type of cavitation that disappears uniformly across the span when $\sigma = \sigma_c$. A second type, consisting of random spots, has a much higher value of cavitation index at desinance. The first type follows the typical trend observed for streamlined bodies. The latter type shows a decrease in σ_c with an increase in velocity, and σ_c is higher than the predicted value (Eq. 10). In his analysis, Holl [43] conjectured that the former type was true vaporous cavitation, whereas the latter type of cavitation was dominated by the effects of gaseous diffusion. This type of bubble growth is not unlike the bubble formation that occurs when the pressure in a bottle of champagne is suddenly reduced when the cork is popped. This type of cavitation follows a different scaling law (compare with Eq. 10):

$$\sigma_c = - C_{pm} + \frac{p_g}{\frac{1}{2} \rho U_o^2} \tag{12}$$

where p_g is the saturation pressure at a given gas content.

The foregoing examples illustrate that cavitation inception (or desinence) is not adequately described by a single parameter such as σ. There are many reasons for the discrepancies noted. Fundamentally these fall into two categories:

1. The pressure field is not adequately described by an ideal-fluid-flow model; the effects of turbulence and other viscous phenomena dominate the problem.
2. The critical pressure at inception is not the vapor pressure and can be either higher or lower than p_v depending on the situation. Ordinary liquids can sustain tension and more than one type of cavitation process can occur in the same flow field. Bubble growth can be a result of the formation of the vapor phase, or be due to the release of dissolved gas, or can be some combination thereof. It is not always possible to clearly distinguish between vaporous and so-called gaseous cavitation.

D. Cavitation Nuclei

It is generally accepted that cavitation inception occurs as a consequence of the rapid or explosive growth of small bubbles or nuclei that have become unstable due to a change in ambient pressure. These nuclei can be either imbedded in the flow or find their origins in small cracks or crevices at the boundary surface of the flow [44, 45, 46, 47, 48]. The details of how these nuclei exist have been considered by many investigators. A coherent summary of this work is offered by Holl [49, 50].

Most of the progress in understanding the details of the inception process has been made through the consideration of the dynamic equilibrium of a spherical bubble containing vapor and non-condensible gas. The Rayleigh-Plesset equation describes this equilibrium [14]:

$$R\ddot{R} + \frac{3}{2}\dot{R}^2 = \frac{1}{\rho}\left[p_i - p_\infty(t) - \frac{2S}{R} - 4\mu\frac{\dot{R}}{R}\right] \tag{13}$$

wherein R is the bubble radius, p_i theinternal pressure, S the surface tension, μ the dynamic viscosity, and ρ the liquid density. Dots denote differentiation with respect to time. Neglecting the dynamical terms in Equation (13) results in

$$p_i - p_\infty = \frac{2S}{R_c} \quad , \tag{14}$$

R_c being an equilibrium radius.

Consider first a nucleus in the form of a small spherical bubble containing incondensible gas in a saturated solution. As shown by Epstein and Plesset [51], Eq. 13 represents an unstable equilibrium. A slight reduction in R_c increases p_i and drives gas into solution resulting in a further reduction in size. Similarly, a slight increase in R_c decreases p_i and the bubble grows by diffusion of gas across the bubble wall. The postulate of Harvey et al. [52, 53, 54] circumvents this problem, as illustrated in Fig. 6. If a solid particle containing a fissure, as shown, is hydrophobic, then the gas-liquid interface is concave and the stability equation is now

$$p_\infty - p_i = \frac{2S}{R_c} \tag{15}$$

which represents a stable equilibrium. The argument against small gas bubbles

as nuclei is only valid in a static environment. Ripken and Killen [55] discuss the source of nuclei and point out that in the turbulent flow of a water tunnel, gas bubbles can be a source of nuclei. Presumably the bubbles are stabilized by rectified diffusion due to turbulent pressure fluctuations. Arndt and Keller [56] measured the nuclei in a large water tunnel and in a depressurized towing tank using a laser scattering technique. They concluded that the only source of nuclei in the towing tank was in the form of suspended solid material, whereas both solid particles and gas bubbles were sources of nuclei in the water tunnel. Gates and Acosta [57] report considerable differences in the makeup of the nuclei population in two different tunnels (one having essentially small particles, the other essentially micro-bubbles). There is generally some relationship between the number density of nuclei and the level of dissolved gas in a given test facility. This relationship is not unique and depends on several factors including the facility configuration and operating conditions [55, 56, 58]. However, recent work by Arndt, Taghavi, and Barrel (unpublished) and Barrel [59] indicate that there is a subtle, albeit definitive relationship between the level of dissolved gas and the nuclei population in a given facility. In fact, the possibility exists that a given facility could be calibrated for nuclei size distribution as a function of dissolved gas, allowing rather simple monitoring of the nuclei content via the measurement of dissolved gas via the van Slyke meter or gas chromatograph. The essence of this argument is illustrated in Figs. 7 and 8. Figure 7 is a plot of number density versus nuclei size. Nuclei number density $n'(R)$ is defined such that the total number of nuclei per unit volume, n, is given by

$$n = \int_0^\infty n'(R)dR \tag{16}$$

In this figure, which contains measurements made in several different facilities, it is readily noted that the shape of the nuclei size spectra are approximately the same. On a log-log plot the spectra can be approximated by a straight line which shifts up or down as a function of the level of dissolved gas. As an example, attention is drawn to the data of Arndt and Keller [56] collected in a relatively large water tunnel (1 m by 1 m test section) and the data of Ooi [60] which was collected in a much smaller water tunnel at the California Institute of Technology. These data are replotted in Fig. 8, as total nuclei density versus total air content. The agreement between the two sets of data is remarkable. However, other facilities display different characteristics as shown by the data of Oba et al. (61] and Keller and Weitendorf [58]. This possibility should be explored further.

The general influence of nuclei size on the critical pressure can be deduced from Eq. 14, assuming p_i to be made up of vapor and non-condensible gas that is free to expand or contract isothermally

$$p_i = p_v + \frac{Nk\theta}{\frac{4}{3}\pi R^3} \quad , \tag{17}$$

N being the total mass of the gas in the bubble, k the universal gas constant, and θ the temperature. There is a critical value of $p_v - p_\infty$ below which static equilibrium is not possible [62]

$$(p_v - p_\infty)_{cr} = \frac{4S}{3R_*} \tag{18}$$

wherein R_* is the critical radius which is related to the amount of gas in the bubble

$$R_* = \left[\frac{9}{8\pi}\frac{Nk\theta}{S}\right]^{1/2} \quad . \tag{19}$$

Equation 18 implies that the basic cavitation scaling law should be modified to read

$$\sigma_c = \left[C_{pm} + \frac{\frac{4}{3}\,S/R_*}{\frac{1}{2}\,\rho U^2}\right] \quad . \tag{20}$$

Measured nuclei size distribution are shown in Fig. 7. The data are for two water tunnels whose nuclei are mostly micro-bubbles and for two other facilities (a water tunnel and a depressurized towing tank) whose nuclei consist mostly of solid particles [56, 57]. As already mentioned, the data indicate that nuclei population that are dominated by micro-bubbles are sensitive to the relative saturation level of dissolved gas.

The data in Fig. 7 also indicate that a reasonable number of larger bubbles exist in most facilities (corresponding to tensions of less than .50 mb). However, there is evidence that the flow field around a given body produces a screening effect such that larger bubbles tend to move out of the critical-pressure region leaving only smaller bubbles with more negative critical pressures to be active in the cavitation process [63]. Very little has been done to investigate the question of the influence of nuclei size distribution on cavitation. What information we do have does indicate that this can be an important factor in laboratory experiments [57, 64, 65]. Most of the theoretical work on the influence of nuclei on cavitation assumes that the bubbles are always in static equilibrium until a critical size is reached and then explosive growth occurs. If the exposure time to negative pressure is

short (less than the natural period of the bubble), then much greater tensions than predicted by an equilibrium model are possible [38, 40, 65, 66]. A universal relationship is not available, but the amount of tension will vary inversely with a characteristic time scale of the flow

$$(p_v - P_\infty)_{cr} = \frac{4S}{3R_*} f\left[\frac{d}{U}\left(\frac{S}{\rho R_*^3}\right)^{1/2}\right] \tag{21}$$

where f is an unknown function which tends to unity for large values of its argument.

The question of an adequate distribution of nuclei in a test facility can be important for modeling developed cavitation as well as determining cavitation-inception limits. This is especially true for unsteady cavitation (e.g. vibration due to cavitation on a propeller operating in a nonuniform inflow [58, 67]).

Techniques for the measurement of cavitation nuclei have been developed over only the past 20 years [55, 57, 64, 68, 69, 70, 71, 72]. It is only recently that reliable measurements are possible, and it is anticipated that more information on this important topic will be made available shortly.

E. Other Influences of Dissolved Gas

The influence of free and dissolved gas on cavitation inception has already been alluded to. However, the fact that dissolved gas can influence hydrodynamic loads in cavitating flows is not given much consideration in the literature. For example, Edstrand [73] found that measured thrust and torque on a model propeller could vary by a factor of two with varying amounts of dissolved gas with σ held constant. Measurements on a model hydrofoil differed from the expected value by as much as 20 percent [74]. The discrepancy

was traced to the influence of dissolved gas. Wade and Acosta [75] measured the cavity pressure on a hydrofoil with developed sheet cavitation and found that there were substantial differences between σ defined by the measured cavity pressure and that defined in the usual manner using the vapor pressure. This is in agreement with previous measurements by Kermeen [30]. This could account for a difference of 10 percent in the measured lift coefficient if completely degassed water were used in place of the saturated water used in the experiments.

A systematic investigation of gas-content effects on cavitation inception in free-shear flow was recently reported by Baker et al. [76]. Cavitation inception in confined jets, generated either by an orifice plate or a nozzle, was determined as a function of total gas content in the liquid. When the liquid was undersaturated at test-section pressure, the critical cavitation index was independent of gas content and roughly equal to that observed by Rouse [77] for an unconfined jet. When the flow is supersaturated, the cavitation index is found to vary linearly with gas content as predicted by the equilibrium theory, Eq. 12. This effect occurs even though the Lagrangian time scale of the turbulence is much shorter than typical times for bubble growth by gaseous diffusion. For example, in the cited cavitation data, a typical residence time for a nucleus within a large eddy is roughly 1/15 of a second. At a gas content of 7 ppm and a jet velocity of approximately 10 m/s, inception occurs at a mean pressure equivalent to a relative saturation level of 1.25. Epstein and Plesset [51] show that for growth by gaseous diffusion alone, 567 seconds is required for a 10^{-3} cm nucleus to increase its size by a factor of 10. However, the local pressure within an eddy is much less than the mean pressure, and highly supersaturated conditions can occur locally. Arndt and Keller [56] also reported large gas-content effects in their experiments with disks when the flow

was supersaturated. The magnitude of the effect also depends on the number of nuclei in the flow. Gas-content effects on cavitation inception and desinence were noted only in their water-tunnel experiments (where there is a healthy supply of nuclei). No gas-content effects on inception were noted in a depressurized tow tank (where the flow is highly supersaturated but there is a dearth of nuclei). Thus the picture becomes cloudier as the influence of dissolved, non-condensible gas is taken into consideration.

F. Deaeration/Aeration

From the above discussion it is evident that testing of hydrodynamical forms or devices in a water tunnel requires careful control of nuclei in the water as well as control and measurement of the dissolved gas. The free gas content (the nuclei) and the dissolved gas content are interrelated in a complex manner that is generally unique to a given facility. All this suggests the desirability of a convenient and reliable means of control and measurement of the free air content of the test water. Unfortunately no single method acceptable to most experimenters exists for either measurement or control of free air content, although this particular aspect of experimental research has been extensively discussed in the recent literature. Fortunately, standard methods do exist for both the measurement and control of air in solution, although they are costly and cumbercome.

The most common procedure for air content control of a small water tunnel is to operate the tunnel through a pressure history which will give a desired value of air in solution, and hopefully an equilibrium of free air with air in solution will result. This becomes a costly and an unreliable procedure for larger water tunnels, if for no other reason than the time to reach an equilibrium becomes excessively long. Auxiliary devices external to the tunnel

flow circuit have been added to large water tunnels which adjust the air in solution. Resorbers have also been added to the flow circuit to provide a counter positive pressure history to the negative pressure history in the test section [78]. The desired effect of the two extremes of pressure in the test loop is to achieve an equilibrium of the air content.

More recently the procedure used for nuclei control is to reduce the free air in the water tunnel circuit as much as possible and to then supply the nuclei upstream of the test section before the contraction or immediately upstream of the test object. The use of a nuclei generator upstream of the test body introduces excessive turbulence into a low turbulence water tunnel, so that the specification on turbulence in this case cannot be met.

The recommendation is that an auxiliary device of the packed column design, similar to that employed on the present DTNSRDC 36-inch water tunnel, be utilized. The capacity shall be sufficient to reduce the air in solution to one tenth of the saturation value in eight hours. The seeding of critical regions with nuclei shall be the responsibility of the experimenter at the time of experimental design, who at the same time shall make the necessary compromises in turbulence level. It is suggested that the introduction of air be by means of a manifold near the upper end of the "downcomer." Axial flow pumps are minimally affected by air in suspension. The auxiliary air saturation control system shall be reversible so that the air in solution can be increased without introducing free air. The use of independent methods of control of free air and air in solution might produce equilibrium operation between free air and air in solution under some test conditions. The techniques of injecting saturated water is discussed by Albrecht et al. [79].

Control of bubble size would be possible only when air is introduced by the experimenter immediately upstream of the test body. When the tunnel is operated

with an equilibrium between the air in solution and in suspension, the maximum stable bubble size is determined by the maximum kinetic energy dissipation the bubbles experience in the flow circuit. The minimum size is determined by a yet undiscovered stabilizing mechanism.

Cavitation is a function of vapor pressure, free gas, dissolved gas, and the standard hydrodynamic parameters which for most purposes reduce to Reynolds scaling. With this in mind, control of temperature is not only necessary, but the capability to vary temperature provides an attractive means for increasing the range of capabilities of the facility. Using temperature to increase vapor pressure, and hence reduce the cavitation number at a given speed, was first used by Parsons in 1897 to study propeller problems in a small water tunnel of his own design and construction. Little has been reported about this technique since that time. However, modern facilities have been provided with temperature control, such as the Garfield Thomas Water Tunnel. The attractiveness of temperature control probably lies in the possible variation in Reynolds number at constant speed. The kinematic viscosity of water varies from 1.67×10^{-5} ft^2/sec at 40°F to 0.74×10^{-5} ft^2/sec at 100°F. In other words, Reynolds number can be varied by a factor of 2.5 simply by temperature control. Surface tension is only slightly affected by temperature, but solubility of gases is strongly dependent on temperature. Thermodynamic effects on cavitation inception are probably not important in water at temperatures below 120°F [18]. However, the uncertainties related to solubility and nuclei content indicate that variations in temperature should be only carried out after careful study. In any event, the capability to vary temperature should be limited to the range 40°F to 105°F. This requirement is different from the requirement to remove the heat generated by the frictional resistance to water flow at full load.

The time required for removal of air in solution depends on the design speed of the auxiliary air removal system, which according to specification is from saturation to one-tenth saturation in eight hours. Air can be added much more quickly through a manifold in the "downcomer." One-hundred (100) cubic meters of air at atmosphere pressure are required to saturate the water in the water tunnel if the starting point is one tenth saturation. The water pressure increases to almost two atmospheres in the lower leg of the water tunnel. The very powerful mixing action of the pump impeller would be expected to drive the air into solution as quickly as it is introduced, as inferred from absorber studies.

IV. ALTERNATE TEST SECTIONS

It has been requested that the possibility of alternate test sections be considered for the LCC. These alternate test sections should fit within the general overall layout of the flow circuit with a minimum of component revision. The baseline design of the LCC includes a closed test section 10x10x40 ft with a maximum speed of 30 knots, and very demanding performance goals have been imposed both with regard to flow quality and noise levels. Any modification to the baseline design necessary to accommodate alternate test sections must not result in a compromise of these established goals. Furthermore, the performance goals are no longer considered applicable for any alternate test section, as special design features are required in an attempt to meet the goals for the baseline design.

The alternate test section design parameters have been given as:

a)	Low speed free surface	0 to 30 knots
b)	High speed free surface	0 to 60 knots design goal
	Test section size	2x2x12 m design goal
		1x1x1 m minimum requirement

Concepts for alternate test sections along these guidelines will be discussed in the following section.

A. Low Speed Free Surface

In the consideration of this test section, the flow has been divided into categories of subcritical and supercritical flow when the depth Froude number is

less or greater than one. The maximum Froude number for subcritical flow that can effectively be utilized is assumed to be about 0.8. For open channel flow, as the Froude number approaches unity, the water surface becomes undulated and therefore considered unacceptable in a test facility.

The simplest way to generate a subcritical flow would be to lower the water level in the channel so that a free surface is present. If a water depth in the test section of 6 ft is desired, the maximum flow velocity for a Froude number of 0.8 is about 11 fps. The flow rate for the 10 ft width is 660 cfs. The head delivered by the pump is determined by the headloss in the flow circuit, which is usually expressed as a fraction of the test section velocity head. For this rather rough calculation, a loss coefficient of 0.3 will be used resulting in a pump head of 0.56 ft. Using the typical dimensionless head-discharge curve (Fig. 9) for an axial flow pump proposed by Etter and Altmann [80], a fixed blade pump with blade angle of 20°, and a pump diameter of 20 ft, the pump would have to be operated at about 13 rpm to achieve these conditions. To operate at the same flow depth but lower Froude number, the rotational speed varies directly with Froude number.

Model studies are required to determine the feasibility of this scheme. Such model studies can be readily carried out in the proposed 1 to 5 scale model of the complete flow circuit of the LCC, as no significant physical changes are anticipated.

An innovative scheme for a supercritical flow test section has been proposed by Etter [81]. A sketch adapted from their report is shown in Fig. 10. Supercritical flow is generated by a sluice gate at the entrance to the test section. An insert placed on the flow of the test section with a height equal to the flow depth is used to control the location of the hydraulic jump. A different insert is required for each flow depth or Froude number. The

advantage of this scheme is that very little modifiction to the main flow circuit is required.

As a hydraulic jump is basically an unsteady flow phenomena, it was uncertain whether the location of the jump could be fixed by the floor insert. To qualitatively evaluate the overall flow performance, a small model with a scale of 1 to 20 was set up in one of the Laboratory's recirculating open channels. The model included the sluice gate, test section, and diffuser, and as these components are symmetrical in planform, the model was confined to half the planform width. A photo of the model in operation with a Froude number of four is shown in Fig. 11. The flow is from right to left, with the sluice gate and floor insert at the right side of the photo. The vertical line near the lower center represents the end of the 40 ft long test section, and the entrance to the diffuser. Of primary interest was the action of the hydraulic jump. The intense roller and aeration can clearly be seen. A large number of bubbles are carried downstream into the diffuser. Many of these bubbles rose to the top of the diffuser along its length. It should be noted that such air entrainment cannot be modeled accurately, and it is expected that in the full scale diffuser, more bubbles will be carried downstream than in the model. The toe of the hydraulic jump moved up and downstream over a period of time, and in some cases encroached on the test section region above the floor insert. It was difficult to obtain a stable flow, and if the conjugate depth was set at the height of the diffuser opening, any slight undulation of the water surface caused the jump to move forward.

The hydraulic jump in the test section is rather violent even at the small scale utilized here. An extensive study of the hydraulic jump and associated boundary pressures has been carried out at the Laboratory [82]. It was found that the maximum value of the rms pressure fluctuations on the bottom were about

5 percent of the inflowing kinetic energy. Extreme values about the mean were about three times the rms value. The location of this maximum was about midway under the surface roller, and the test section floor must be designed to resist these pressures.

The model does not completely represent the flow circuit of the LCC, in that depth was controlled with a tailgate. Initially, supercritical flow was established in the test section, and the tailgate then adjusted so that the conjugate depth was about the diffuser height. It is expected that in the full scale flow circuit, the test section would initially be flooded, and the volume of water eventually would be removed or stored in a separate tank during free surface operation. This is basically the manner in which the SAF high speed free surface water tunnel is operated. The starting water level was found to be critical in the establishment of a stable free surface flow.

Although this scheme to generate supercritical flows in the test section requires relatively moderate modification, the actual usefulness is questioned. The flow range and length and depth of test section are quite limited. The small scale model studies indicated that rather large quantities of air may be ingested in the diffuser. A large percentage of this air must be removed somewhere in the flow circuit to prevent flow instability and to increase the length of time available for a test run. A more complete evaluation of the scheme can be carried out in the 1 to 5 scale model of the entire flow circuit if interests warrant.

B. High Speed Free Surface

The performance goals for this alternate test section include a top speed capability of 60 knots with the size of the test section reduced to 2x2 m or a minimum requirement of 1x1 m. The Laboratory has previously been involved in

the design of a free surface water tunnel with a 3 ft x 3 ft test section and top speed of 60 knots [83]. During that design and consequent model studies, one of the predominating concerns was air removal from the system. The final design incorporated a very large air separator upstream of the test section. Such a design is not economically feasible for the LCC. However, possible modifications that would restrict the overall performance have been briefly examined.

Several items deserve attention in the discussion of these alternate test sections. Reducing the test section area requires an addition of some type of modified nozzle, which can either replace part of the K&R contraction or be added downstream of it. The latter option reduces the length available for the actual test section. Furthermore, the reduced test section area results in more severe demands on the diffuser, as the area ratio has been increased. This is particularly true if it is assumed that size of the first elbow has not been changed. The turning vane design will be dictated by the baseline design, and the alternate test sections should not compromise that design. Due to the increased area ratio, the diffuser losses will be higher, and care must be taken to prevent separation and flow instability.

As previously mentioned, air entrainment and its removal is a problem in a free surface facility. Some type of skimmer is required to insure a smooth flow into the diffuser to provide flow stability. The skimmer is usually designed to remove about the top 5 percent of the flow, although early tests at the Laboratory have indicated that 2 percent may be adequate. However, it must be pointed out that a skimmer will not remove all of the air being entrained in the test section. Without an additional air separator, the air concentration will increase with running time. Some air may be collected in domes at low velocity regions of the test loop and be bled back to the test section, although not all

entrained air is expected to be removed. The continued increase of air concentration will eventually require that a test run be terminated and the tunnel deaerated. It also has been demonstrated that large air pockets in the test loop can introduce undesirable elasticity in the flow circuit with resulting unstable flow in the test section.

To establish some reference values, assume that the maximum available shaft power is 15,000 HP. This power is directly proportional to the head, H, and discharge, Q. Since H is equal to a tunnel loss coefficient, K_T, expressed in terms of the test section velocity head, and Q is the product of the test section area and velocity, the velocity and area can be calculated for various K_T within the restraint of available power. Such a plot is shown in Fig. 12 with an assumed efficiency of 80 percent. It can be seen that to attain 100 fps in a 2x2 m test section (A = 43 ft^2) the loss coefficient should not be greater than 0.15. Estimates of K_T with a bare tunnel gave a value of about 0.21 which exceeds the allowable value. The diffuser contributes to much of the loss. With K_T of 0.25, the maximum velocity is about 85 fps.

At this point, a test section with a 2x3 m cross-section (A = 65 ft^2) will be discussed. Estimates of K_T of about 0.164 have been made for a bare tunnel, and with an increase of about 20 percent for a test body, a value of 0.2 may be assumed. This results in a maximum test section velocity of about 80 fps. The maximum discharge of 5164 cfs exceeds the baseline discharge of 5000 cfs, but this should not be of concern.

This size of cross section has some advantages in that the width does not have to be modified. The contraction design may be relatively simpler, and the demand on the downstream diffuser is not as great. However, the skimmer must extend the full width of the test section, and the quantity of skimmed flow is greater than for a reduced width. From previous tests at the Laboratory with

free surface test sections, it is known that the free surface is not flat across the entire test section width due to effects of the side walls. These effects become more predominate as the length of the test section increases. Using the wider test section should enhance the possibility of attaining a smooth, flat free surface.

A sketch of a tentative layout for such a section is shown in Fig. 13. The free surface is generated by a contraction on the top surface. Using a shape similar to that previously used at the Laboratory, the length is about 11.5 ft and the opening height at the entrance to the test section is about 7.8 ft. Final contraction of the free surface occurs in the test section and requires about 13 ft. The top surface element can either be applied as an insert or a separate nozzle can be fabricated and installed at a breakplane at that location. In any case, the existing corner fillet of the K&R contraction would have to be matched and reduced to zero at the exit of the top surface.

A skimmer design similar to that previously used [83] is contemplated. This may be about 12 ft long, and it is proposed to install the unit at the location shown. The resulting length of test section is therefore about 14 ft. A breakplane is shown at the end of the second transition of the main K&R diffuser. A new insert would be installed from the skimmer lip to the top of the diffuser. The length of the insert is the minimum that can be considered. Again, fillet modifications are required over this length. The emphasis here has been placed on removing as little of the main diffuser as possible. Model studies are definitely required to establish the performance of this diffuser to determine possibilities of flow separation and cavitation in the vicinity of the skimmer lip where the pressures are the lowest. Previous tests have shown this to be a critical area, and careful design of the transition is required. The effects of the additional diffuser on the exit velocity profiles and flow

stability of the main diffuser must be evaluated. This can be done in the 1 to 5 scale model of the entire flow circuit, or in the existing 1 to 10 scale wind tunnel.

The skimmed flow must be deaerated and returned to the loop. Although it may be possible to inject this flow at the boundary of the diffuser and thereby reenergize the boundary layer, this was considered in the existing Laboratory design but was not implemented. Rather, the flow was reintroduced immediately downstream of the first elbow. Assuming a pressure rise of 0.5 times the test section velocity head between the test section and that point, the power required to inject a flow rate of 250 cfs is about 1800 HP.

Using the hypothetical pump curve of Fig. 9, for H = 19.8 ft, Q = 5150 cfs, and D = 20 ft, $\sqrt{K_H}/K_Q = 0.346$. If the blade angle is assumed to be 20 degrees, the flow coefficient K_Q is 0.0075. The pump rpm is then about 86 rpm, and the efficiency is just a small percentage from the maximum value.

V. ESTIMATE OF HEADLOSSES

An estimate of headlosses in individual components has been made based on the preliminary K&R design. This estimate is for the closed test section with dimensions of 10x10x40 ft, and the loss coefficients are listed in Table II. Here K_C refers to the loss coefficient for the component referred to the local inlet velocity head, and K_T is the loss coefficient referred to the test section velocity head. The two are related by the ratio of the squares of the test section to component area.

TABLE II

Summary of Loss Coefficients

Bare Tunnel

Component	K_C	K_T
Test Section	0.04	0.04
Main Diffuser	0.12	0.12
1st Elbow	0.25	0.0257
Shape Transition	0.021	0.0022
2nd Elbow	0.25	0.0260
Lower Leg Diffuser	0.06	0.0062
55 ft Pipe	0.04	0.0011
Shape Transition	0.02	0.0006
3rd Elbow	0.25	0.0071
4th Elbow	0.25	0.0071
Honeycomb	0.20	0.0057
Contaction	1.02	0.029
		$\sum K_T = 0.2707$

where $K_T = \frac{H_L}{V_T^2/2g}$ $K = \frac{h_\ell}{V_C^2/2g}$

For a test section velocity of 50 fps, the pump head of the bare tunnel is about 10.5 ft. This value should be increased to account for the drag of a body in the test section. The test section loss coefficient is assumed to increase by 50 percent due to presence of a test body. It is unknown what the effect the body has on the diffuser. The loss may increase or decrease, but for the present purposes, it will be assumed that losses may increase by 50 percent. Therefore, the pump head increases to 13.6 ft for the design velocity of 50 fps.

The above loss coefficients do not include interaction effects between components. These effects can be considerable, and may be adverse or favorable, depending on the flow conditions. A better determination of loss coefficients requires measurement of inlet and exit velocity profiles for each component in the complete flow circuit, in addition to pressure drops across the component. In this manner, the actual rather than the average kinetic energy can be incorporated. Such determination can be carried out in the 1 to 5 scale model of the LCC.

VI. CONCLUSIONS

1. The preliminary K&R contraction design should provide mean velocity profiles in the test section within the specified plus or minus one percent, excluding boundary layer regions. The possibility of flow separation at the contraction inlet has led to consideration of two alternate boundary shapes, maintaining the original contraction ratio of about six. These shapes were evaluated using both a three-dimensional and an axisymmetric mathematical model. One shape was a modification of the K&R design using the same equation with the contraction length increased by 2 meters. The other shape was a matched cubic similar to that previously used in axisymmetric contraction design. The length of the contraction was increased to 13 meters. The maximum pressure coefficient near the inlet was reduced for both shapes, thereby reducing the possibility of flow separation. Increased length may be desirable for turbulence management systems. The optimum shape for the contraction has not been finalized. Other shapes could be investigated using the mathematical model developed in Task B.

2. The two part diffuser transition of the K&R design could possibly be shortened. The original transition curve is a quartic, and a cubic curve is proposed as a modification. The resulting transition is about 2.7 meters shorter, and this length could effectively be used upstream of the contraction, thereby retaining the overall length of the LCC. Model studies of the proposed transition changes are recommended and could be carried out in the existing 1 to 10 scale wind tunnel used for the Task A studies of the original diffuser.

3. Based on the experimental measurements obtained with the K&R diffuser, a preliminary analysis of the cavitation susceptibility of the turning vanes in

the first elbow was made. The analysis utilized the turning vane profile of the 36 inch DTNSRDC water tunnel, as pressure distributions were available for that shape. Computations indicated that the vanes are susceptible to cavitation, and profiles with a less peaky pressure distribution are recommended. The eventual consideration of unsteady velocity effects will strengthen this recommendation. Changing the turning vane design should not affect the overall configuration of the LCC.

4. Because cavitation testing is the primary use of this facility, careful attention must be paid to control of the nuclei population. There are basically two methods of control. The first is to degas and filter the water to the extent that very few nuclei exist under natural conditions. Nuclei are then added to the flow under carefully controlled conditions. This can be done in localized regions via electrolysis or by seeding the entire flow either by injecting air saturated water or by direct injection of air. A second alternative is to accept the naturally occurring distribution of bubbles which can be adjusted by controlling the level of dissolved gas in the flow. In this method, the nuclei size distribution is determined as a function of the level of dissolved gas. Day to day adjustments of the nuclei population are accomplished by adjusting the level of dissolved gas (which is easily measured). In the former method, a compromise between the seeding method and the desired turbulence level in the tunnel test section must be made. This trade-off should be left to the individual experimenter. Estimates of the nuclei population and its relationship to the level of dissolved gas can be obtained in the 1 to 5 scale model experiments.

5. Several alternate test sections with free surface capability have been examined conceptually. A subcritical flow may be obtained by operating the baseline LCC design with a lowered water level. Two schemes with a

supercritical flow have been proposed; one with a hydraulic jump in the test section and the other with a skimmer. The concept utilizing a hydraulic jump was qualitatively evaluated in a small scale model, and its usefulness is judged to be marginal. The concept with a skimmer provides a more useful test section, but involves extensive design of a removable alternate section. The skimmer design and the modification of the downstream diffuser will require much effort. An additional pumping system is necesssary to return the skimmed flow back to the flow circuit.

Model studies are required to evaluate any concept for an alternate test section. As no deaeration devices are contemplated in the designs, the time available for a test run before air concentration becomes excessive may be quite short. Therefore, the utility of a high speed free surface alternate test section within the baseline LCC design configuration is questionable.

6. Estimates have been made of the loss coefficients for each component in the preliminary K&R design. The total headloss in the circuit is about the same as originally estimated by K&R. As interaction between the close coupled components could not be included, more definitive values will be obtained in the 1 to 5 scale model of the entire flow circuit.

REFERENCES

1. Wille, R. Beiträge zur Phänomenologie der Freistrahlen, Zeitschrift für Flugwissen-schaften, Band 11, 1963, pp. 222-233.

2. Stratford, B. S. The Prediction of Separation of the Turbulent Boundary Layer, Jour. Fluid Mech., Vol. 5, 1959, pp. 1-16.

3. Morel, T. Comprehensive Design of Axisymmetric Wind Tunnel Contractions, ASME Jour. Fluids Engrg., June, 1975, pp. 225-233.

4. Morel, T. Design of Two-Dimensional Wind Tunnel Contractions, ASME Jour. Fluids Engrg., June, 1977, pp. 371-378.

5. Ripken, J. F. Design Studies for a Closed-Jet Water Tunnel, St. Anthony Falls Hydraulic Laboratory, University of Minnesota, Tech. Paper No. 9, Series B, Aug., 1951.

6. Eisenberg, P. Mechanics of Cavitation, Handbook of Fluid Dynamics, ed. V. L. Streeter, New York, McGraw Hill, 1961, pp. 12.2 - 12.24.

7. Acosta, A. J. Cavitation and Fluid Mechinery, Cavitation, Conf. held at Heriot-Watt Univ., Edinburgh, Scotland, Sept., 1974, London, Inst. Mech. Engrs., 1974, pp. 383-396.

8. Acosta, A. J., Parkin, B. R. Cavitation Inception--A Selective Review, Jour. Ship Res., Vol. 19, 1975, pp. 193-205.

9. Knapp, R. T., Daily, J. W., Hammitt, F. G. Cavitation, New York, McGraw-Hill, 1970, 578 pp.

10. Karelin, V. Ya. Kavitatsionnye Yavleniya v Tsentrobezhnykh i Osevykh Nasosakh (Cavitation Phenomena in Centrifugal and Axial Pumps), Moscow, Mashgiz, Transl. available through Boston Spa (Engl.) Nat. Lending Lib. for Sci. & Engrg, 1963, 354 pp.

11. Pearsall, I. S. Cavitation, London: Mills & Boon, 1972.

12. Wu, T. Y. Cavity and Wake Flows, Annual Rev. Fluid Mech., Vol. 4, 1972, pp. 243-284.

13. Acosta, A. J. Hydrofoils and Hydrofoil Craft, Annual Rev. Fluid Mech., Vol. 5, 1973, pp. 161-184.

14. Plesset, M. S., Prosperetti, A. Bubble Dynamics and Cavitation, Annual Rev. of Fluid Mech., Vol. 9, 1977, pp. 145-185.

15. Rosenhow, W.M. Boiling, Annual Rev. Fluid Mech., Vol. 3, 1971, pp. 211-236.

16. van Wijngaarden, L. One-Dimensional Flow of Liquids Containing Small Gas Bubbles, Annual Rev. Fluid Mech., Vol. 4, 1972, pp. 369-396.

17. Holt, M. Underwater Explosions, Annual Rev. Fluid Mech., Vol. 9, 1977, pp. 187-121.

18a. Arndt, R.E.A. Cavitation in Fluid Machinery and Hydraulic Structures, Ann. Rev. Fluid Mech., Vol. 13, 1981, pp. 273-328.

18b. Arndt, R.E.A. Recent Advances in Cavitation Research, Advances in Hydroscience, Vol. 12, ed V. T. Chow, Academic Press, 1981.

19. Vennard, J. K., Harrold, J. C., Warnock, J., E., Hickox, G. H. Cavitation in Hydraulic Structures: A Symposium, Trans. ASCE, Vol. 112, 1947, pp. 2-72, discussion 73-124.

20. Cavitation in Hydrodynamics, Proc. Symp, Natl. Physical Lab, Sept. 1955, London:HMSO, 1956.

21. Brown, F. R. Cavitation in Hdyraulic Structures: Problems Created by Cavitation Phenomena, J. Hydraul. Div., ASCE, Vol. 89, HY1, 1963, pp. 99-115.

22. Numachi, F., Ed. Cavitation and Hydraulic Machinery, Proc. IAHR Symp., Inst. High Speed Mech., Tohoku Univ., Sendai, Japan, 1963, 570 pp.

23. Davies, R., ed. Cavitation in Real Liquids, Amsterdam, Elsevier, 1964.

24. Holl, J. W., Wood, G. M. (eds.) Symp. Cavitation Res. Facilities and Techniques, ASME, 1964.

25. Wood, G. M., Hartz, F. H., Hammitt, F. G., Agostinelli, A. eds. Symp. Cavitation in Fluid Machinery, ASME, 1965, 267 pp.

26. Robertson, J. M., Wislicenus, G. F., eds. Cavitation State of Knowledge, ASME, New York, 1969.

27. Institute of Mechanical Engineers. Cavitation, Conf. held at Heriot-Watt Univ., Edinburgh, Scotland, Sept. 1974, London, Inst. Mech. Engrs., 1974.

28. IAHR, Proc. IAHR Symp. Two Phase Flow and Cavitation in Power Generation Systems, Grenoble, France, 1976.

29. Plesset, M. S., Physical Effects in Cavitation and Boiling, Proc. 1st Symp. Naval Hydrodyn., Washington, D. C., 1956, pp. 297-323.

30. Kermeen, R. W. Water Tunnel Tests of NACA 4412 and Walchner Profile 7 Hydrofoils in Noncavitating and Cavitating Flows, Calif. Inst. Tech. Hydrodyn. Lab., Rep. 47-5, 1956.

31. Kermeen, R. W. Water Tunnel Tests of NACA 66, - 012 Hydrofoil in Noncavitating and Cavitating Flows, Calif. Inst. Tech. Hydrodyn. Lab., Rep. 47-7, 1956, 12 pp.

32. Daily, J. W. Cavitation Characteristics and Infinite-Aspect Ratio Characteristics of a Hydrofoil Section, Trans. ASME, Vol. 71, 1949, pp. 269-284.

33. Brockett, T. Minimum Pressure Envelopes for Modified NACA-66 Sections with NACA a = 0.8 Camber on Bu Ships Type I and Type II Sections, David Taylor Model Basin Rep. 1780, 1966, 39 pp.

34. Young, J. O., Holl, J. W. Effects of Cavitation on Periodic Wakes Behind Symmetric Wedges, J. Basic Engrg., Vol. 88, 1966, pp. 163-176.

35. Knapp, R. T. Recent Investigations of the Mechanics of Cavitation and CAvitation Damage, Trans. ASME, Vol. 77, 1955, pp. 1045-1054.

36. Stinebring, D. R. Scaling of Cavitation Damage, M.S. Thesis, Penn. State Univ., University Park, Pa., 1976.

37. Shen, Y. T., Peterson, F. B. Unsteady Cavitation on an Oscillating Hydrofoil, 12th Symp. Naval Hydrodyn., Washington, D. C., 1978, pp. 362-384.

38. Kermeen, R. W., McGraw, J. T., Parkin, B. R. Mechanism of Cavitation Inception and the Related Scale-Effects Problem, Trans. ASME, Vol. 78, 1956, pp. 533-541.

39. Holl, J. W., Wislicenus, G. F. Scale Effects on Cavitation, J. Basic Engr., Vol. 83, 1961, pp. 385-398.

40. Arndt, R. E. A. Cavitation Inception and How it Scales: A Review of the Problem with a Summary of Recent Research, Proc. Symp. High Powered Propulsion of Large Ships, Wageningen, The Netherlands, Part 2, pp. XXI, 1-65, 1974, (available from Netherlands Ship Model Basin).

41. Arndt, R. E. A. Pressure Fields and Cavitation, Trans. 7th IAHR Symp., Vienna, Part 1, 1974, pp. IX, 1-20.

42. Holl, J. W., Robertson, J.M. Discussion of Kermeen et al. (1956). Trans. ASME, Vol. 78, 1956, p. 540.

43. Holl, J. W. An Effect of Air Content on the Occurrence of Cavitation, J. Basic Engr., Vol. 82, 1960, pp. 941-946.

44. Acosta, A. J. Hamaguchi, H. Cavitation Inception on the ITTC Standard Head Form, Calif. Inst. Technol. Hydrodyn. Lab Rep. No. E-149, 1967.

45. Holl, J. W., Treaster, A. L. Cavitation Hysteresis, J. Basic Engrg., Vol. 88, 1966, pp. 199-212.

46. Gupta, S.K. The Influence of Porosity and Contact Angle on Incipient and Desinent Cavitation, M.S. Thesis, Penn. State Univ., University Park, Pa., 1969.

47. Peterson, F. B. Cavitation Originating at Liquid-Solid Interfaces, Naval Ship Res. and Develop. Cent. Rep 2799, 1968.

48. van der Meulen, J. H. J. Cavitation on Hemispherical Nosed Teflon Bodies, Int. Shipbuilding Prog., Vol. 19, 1972, pp. 333-341.

49. Holl, J. W., Limited Cavitation, Cavitation State of Knowledge, 1969, pp. 26-63.

50. Holl, J. W., Nuclei and Cavitation, J. Basic Engrg., Vol. 92, 1970, pp. 681-688.

51. Epstein, P. S., Plesset, M. S. On the Stability of Gas Bubbles in Liquid-Gas Solutions, J. Chem. Phys., Vol. 18, 1950, pp. 1505-1509.

52. Harvey, E. N., Barnes, D. K., McElroy, W. D. Whiteley, A. H., Pease, D. C., Cooper, K. W. Bubble Formation in Animals, I. Physical Factors, J. Cell. Comp. Physiol., Vol. 24, 1944, pp. 1-22.

53. Harvey, E. N. Whiteley, A. H., McElroy, W. D., Pease, D. C., Barnes, D. K. Bubble Formation in Animals, II. Gas Nuclei and Their Distribution in Blood and Tissues, J. Cell. Comp. Physiol., Vol. 24, 1944, pp. 23-34.

54. Harvey, E. N., McElroy, W. D., Whiteley, A. H. On Cavity Formation in Water, J. Appl. Phys., Vol. 18, 1947, pp. 162-172.

55. Ripken, J. R., Killen, J. M. Gas Bubbles: Their Occurrence, Measurement, and Influence in Cavitation Testing, Proc. IAHR Symp., Sendai, Japan, 1962, pp. 37-57.

56. Arndt, R. E. A., Keller, A. P. Free Gas Content Effects on Cavitation Inception and Noise in a Free Shear Flow, Proc. IAHR Symp. Two Phase Flow and Cavitation in Power Generation Systems, Grenoble, France, 1976, pp. 3-16.

57. Gates, E. M., Acosta, A. J. Some Effects of Several Free-Stream Factors on Cavitation Inception on Axisymmetric Bodies, 12th Symp. Naval Hydrodyn., Washington, D. C., 1978, pp. 86-108.

58. Keller, A. P., Weitendorf, E. A. Influence of Undissolved Air Content on Cavitation Phenomena at the Propeller Blades and on Induced Hull Pressure Amplitudes, Proc. IAHR Symp. Two Phase Flow and Cavitation in Power Generation Systems, Grenoble, France, 1976, pp. 65-76.

59. Barral, L. A Critical Examination of the Influence of Dissolved Gas on the Cavitation Process in Turbulent Shear Flows, M. S. Thesis in Fluids Mechanics, University of Minnesota, 1983.

60. Ooi, K. K. Scale Effects on Cavitation Inception in Submerged Jets, Ph. D. Thesis, David Taylor Naval Ship Research and Development Center Report No. Eng. 183-6, 1981.

61. Oba, R., Kim, K. T., and Uranishi, K. Singular Behavior of Cavitationin Undersaturated Water, Report No. 357, Institute of High Speed Mechanics, Tohoku University, Japan, Vol. 46, 1983.

62. Blake, F. G., Jr. The Onset of Cavitation in Liquids, I, Harvard Acoustics Res. Lab TM 12, Sept. 1949.

63. Johnson, V. E., Hsieh, T. The Influence of the Trajectories of Gas Nuclei on Cavitation Inception, 6th Symp. Naval Hydrodyn., Washington, D. C., 1966, pp. 163-182.

64. Keller, A. P. The Influence of the Cavitation Nucleus Spectrum on Cavitation Inception, Investigated with a Scattered Light Counting Method, J. Basic Eng., Vol. 94, 1972, pp. 917-925.

65. Keller A. P. Investigations Concerning Scale Effects of the Inception of Cavitation, Cavitation, pp. 109-117. Conf. held at Heriot-Watt Univ., Edinburgh, Scotland, Sept. 1974, London: Inst. Mech. Engrs.

66. Arndt, R. E. A., George, W. K. Pressure Fields and Cavitation in Turbulent Shear Flows, 12th Symp. Naval Hydrodyn., Washington, D. C., 1978, pp. 327-339.

67. Kuiper, G. Scale Effects on Propeller Cavitation Inception, 12th Symp. Naval Hydrodyn., Washington, D. C., 1978, pp. 400-429.

68. Ripken, J. R., Killen, J. M. A Study of the Influence of Gas Nuclei on Scale Effects and Acoustic Noise for Incipient Cavitation in a Water Tunnel, St. Anthony Falls Hydraulic Lab. Tech. Pap. 27-B, 1959, 49 pp.

69. Peterson, F. B., Danel, F., Keller, A., Lecoffe, Y. Determination of Bubble and Particulate Spectra and Number Density in a Water Tunnel with Three Optical Techniques, Proc. 14th Int. Towing Tank Conf., Ottawa, Vol. 2, 1975, pp. 27-52.

70. Peterson, F. B. Hydrodynamic Cavitation and Some Considerations of the Influence of Free Gas Content, 9th Symp. Naval Hydrodyn., Paris, Vol. 2, 1972, pp. 1131-1186.

71. Feldberg, L. A., Shlemenson, K. T. The Holographic Study of Cavitation Nuclei, Proc. IUTAM Symp. Non-Steady Flow of Water at High Speeds, Leningrad, USSR, 1971, pp. 239-242 (English version, Moscow 1973, pp. 106-111).

72. Morgan W. B., Air Content and Nuclei Measurement, Proc. 13th Int. Towing Tank Conf., Berlin/Hamburg, Vol. 1, 1972, pp. 657-674.

73. Edstrand, H. Cavitation Tests with Model Propellers in Natural Sea Water with Regard to the Gas Content of the Water and Its Effect Upon Cavitation Point and Propeller Characteristics, SSPPA Rep. No. 5, Goteborg, Sweden, 1950.

74. Arndt, R. E. A. The Influence of Dissolved and Free Gas Content on Cavitation, Boeing Co. Doc. No. D 324-51505-1, 1979.

75. Wade, R. B., Acosta, A. J. Experimental Observations on the Flow Past a Plano-Convex Hydrofoil, J. Basic Engrg., Vol. 88, 1966, pp. 273-283.

76. Baker, C. B., Holl, J. W., Arndt, R. E. A. The Influence of Gas Content and Polyethelene Oxide Additive Upon Confined Jet Cavitation in Water, ASME Cavitation and Polyphase Flow Forum, 1976, pp. 6-8.

77. Rouse, H. Cavitation in the Mixing Zone of a Submerged Jet, Houille Blanche, Vol. 8, 1953, pp. 9-19.

78. Brownell, W. F. A 36-Inch Variable Pressure Water Tunnel, DTMB Report 1052, 1956.

79. Albrecht, K., Bjorheden, O. Cavitation Testing of Propellers in a Free Surface Tunnel Utilizing Micro Air Bubble Control, Jour. Fluids Engineering, 1975, pp. 523.

80. Etter, R. J. and Altmann, R. A Study of the Preliminary Design and Operation of a Large Cavitation Tunnel (NAVSEA Report 3213-82-08), Hydronautics, Inc. Tech. Report 7925.58-1, May, 1982.

81. Etter, R. J. Addendum to a Study of the Preliminary Design and Operation of a Large Cavitation Tunnel (NAVSEA Report 3213-82-08), Hydronautics, Inc. Tech. Report 82010.23-1, Jan., 1983.

82. Schiebe, F. R. The Stochastic Characteristics of Pressure Fluctuations on a Channel Bed Due to the Macroturbulence in a Hydraulic Jump, Ph.D. Thesis, Dec. 1971.

83. Ripken, J. F., Wetzel, J. M. and Bergstedt, L. M. Hydrodynamic Studies for a Large, High-Speed, Variable Pressure, Free Surface Flow Facility, St. Anthony Falls Hydraulic Laboratory, University of Minnesota M-134, Aug., 1973.

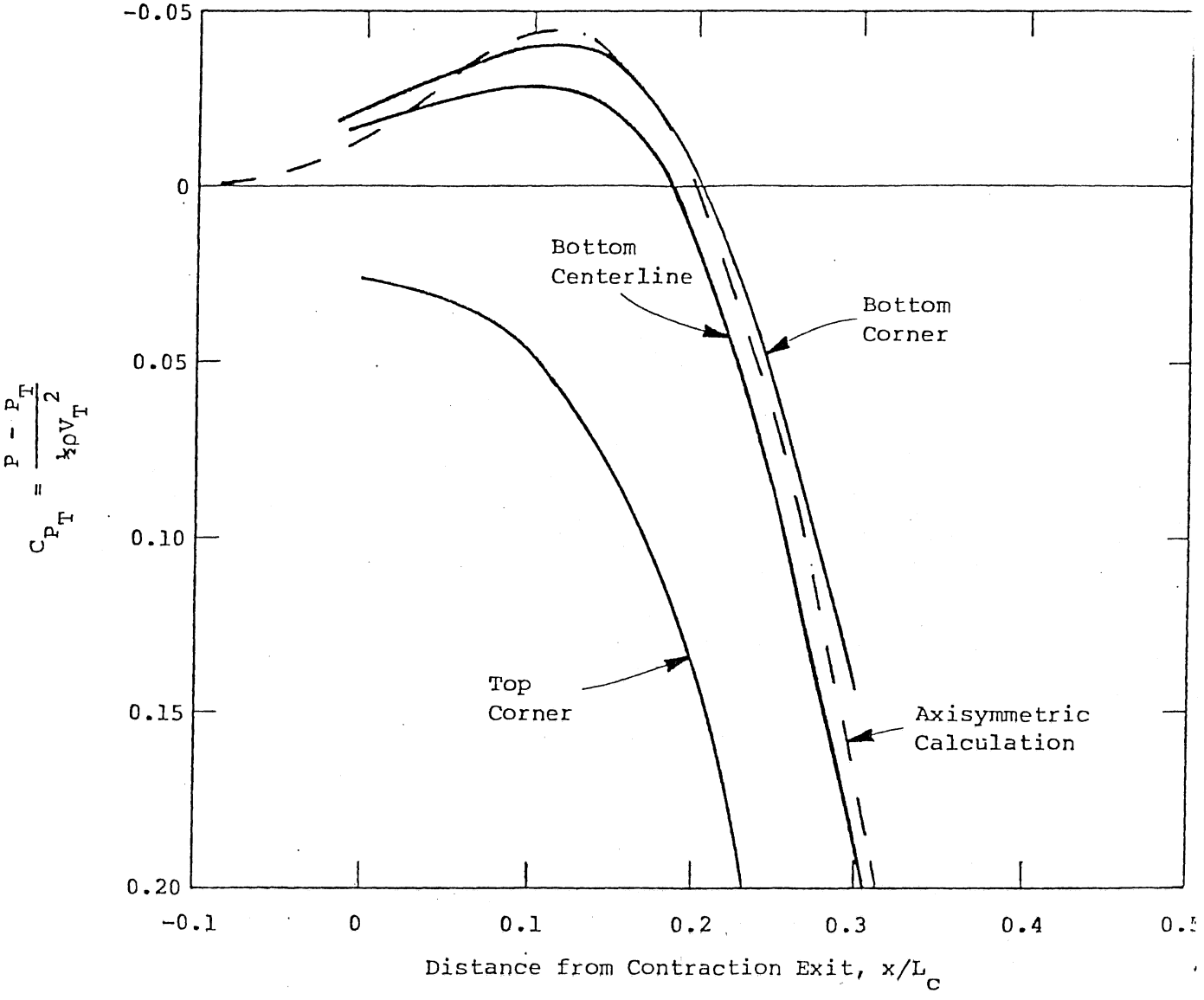

Fig. 1 - Pressure Coefficient at Contraction Exit.

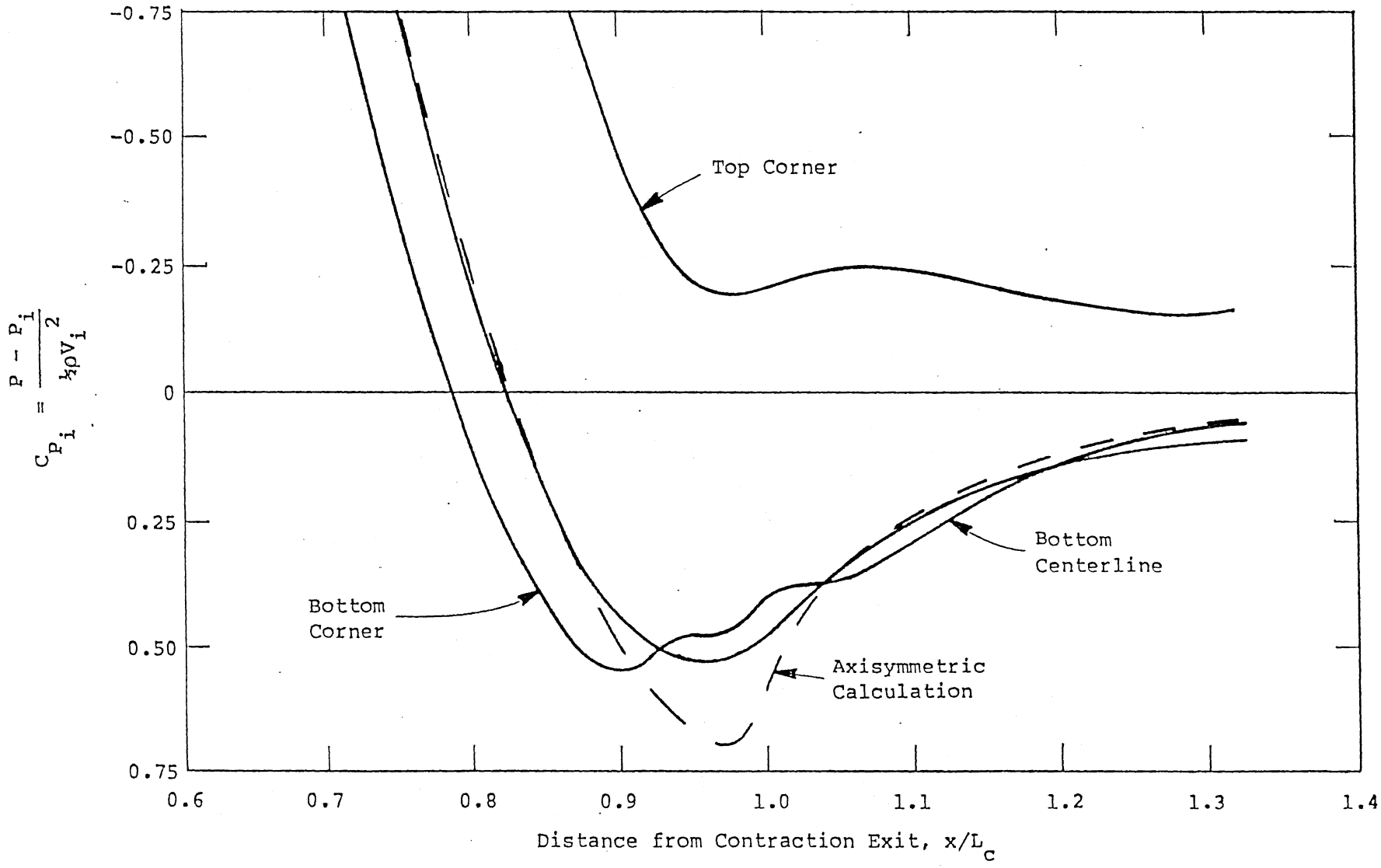

Fig. 2 - Pressure Coefficient at Contraction Inlet.

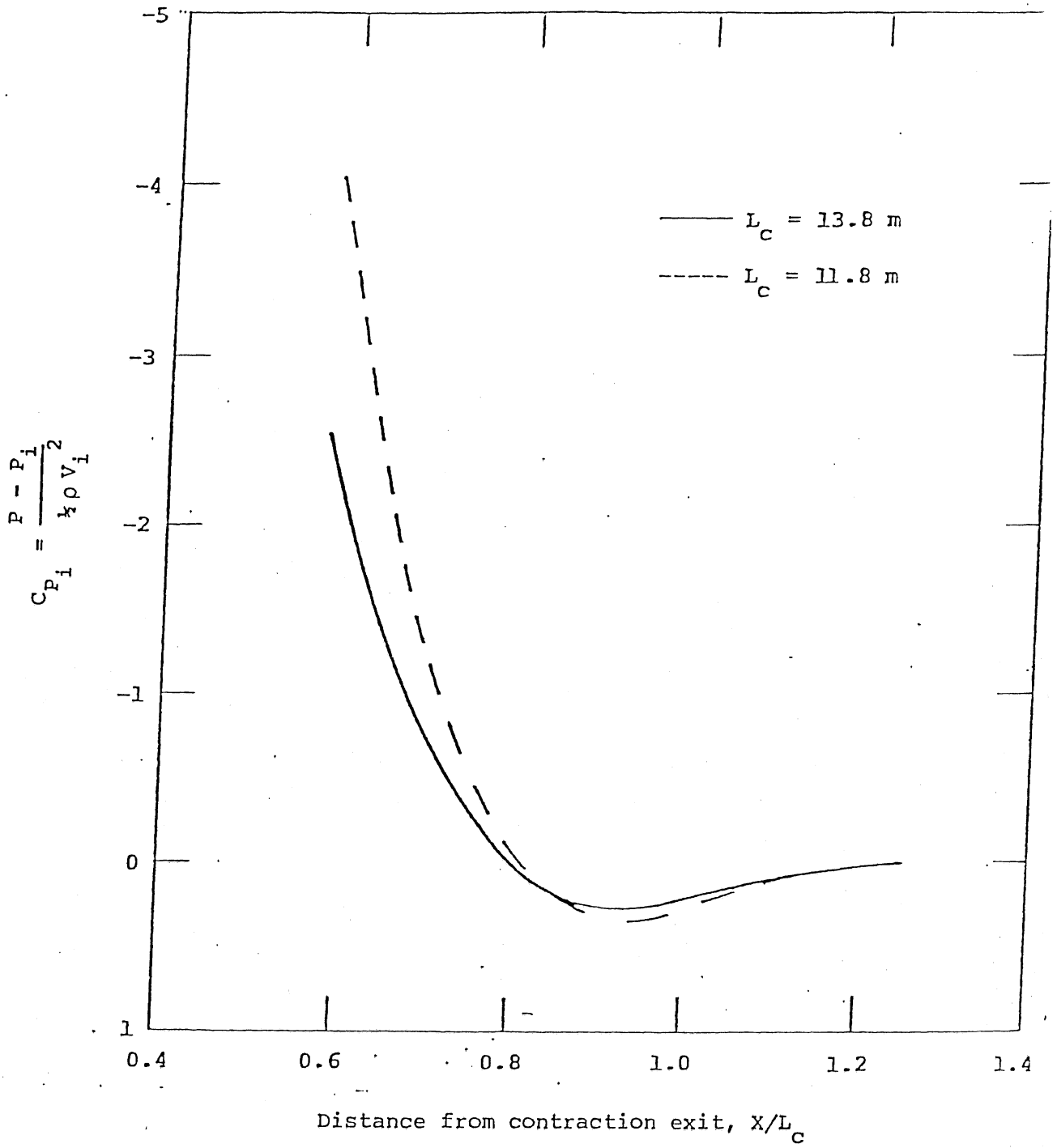

Fig. 3. Comparison of pressure coefficients based on inlet conditic C_{P_i} along the center line on the bottom surface.

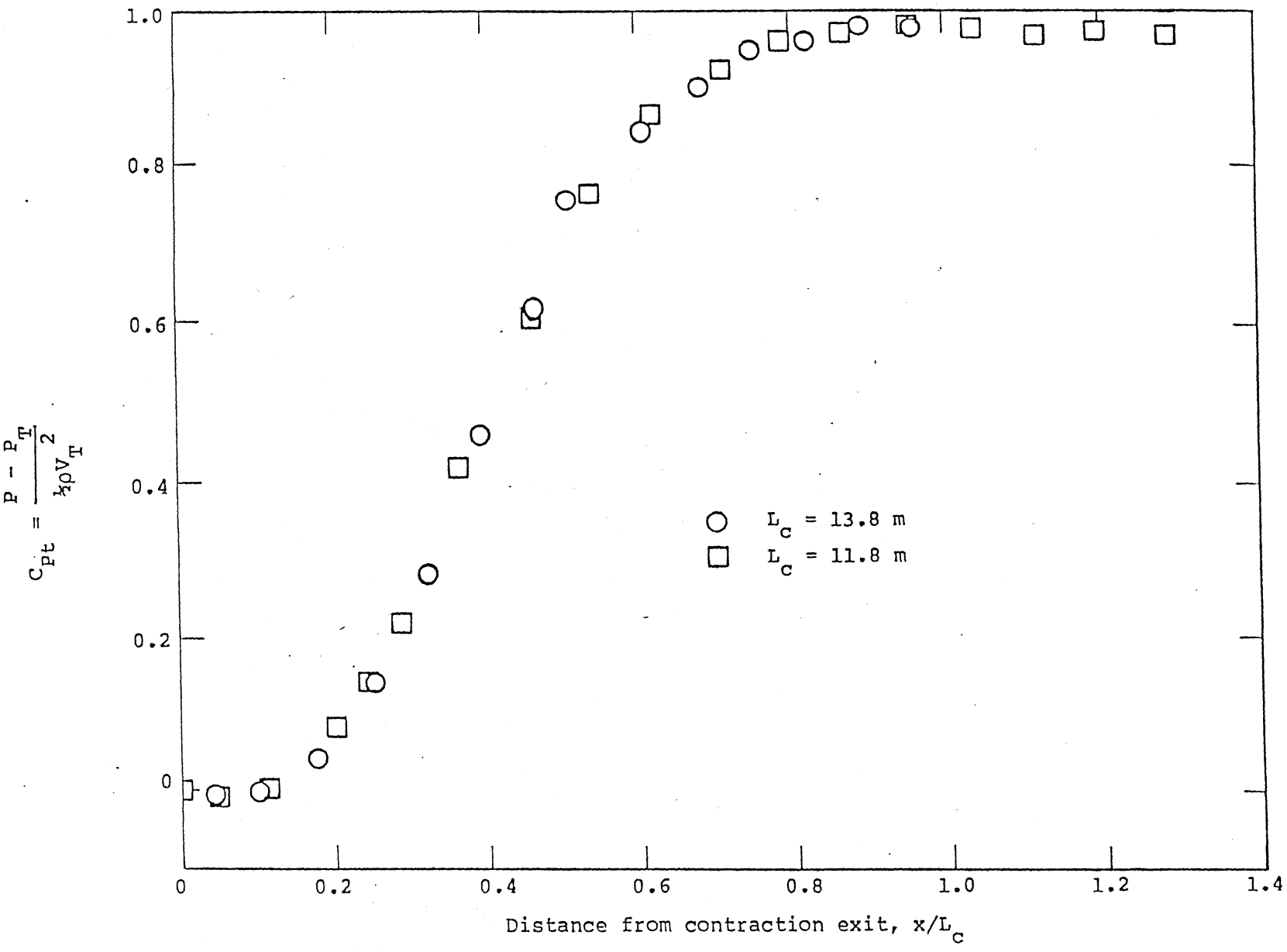

Fig. 4. Comparison of pressure coefficients based on test section condition, C_{Pt}, along the center line on the bottom surface.

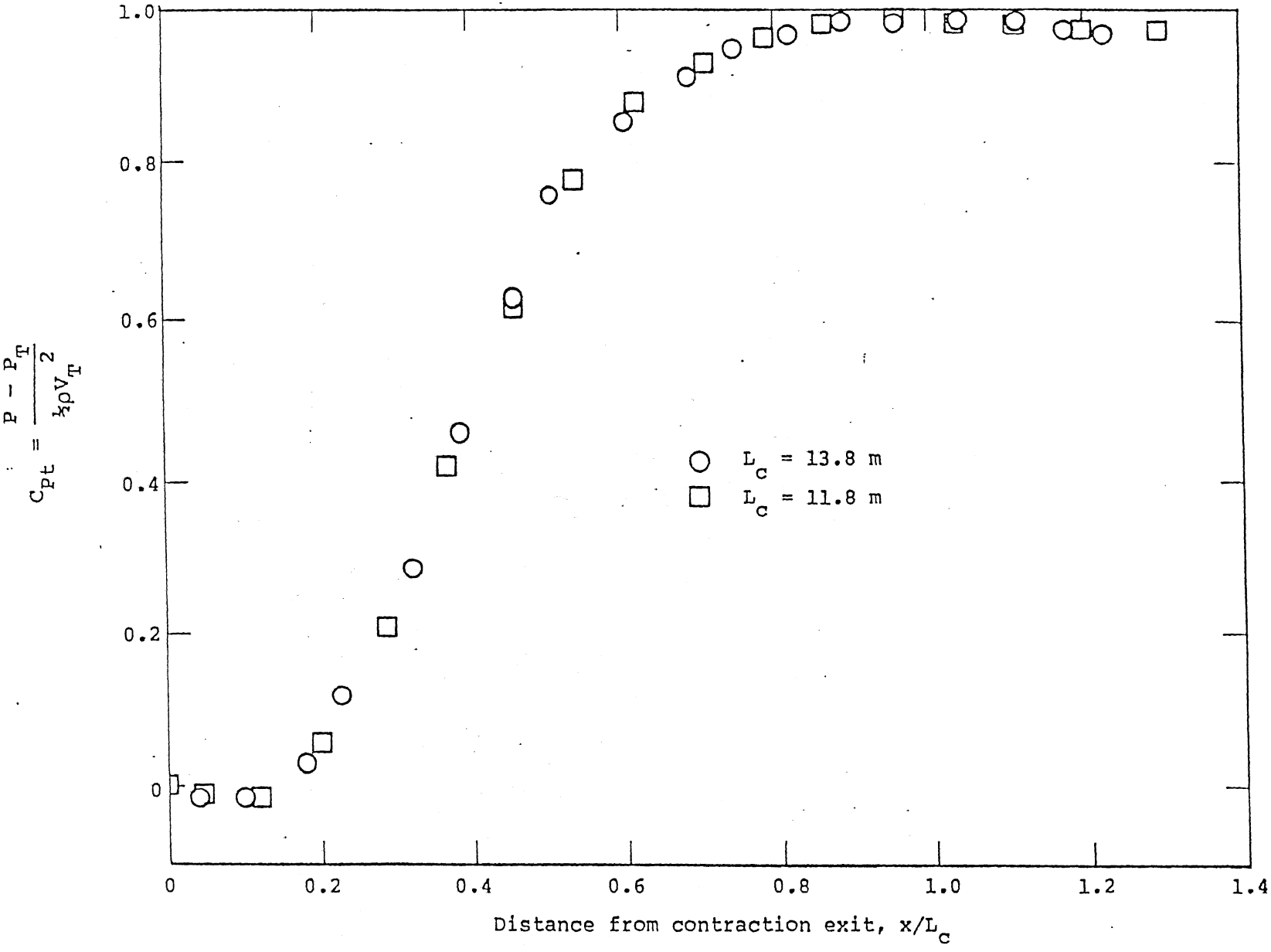

Fig. 5. Comparison of pressure coefficient based on test section condition, C_{Pt}, along the bottom corner.

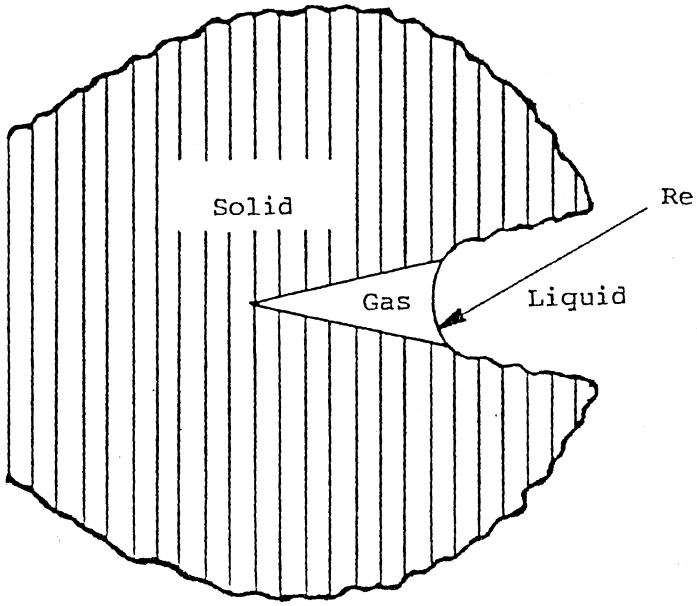

Fig. 6 – Schematic of a Cavitation Nucleus in the Form of a Solid Particle (Harney et al 1947).

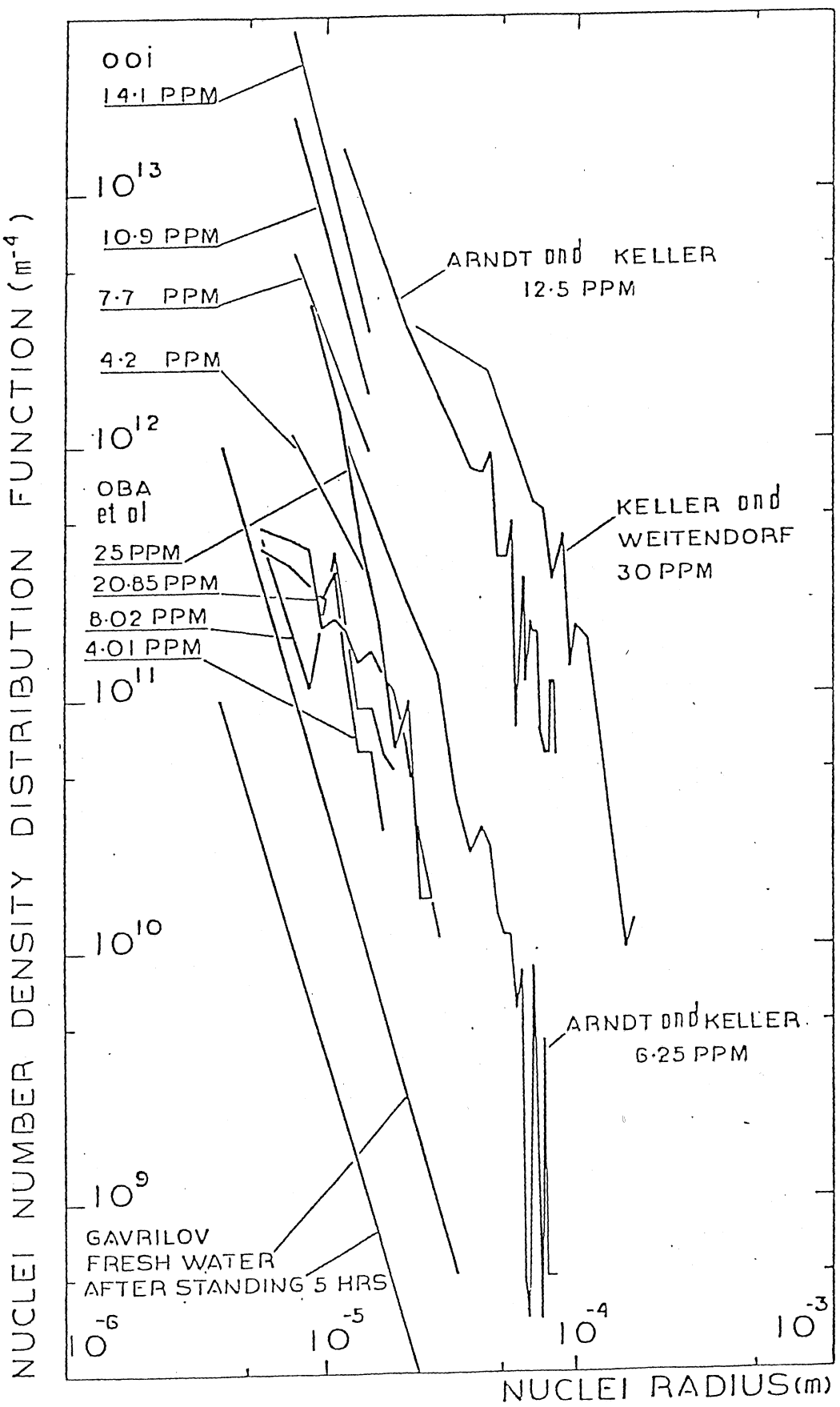

Fig. 7 – Nuclei Number Spectra for Various Total Air Contents

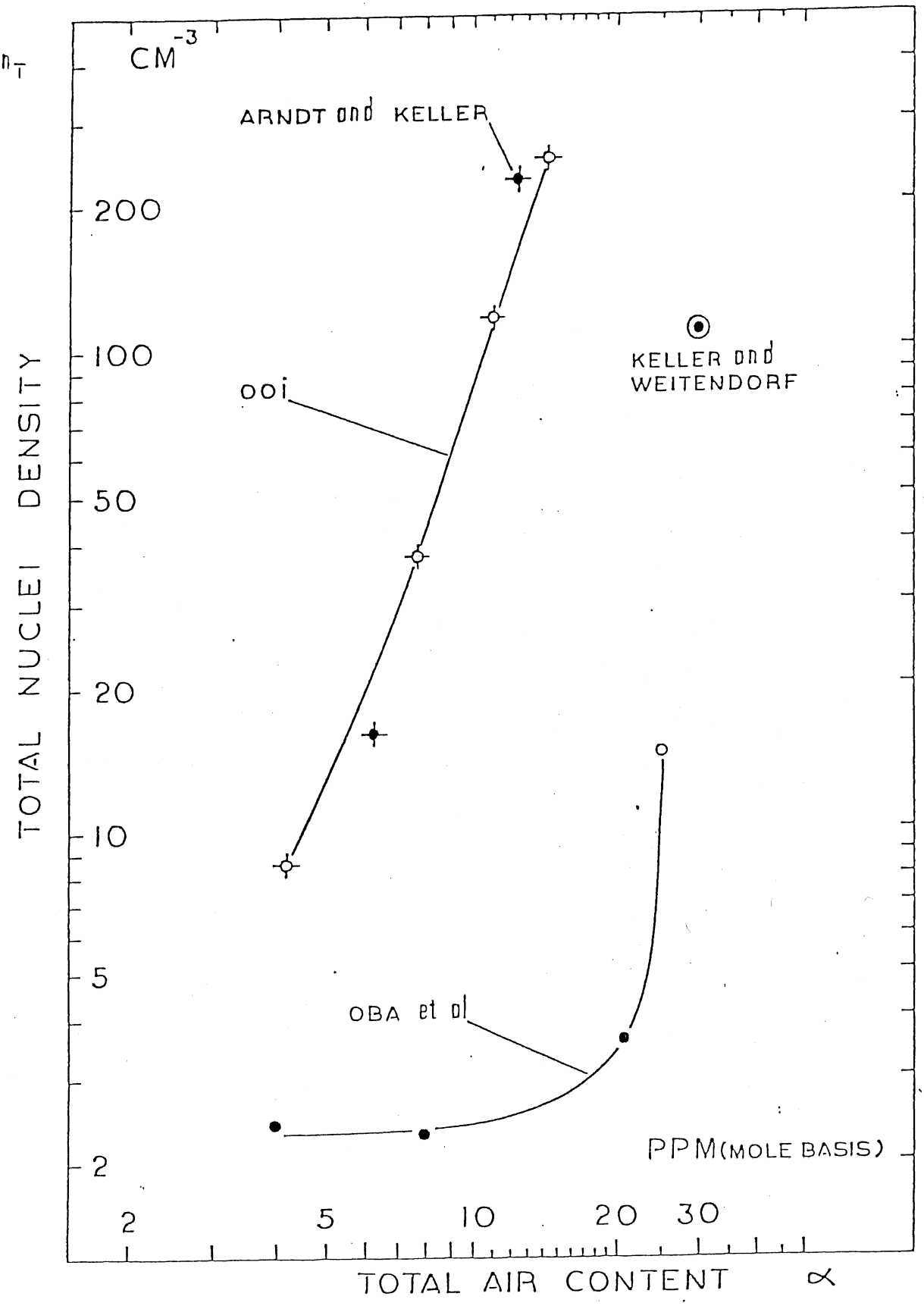

Fig. 8 - Influence of the Total Air Content, α, on the Total Nuclei Density, N_T, for Various Facilities.

$$K_H = \frac{H}{n^2 D^2} \qquad K_Q = \frac{Q}{ND^3}$$

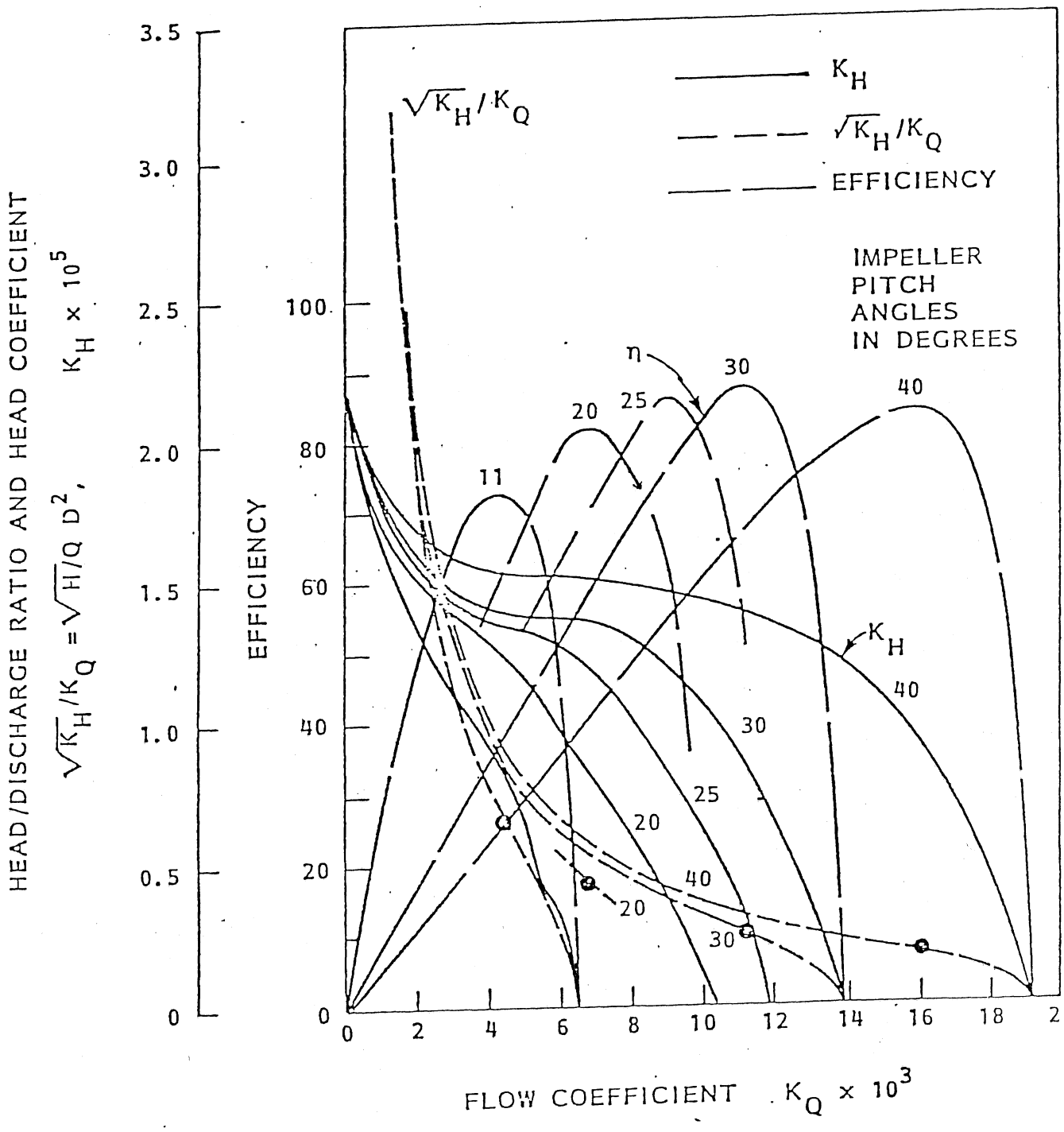

Fig. 9 – Estimated Performance of Variable-Pitch Pump for Large Cavitation Tunnel (from Etter [80]).

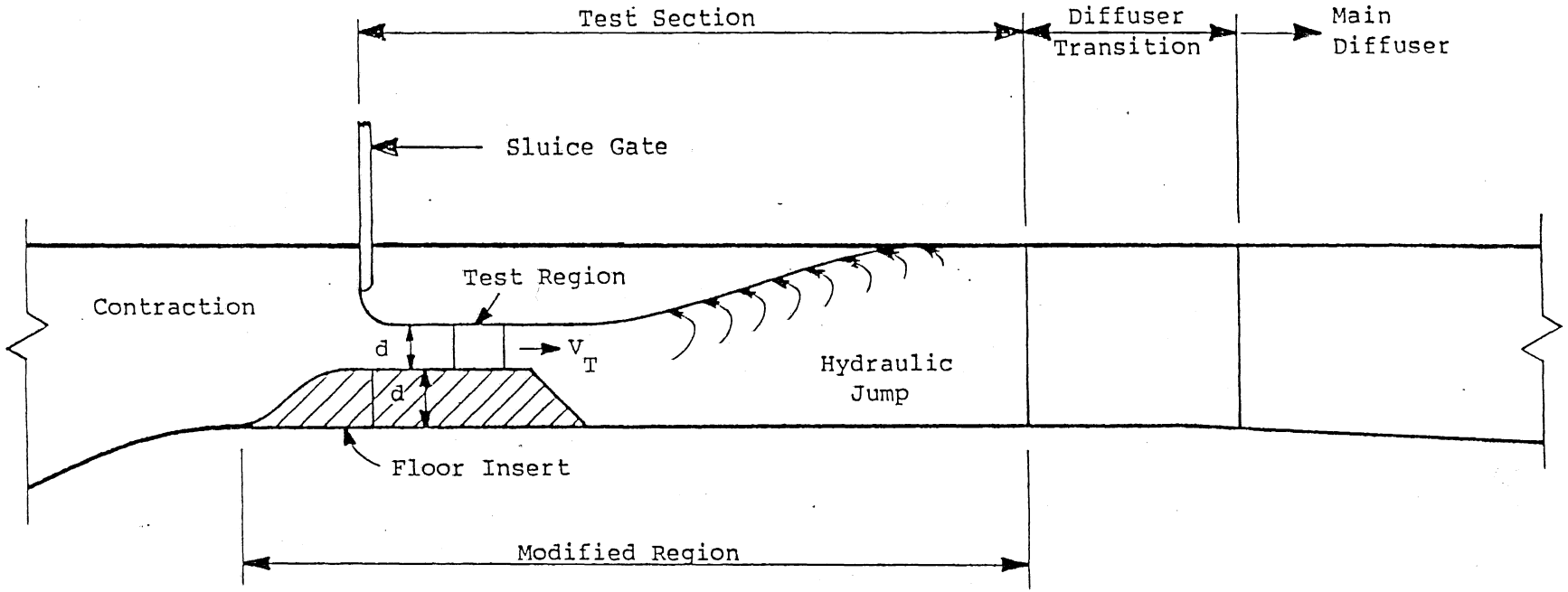

Fig. 10 - Supercritical Free Surface Test Section with Hydraulic Jump (after Etter [81]).

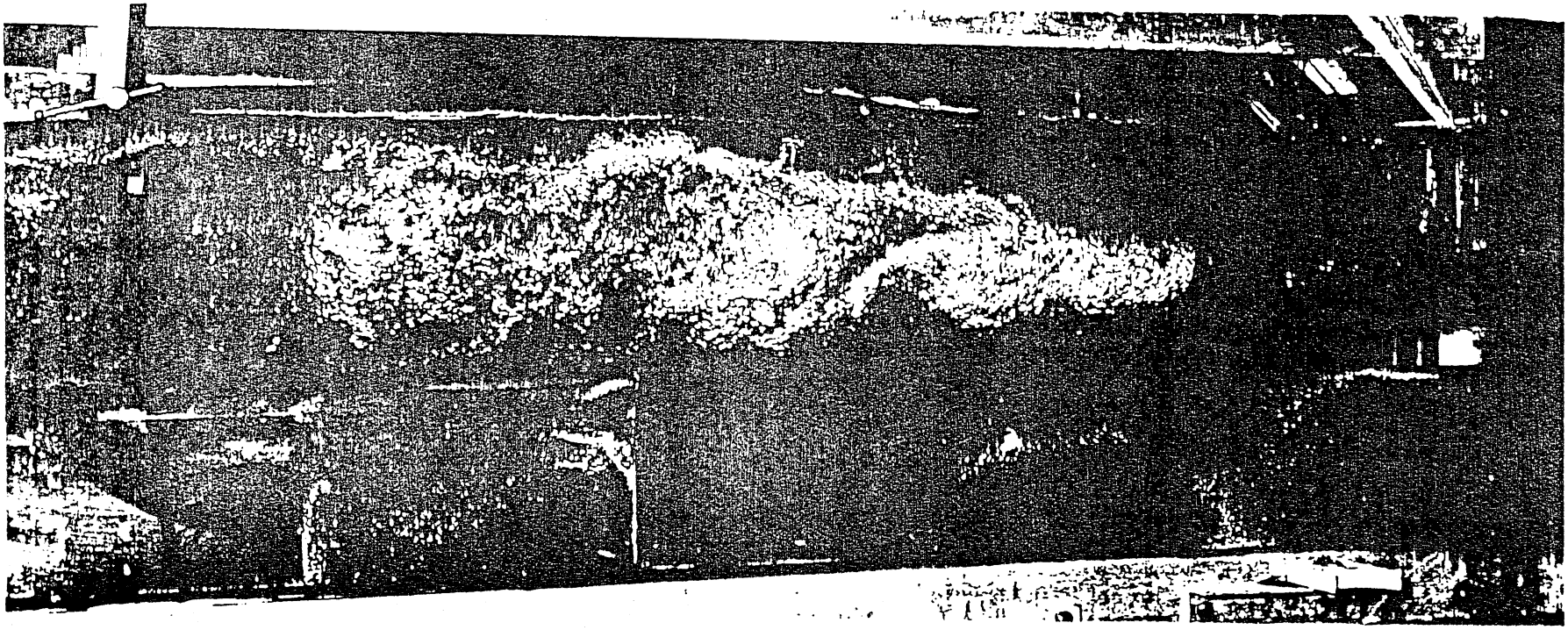

Fig. 11. Photo of 1 to 20 scale model of supercritical free surface test section with hydraulic jump.

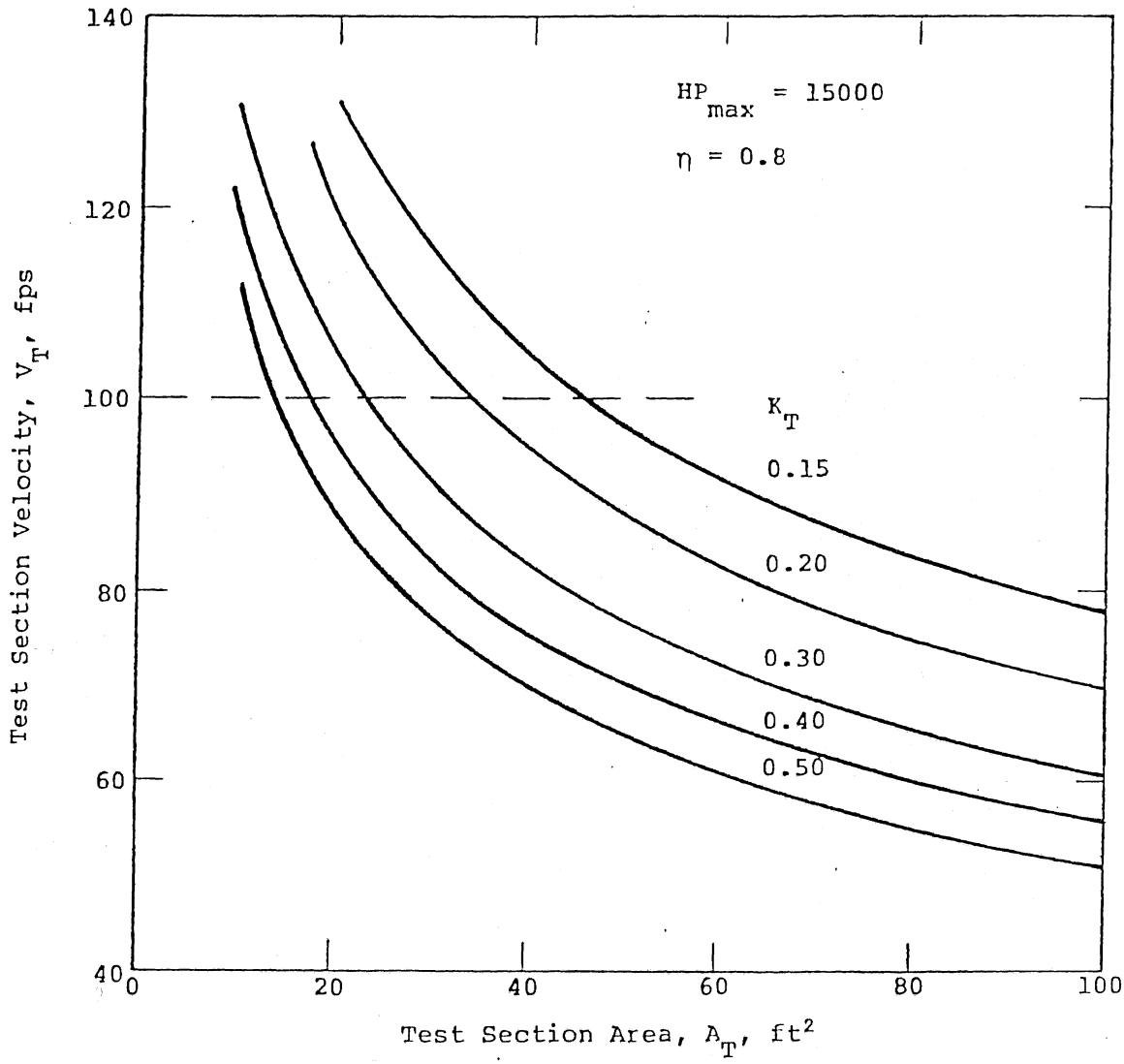

Fig. 12 - Test Section Parameters at Maximum Available Horsepower and Various Tunnel Loss Coefficients.

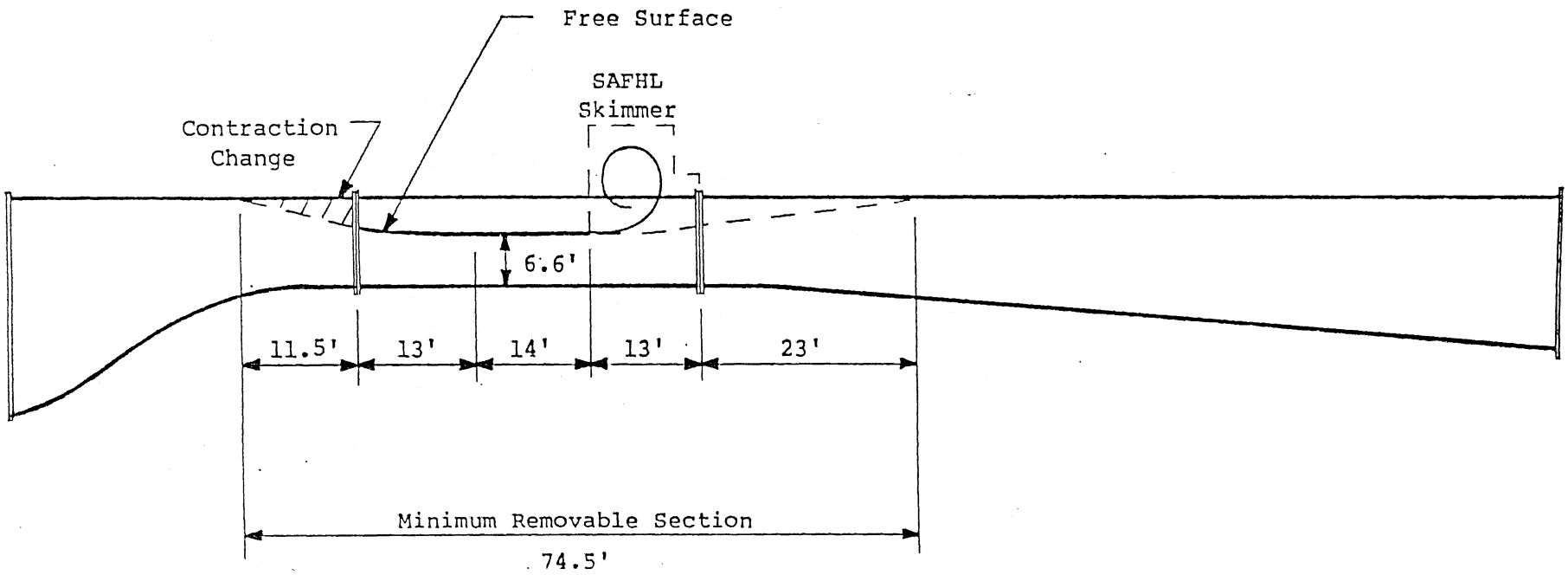

Fig. 13 - Alternate High Speed Free Surface Test Section Applied to Preliminary K & R Design.